MEMBRANE DISTILLATION CRYSTALLIZATION - PERFORMANCE ENHANCEMENT AND SCALING CONTROL

CHEN GUIZI 2014

NANYANG TECHNOLOGICAL UNIVERSITY

MEMBRANE DISTILLATION CRYSTALLIZATION - PERFORMANCE ENHANCEMENT AND SCALING CONTROL

CHEN GUIZI

SCHOOL OF CIVIL AND ENVIRONMENTAL ENGINEERING

NANYANG TECHNOLOGICAL UNIVERSITY

2014

MEMBRANE DISTILLATION CRYSTALLIZATION - PERFORMANCE ENHANCEMENT AND SCALING CONTROL

CHEN GUIZI

CHEN GUIZI

School of Civil and Environmental Engineering

A thesis submitted to the Nanyang Technological University
in fulfillment of the requirements for the degree of Doctor of Philosophy

2014

ACKNOWLEDGEMENTS

First of all, I would like to express my sincere appreciation and deep gratitude to my supervisors, Associate Professor ***Wang Rong*** and Professor ***Anthony G. Fane***. Their supports, scientific guidance and valuable advice throughout the project helped me to overcome difficulties and reach a new high in my career. It is lucky for me to work with both of them—their exceptional intelligence and academic integrity have given me substantial influence, for now and forever.

My special thanks go to Professor ***W.B. Krantz,*** for his brilliant advice on research and technical writing skills. During discussing with Prof. Krantz, I gained not only the sparkling inspirations and knowledge, but also confidence and optimistic nature that has an enormous influence on me.

I am grateful to Environment and Water Industry Program Office (EWI) for providing the scholarship and funding, to Singapore Membrane Technology Centre (SMTC) for providing a workplace equipped with necessary facilities and Siemens Water Technology (SWT) for membrane supply. Special thanks are due to Dr. Lu Yinghong and Deric Lim (Final Year Project students) for their helps and support in the experimental part; and Dr. Yang Xing for her kind guidance and help on technical writing skill, without which I would not be able to accomplish PhD work and this thesis smoothly.

Many thanks go to my friends and staff from SMTC, Chun Heng, Zhang Yuan, Lauren, Chen Lin, Wei Jing, Saren, Amir, Shuwen, Jingsong, Shuren, Ziggy and my former colleague Yuhui, Guangzhi, Elizabeth, Guoqiang etc. for their sharing of knowledge and kind assistance on various issues. Without their friendship and help, I would not have such an enjoyable postgraduate student life.

Lastly, I would like to thank my dearest parents and my husband for offering me unlimited moral support, perseverance and encouragement, being with me whenever frustrations/difficulties were met. Also, special thanks to my unborn baby, maybe mum can't offer you the best physical environment and has to take you to work every day, but mum hope you can acquire strong mind, optimism and painstaking. Mum and Dad love you forever.

PUBLICATIONS

In Journals

- **Guizi Chen**, Xing Yang, Rong Wang, Anthony G. Fane, Performance enhancement and scaling control with gas bubbling in direct contact membrane distillation, Desalination, 308 (2013): 47-55.

- **Guizi Chen**, Yinghong Lu, William B. Krantz, Rong Wang, Anthony G. Fane, Optimization of operating conditions for a continuous membrane distillation crystallization process with zero salty water discharge, Journal of Membrane of Science, 450 (2014): 1-11.

- **Guizi Chen**, Yinghong Lu, Xing Yang, Rong Wang, Anthony G. Fane, Quantitative study on the crystallization induced scaling in high concentration direct contact membrane distillation (DCMD), Industrial & Engineering Chemistry Research 53 (2014): 15656–15666.

- **Guizi Chen**, Xing Yang, Yinghong Lu, Rong Wang, Anthony G. Fane, Heat transfer intensification and scaling mitigation in bubbling-enhanced membrane distillation for brine concentration, Journal of Membrane Science, 470 (2014):60-69.

At International Conferences

- **Guizi Chen**, Yinghong Lu, Xing Yang, Rong Wang, Anthony G. Fane, Quantitative study on crystallization induced scaling in high concentration direct contact membrane distillation (DCMD) (oral presentation). The 10th International Congress on Membranes and Membrane Processes (ICOM), July 20-25, 2014, Suzhou, China.

TABLE OF CONTENTS

ABSTRACT

Membrane distillation (MD) is well recognized as a potential alternative technology for desalination due to the benefits of moderate operating temperatures, low sensitivity to feed salinity, high salt rejection and ability to incorporate free low-grade heat. However, technical challenges that impede the industrialization of MD brine processing still remain, which include the temperature polarization effect and fouling/scaling formation, especially at high salt concentration, etc.

This thesis provides a comprehensive review on the state-of-art of MD operations in concentrated solutions, focusing on some areas that need to be further investigated or improved, such as available methods for performance enhancement and scaling control in membrane processes, investigation and measurement of membrane fouling/scaling, the coupled processes of membrane and crystallization operations, which may provide strategies to address the above challenges.

Firstly, the potential of introducing gas bubbling has been preliminary explored to improve fluid dynamics and shear stress in the shell side of the DCMD module. The effect of operating conditions and module configuration on the flux enhancement ratio induced by gas bubbling were investigated in a low concentration (3.5%) DCMD. Additionally, the module performance and scaling status for high salt concentrations (from 18% to supersaturation) have been examined and compared in three systems (*i.e.*, modified module with knitted-spacers, original modules with and without bubbling). It was found that the introduction of gas bubbling not only mitigates the temperature polarization effect but also enhances surface shear stress intensity to postpone scaling formation on the membrane surface.

Secondly, a more in-depth theoretical analysis on the working mechanisms of gas bubbling was studied, with the aid of direct observation and statistical analysis on the bubble characteristics. The results showed that bubbles with small mean size and narrow size distribution were preferred for creating even flow distribution, intensifying mixing and enhancing surface shear stress. Compared to that of a non-

bubbling DCMD system, the values of heat transfer coefficient and temperature polarization coefficient (*TPC*) reached up to 2.30- and 2.13-fold, respectively, at an optimal gas flowrate. Additionally, with the theoretical expressions for scaling resistance derived based on resistance-in-series model, it was found that gas bubbling can remarkably decrease scaling resistance, due to the high shear stress induced by the flowing water and gas bubbles.

Thirdly, fundamentally, in order to prevent scaling formation and prolong membrane lifespan, a novel method was proposed to quantify the scaling formation in DCMD brine concentration processes, based on crystal kinetics on the membrane surface and transfer mechanisms of MD. A mathematical model, namely, crystallization on membrane surface (COMS), was developed and verified in terms of MD performance (critical point of major flux decline and scaling formation) and deposited crystal characteristics (median size and total number). The results indicated that the critical point can be estimated precisely based on COMS model and the scaling information can be quantified effectively by crystallization kinetics. A good agreement with an acceptable average absolute relative error of 10% between the experimental and simulated data confirms the reliability of this proposed COMS model.

Fourthly, a hybrid process that integrates MD with crystallization, namely continuous membrane distillation crystallization (CMDC), was systematically studied with a highly concentrated NaCl feed solution (26.7 wt% salt). In order to improve the product recovery (pure water and NaCl crystal) and better realize zero discharge, an orthogonal fractional factorial (OFF) experiment design was used to optimize the operating conditions. The range analysis of the experimental results identified the feed and permeate-side flow rates as the most influential factors affecting CMDC performance. Additionally, the optimal operating parameters determined from the analysis were validated experimentally, which confirmed the merits of the OFF experiment design and analysis for the CMDC process.

Keywords: high concentration membrane distillation; crystallization; gas bubbling; performance enhancement; scaling control; hybrid membrane process; desalination**.**

LIST OF SYMBOLS

A	effective membrane area, m^2
AARE	average absolute relative error
a	gas sparging area, m^2
B	crystal nucleation rate, the combination of crystal birth by nucleation and crystal death by dissolution, No. s^{-1} m^{-3}
B'	overall crystal birth rate associated with nucleation growth by supersaturation and simultaneous crystal death by dissolution in the same size range of l_i to l_{i+1}, No. $m^{-4}s^{-1}$
b	dimensionless exponent for crystal nucleation
C	global mass transfer coefficient, kg m^{-2} h^{-1} Pa^{-1}
CPC	concentration polarization coefficient
C_p	specific heat capacity, J kg^{-1} K^{-1}
c	solution concentration, kg m^{-3} or wt%
c^*	equilibrium saturation at given temperature, kg m^{-3} or wt%
c_o	initial concentration of feed solution, kg m^{-3} or wt%
c_b	bulk concentration of salt solution, kg m^{-3} or wt%
c_m	salt concentration at membrane surface, kg m^{-3} or wt%
Δc	Difference of the supersaturation and equilibrium saturation at given temperature, kg m^{-3} or wt%
D	mass diffusivity, m^2 s^{-1}
D_t	the difference between the average pure water production flux for the three levels of each factor and the average pure water production flux for the 9 runs, kg m^{-2} day^{-1}
d_h	hydraulic diameter of the flowing channels, mm
d_i	inlet diameter of membrane fiber, mm
d_o	outlet diameter of membrane fiber, mm
d_s	housing diameter, mm
E	membrane element

E_t	tensile module, MPa
F	shear stress, N
G	crystal growth rate, m s^{-1}
Gz	Graetz number, $Gz = Re\ Pr\ (D/L)$
g	dimensionless exponent for crystal growth
H	heat transfer rate, W
ΔH_v	latent heat of vaporization, J mol^{-1}
h_f	film heat transfer coefficients from feed side, W m^{-2} K^{-1}
h_m	heat transfer coefficients of the membrane, W m^{-2} K^{-1}
h_{ms}	heat transfer coefficients of the membrane material, W m^{-2} K^{-1}
h_{mg}	heat transfer coefficients of the membrane of the vapor that fills the membrane pores, W m^{-2} K^{-1}
h_p	film heat transfer coefficients from permeate side, W m^{-2} K^{-1}
h_v	latent heat of evaporation, kJ·kg^{-1}
I	total pure water production of each subgroup in the OFF test, kg m^{-2} day^{-1}
$\bar{I}$	average pure water production of each subgroup in orthogonal test, kg m^{-2} day^{-1}
J	permeate flux, kg m^{-2} h^{-1}
K	mass transfer coefficient, m s^{-1}
K_B	nucleation rate constant, No. m^{-3-b} s^{-1+b}
K_G	crystal growth rate constant, kg^{-g} m^{3g+1} s^{-1}
k	boundary layer mass transfer coefficient, m s^{-1}
k_m	overall thermal conductivity of the membrane, W m^{-1} K^{-1}
k_g	thermal conductivity of equimolar mixtures of gas and water vapour, W m^{-1} K^{-1}
k_s	thermal conductivity of some membrane material (polymeric material), W m^{-1} K^{-1}
k_{factor}	dimensionless number of factors
M_0	initial mass of feed solution, g
L	the symbol of the orthogonal layout

L_m	effective fiber length, mm
l	crystals size, m
M	consistency index
M_0	the initial weight of feed solution, kg
M_{pro}	mass production rate per unit area of membrane, kg m^{-2} day^{-1}
M_{water}	molecular weight of water, g mol^{-1}
m_{flux}	mass of permeation flux from feed side to permeate side, kg
m_{solid}	the mass production of the NaCl crystals from the crystallizer, kg min^{-1}
m	mass of the permeate, kg
N	flow behaviour index
N_c	crystal number
Ni	number of crystals between crystal size l_i and l_{i-1}.
N_{com}	number of the comparison between simulation result and experiment data
Nu	Nusselt number
n	the population density of crystals, No. m^{-4}
n_{OFF}	dimensionless number of experiments in the orthogonal layout
$n(l)$	population density of the crystals having size l, No. μm^{-1}
P^0	saturated vapor pressure, Pa
ΔP	vapor pressure difference across of membrane, Pa
P_{fm}	saturated vapor pressure at the membrane wall on the feed side, Pa
P_{pm}	saturated vapor pressure at the membrane wall on the permeate side, Pa
Pr	Prandtl number, $c_p\mu/k$
P_{vap}	vapor pressure, Pa
Q	flowrate, L min^{-1}
q	the overall heat-transfer flux, J
q_c	the conductive heat flux q_c across the membrane, J
q_v	the latent heat transfer q_v accompanying the vapor flux, J
R	the gas constant, 8.314 J K^{-1}
Re	Reynolds number, $d_h v\rho/\mu$
R_{max}	maximum value of D_t, kg m^{-2} day^{-1}

R_{min}	minimum value of D_t, kg m^{-2} day^{-1}
r	pore size of membrane, μm
r_{ov}	the equivalent overall mass transfer resistance, Pa m^2 h kg^{-1}
r_f	resistance due to polarization effect on the feed side, Pa m^2 h kg^{-1}
r_{sl}	resistance of the scaling layer, Pa m^2 h kg^{-1}
r_m	resistance of the membrane, Pa m^2 h kg^{-1}
r_p	resistance due to polarization effect on the permeate side, Pa m^2 h kg^{-1}
S	supersaturation ratio
Sc	Schmidt number
Sh	Sherwood number
T	the difference between R_{max} and R_{min}, kg m^{-2} day^{-1}
t_{OFF}	dimensionless number of levels of each factor
T_f	bulk temperature of the feed, K
T_{fm}	temperature at the membrane wall on the feed side, K
T_p	bulk temperature of the permeate, K
TPC	temperature polarization coefficient
T_{pm}	temperature at the membrane wall on the permeate side, K
T_m	temperature at the membrane wall, K
t	time, s
Δt	time interval, s
U_b	liquid velocity of feed side, m s^{-1}
V	crystallizer volume, m^3
v	velocity, m s^{-1}
W	total water removal from concentrated salt solutions, g m^{-2}
X	dimensionless mass fraction of salt in the solution
x	the bubble size, mm
x_c	the mean bubble size, mm
x_{NaCl}	mole fraction of sodium chloride in feed side solution
x_m	dimensionless mole fraction of salt at the membrane surface on the feed side
x_w	constant in GaussAmp mathematical function

Y	average pure water production in the OFF test, kg m^{-2} day^{-1}
y	the bubbling frequency for a specific size range
y_0	constant in GaussAmp mathematical function
y_1	constant in GaussAmp mathematical function
y_n	water production of every experiment run in the orthogonal test, kg m^{-2} day^{-1}

Greek letters

α_{cal}	result from simulation modelling
$\alpha_{\exp}$	data obtained from experiments
η	thermal efficiency of the DCMD module
μ	viscosity, kg m^{-1} s^{-1}
σ	dimensionless relative supersaturation
γ	dimensionless activity coefficient
γ_{vap}	latent heat-of-vaporization, J kg^{-1}
ρ	density, kg m^{-3}
ρ_s	NaCl density, kg m^{-3}
ϕ_i	intervals of fixed crystal size, m
ϕ_v	dimensionless shape factor
Φ	flux enhancement ratio
ε	membrane porosity, %
δ_b	strain at break, %
δ_m	thickness of hollow fiber, μm
δ_{tf}	thickness of temperature boundary layer in the feed side, μm
δ_{tp}	thickness of temperature boundary layer in the permeate side, μm

Suffix

B	crystal nucleation

c	conduction
crystal	sodium chloride crystal
f	feed
fi	inlet of the membrane module in the feed side
fm	membrane wall in the feed side
fo	outlet of the membrane module in the feed side
G	crystal growth
g	gas
m	membrane surface
max	the maximum value
mean	the average value
out	out from crystallizer
p	permeate
pi	inlet of the membrane module on the permeate side
pm	membrane wall in the permeate side
po	outlet of the membrane module in the permeate side
sl	scaling layer
stable	stable state of CMDC
sus	suspension solution
v	water vapor
water	pure water
w	DCMD process with gas bubbling
w/o	DCMD process without gas bubbling

LIST OF FIGURES

LIST OF TABLES

CHAPTER 1

INTRODUCTION

1.1 Background

It has become a worldwide trend to use seawater desalination to meet the increasing demand for clean water. According to the data from the International Desalination Association (IDA) and Global Water Intelligence (GWI) DesalData (Intelligence, G.W, 2013), the total capacity of desalination plants has reached up to 6 million m^3 day^{-1} during 2013, a 50% increase on 2012.

Among the advanced water treatment techniques, reverse osmosis (RO) is the leading membrane processes for desalination due to its cost efficiency compared with other membrane processes (Greenlee, Lawler et al. 2009). However, the operation of RO process requires high pressure ranging from 15 to 70 bars and this high energy demand remains a drawback (Catherine 2009). Membrane distillation (MD) is a potential alternative to conventional seawater desalination techniques due to its moderate operating conditions and the use of low-grade waste heat or renewable energy sources. Also, during RO processing, elevated pressures are required to overcome the osmotic pressure of concentrated stream, whereas in MD, which is driven by vapor pressure difference and can be operated at atmospheric pressure, the suppression of the driving force caused by high salt concentrations within the module is limited and can be neglected. Furthermore, the solute outside the membrane distillation module has the high possibility of precipitation, which leads to the development of a hybrid process combining membrane distillation and crystallization operations (Drioli 1989).

Membrane distillation crystallization (MDC) is a combination of MD and a crystallizer (Chan, Fane et al. 2005). The pure water is produced as permeate from the MD process while the concentrated solutes can be recovered as solids from the crystallizer. This process can be economically competitive when low-grade waste heat or renewable energy resources such as solar energy are available (Lawson and Lloyd 1997; Banat, Jumah et al. 2002; Alklaibi and Lior 2005).

1.2 Challenges for high concentration MD/MDC

MD is a key part of the MDC process either for process operation or energy consumption. Both MD and MDC face the same challenges which limit the development and application. Even though MD has an obvious advantage over conventional RO as a concentration and dewatering process at high solute concentrations, it is yet to be implemented by industry or practice, let alone MDC. The reasons can be attributed to the following challenges:

1) Lack of desired membranes (flat sheet/hollow fiber membranes) specially fabricated for MD applications;
2) Flux decline in high concentration MD due to the loss of driving force and membrane permeability;
3) Lack of desired module design which can enhance heat and mass transfer efficiency in the boundary layer and avoid crystal deposits on the membrane surface;
4) Fouling/scaling formation leading to a decrease of membrane permeability at high concentration solution treatments;
5) Membrane wetting in long-term operation;
6) Lack of optimal operating regime to avoid crystal blockage in the module;
7) Relatively low gain output ratio (GOR) and cost-benefit ratio of the process (for various quality feeds and energy sources).

1.3 Objectives of this thesis

This research aims to develop methods of enhancing membrane module performance and controlling scaling formation on membrane surface in MD/MDC brine treatment processes. Specifically, the objectives of this study are as follows:

1) Design novel MD hollow fiber modules to improve liquid flow distribution for module performance enhancement, explore the mechanisms of process intensification and optimize the operating conditions;
2) Increase the shear stress to avoid crystal deposits on the membrane surface;
3) Quantify the fouling/scaling information to effectively control the scaling formation in high concentration MD/MDC process;
4) Optimize the operating regime of the hybrid process combining membrane distillation with crystallization operations.

To achieve the above-mentioned goals and explore the industrial potential of seawater desalination, deep insight into the MD process in terms of available methods of process intensification, fouling/scaling measurement methods, operating conditions and fluid dynamics, *etc*, has to be acquired.

1.4 Scope of this research

Along the lines of the above proposed objectives, this thesis provides a comprehensive literature review of prior high concentration MD works, conducts both experimental studies and theoretical analysis on the module performance enhancement and scaling control in high concentration MD and MDC processes with hollow fiber membranes. Firstly, the construction and evaluation of a bubbling-assisted DCMD module were investigated experimentally. With the encouraging results of performance improvement, an in-depth theoretical analysis was conducted to further demonstrate the working mechanism of gas bubbling on the heat-transfer intensification and scaling alleviation. Subsequently, to reveal the fundamentals of crystal deposition in the membrane module, the crystallization kinetics on the surface of polyvinylidene fluoride (PVDF) hollow fiber membranes was studied to quantify

the scaling formation in DCMD brine concentration processes. Lastly, the connection of membrane distillation and crystallization operations were systematically studied and optimized to better realize zero discharge of brine to the environment.

1.5 Organization of this thesis

Chapter 1 includes a brief introduction to the background of MD/MDC as well as a description of research objectives and scope.

Chapter 2 provides a comprehensive literature review, which summarizes the basic concepts of MD and the distinctive features of the MD operating under concentrated solutions. Specifically, the available methods for MD performance enhancement and scaling control, investigation and measurement of membrane fouling/scaling are also described in details. Besides, the review sheds light on crystallization and coupled processes of membrane and crystallization applications to provide a better understanding of the MDC process. Finally, an overview on recent works of MDC is included and the challenges and prospects for this project are summarized.

Chapter 3 presents a preliminary study to improve fluid dynamics and shear stress by introducing gas-liquid two-phase flow into the shell side of the DCMD module. This study focuses on the effect of gas bubbling on the permeation flux in a low concentration (3.5%) DCMD, including investigations on operating conditions (feed temperature and fluid dynamics) and module configuration (module orientation, length and packing density) in terms of the flux enhancement ratio, temperature polarization coefficient and global mass transfer coefficient. Additionally, the module performance and scaling status for high salt concentrations (from 18% to supersaturation) have been examined and compared in three systems (*i.e.*, modified module with knitted-spacers, original modules with and without bubbling).

Chapter 4, as an extension of the bubbling study, in-depth studied the working mechanisms of gas bubbling on the heat transfer intensification and scaling alleviation for MD brine processing. Firstly, the working mechanisms of heat-transfer

intensification using a low concentration feed/pure water were analyzed, in association with the temperature polarization coefficient and the ratio of conductive heat loss to the overall heat flux. As an ancillary work, the direct observation of bubble characteristics was conducted and analyzed, including the mean bubble size and the variance of bubble size distribution. In addition, the effectiveness of scaling control by bubbling at elevated salt concentrations in the feed steam (with NaCl as the main solute, close to saturation level) was investigated. Theoretical analysis was conducted and the specific expressions of scaling resistance associated with flux decline were derived to quantify the scaling process in DCMD with and without the bubbling system.

Chapter 5 focuses on the investigation and measurement of the scaling information in DCMD brine concentration process. The crystallization kinetics on the surface of polyvinylidene fluoride (PVDF) hollow fiber membranes was studied using sodium chloride as a model scalant. Based on experimental investigations, a mathematical model, namely crystallization on membrane surface (COMS), was developed and verified in terms of MD performance (critical point of major flux decline or scaling formation) and deposited crystal characteristics (median size and total number).

Chapter 6 studies a hybrid process that integrates MD with crystallization, namely continuous membrane distillation crystallization (CMDC). In order to improve the product recovery (pure water and solid NaCl) and better realize zero discharge from a highly concentrated NaCl feed solution (26.7 wt% salt), an orthogonal fractional factorial (OFF) experiment design was used to optimize the operating conditions, including the flow rates and inlet temperatures on both the feed and permeate sides.

Chapter 7 summarizes the overall research, presents general conclusions and recommendations for future work.

CHAPTER 2

LITERATURE REVIEW

2.1 Introduction to membrane distillation

Membrane distillation (MD) is a relatively new technique that is increasingly being studied, as it is a low cost, energy saving alternative to conventional separation processes such as traditional distillation techniques and the currently dominant desalination technique of reverse osmosis (RO). MD is a thermally driven process, in which only vapour molecules are transported through porous hydrophobic membranes. The liquid feed to be treated by MD must be in direct contact with one side of the membrane and does not penetrate inside the dry pores of the membranes. The hydrophobic nature of the membrane material prevents liquid solutions from entering its pores due to the surface tension forces. As a result, liquid/vapour interfaces are formed at the entrances of the membrane pores. Only vapour molecules penetrate the membrane pores and are cooled and condensed by low temperature liquid in the other side of the membrane. Thus, volatile compounds in feed solution can be purified by MD.

2.1.1 MD configurations

MD processes have four different configurations, which are direct contact membrane distillation (DCMD), air/gas-gap membrane distillation (AGMD), low pressure membrane distillation or vacuum membrane distillation (VMD) and sweeping gas membrane distillation (SGMD). These configurations are shown in Fig. 2.1 and described below:

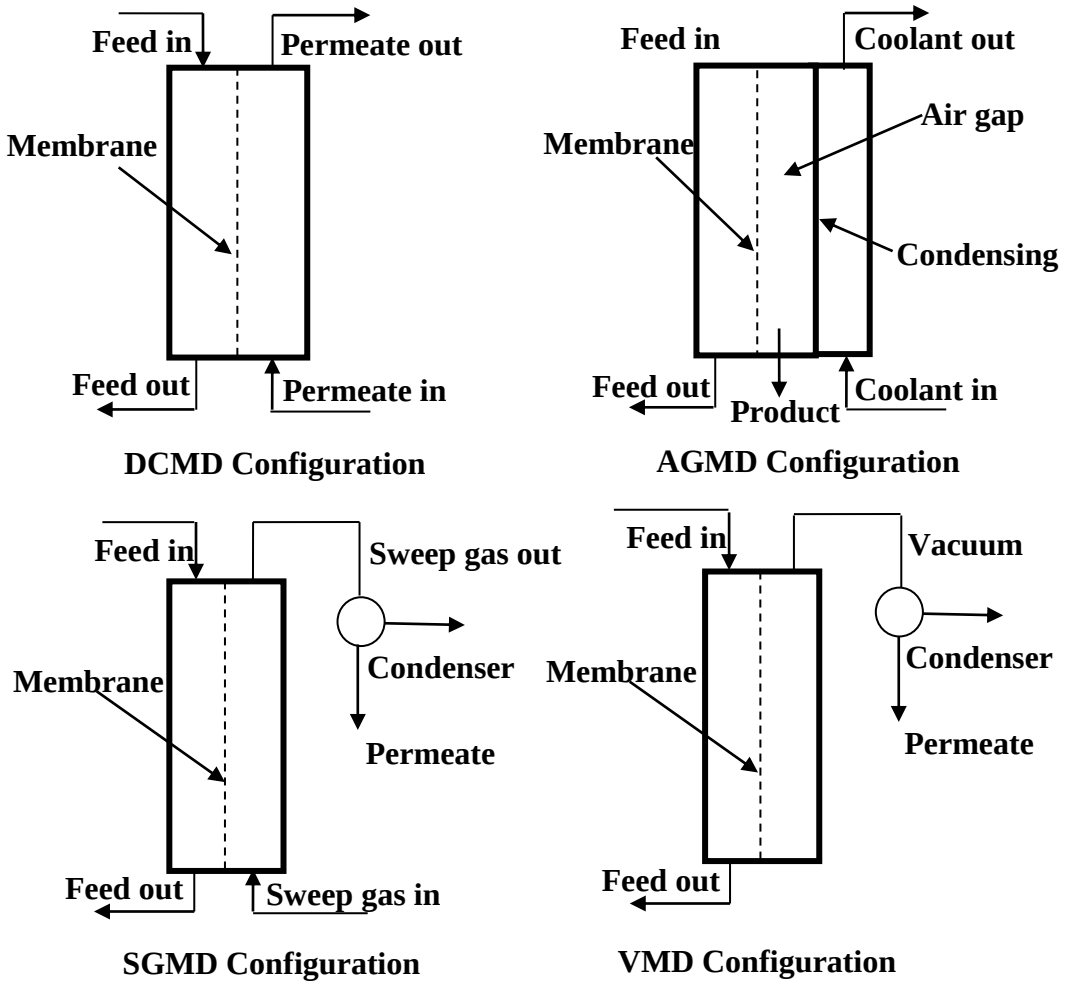

Fig. 2.1 Different configurations of the MD process, adapted from (Lawson and Lloyd 1997)

(i) In DCMD, a cooled solution is maintained in direct contact with the permeate side of the membrane while the feed side of the membrane is charged with a liquid hot feed solution. The driving force of DCMD is the vapor pressure difference induced by a trans-membrane temperature difference. Consequently, the vapour evaporating at the feed side passes through the membrane pores and condenses at the permeate side.

(ii) In AGMD, a gap filling with stagnant air is interposed between the membrane material and a cooled walling. Hence, the evaporated volatile molecules passing the membrane pores have to additionally go across the air gap to finally condense on the cooler surface.

(iii) In SGMD, the vapor molecules are swept by a cold inert gas on the permeate side and condensed in an external condenser instead of the MD module.

(iv) In VMD, once the vapor molecule passes through the membrane pores, it is sucked out of the permeate side where vacuum is applied. In this situation, condensation also takes place outside of the MD module like SGMD.

Among the four configurations of the MD process, DCMD is the simplest and oldest version. The significance of the DCMD process is that it can be operated with all types of membranes such as flat sheet, hollow fiber and spiral wound membranes.

2.1.2 Heat transfer & temperature polarization (TP) effect

In MD, the transfer process of the vapor molecules from the feed side to the permeate side leads to a heat transfer process in the membrane module. The mechanism of heat transfer in DCMD is illustrated in Fig. 2.2 in the form of a set of thermal resistances and a temperature profile. As it can be seen, heat is first transported from the feed solution with higher temperature to the membrane surface by a film heat transfer coefficient, h_f. Liquid is vaporized near the membrane wall, and the vapor passes through the membrane pores carrying heat. In this case, heat transfers the membrane by means of a volatilization coefficient, h_v. Moreover, heat conduction occurs through the membrane material and the vapor fills the membrane pores by heat conduction coefficients, h_{ms} and h_{mg}, respectively. Finally, vapor is cooled and condensed on the permeate side, which results in heat removal by the film heat transfer coefficient h_p.

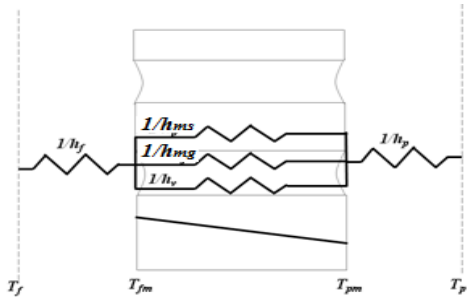

Fig. 2.2 Heat transfer resistance in DCMD, adapted from (Lawson and Lloyd 1997)

During the heat transfer process, a large quantity of heat must be offered adjacent to the membrane surface for liquid vaporization, so the rate of heat transfer in the boundary layer is often the limiting step. Commonly, the magnitudes of the heat transfer resistance in the boundary layer over the total heat transfer resistance of the system is measured by the temperature polarization coefficient (*TPC*), which is defined as:

$$TPC = \frac{T_{fm} - T_{pm}}{T_f - T_p} \tag{2.1}$$

where T_{fm} and T_{pm} are membrane wall temperatures on the feed and permeate sides, respectively. And T_f and T_p are temperatures of feed and permeate bulk fluid, respectively. For a well designed module, the *TPC* value approaches unity which indicates the limiting step is mass transfer. For a poorly designed module, the *TPC* value approaches zero which indicates the limiting step is heat transfer through the boundary layer. The temperature polarization phenomenon could be considered as a major cause of trans-membrane driving force reduction, resulting in significant flux decline in MD.

Because the temperature distribution along the membrane wall is quite complex on the feed and permeate sides with a counter-current flow pattern, T_{fm} and T_{pm} cannot be directly measured by experiments. However, for a hollow fibre membrane configuration, the values of T_{fm} and T_{pm} can be estimated based on the measured T_f, T_p and the dimensions of fibres (Chan 2005):

$$T_{fm} = T_f - (T_f - T_p)\frac{1/h_f \times d_i/d_0}{1/h_f \times d_i/d_0 + 1/(h_m + h_v) + 1/h_p} \tag{2.2}$$

$$T_{pm} = T_p + (T_f - T_p)\frac{1/h_p}{1/h_f \times d_i/d_0 + 1/(h_m + h_v) + 1/h_p} \tag{2.3}$$

where d_i and d_o are the inlet and outlet diameters of the hollow fibers, mm. h_v is the volatilization coefficient, W m^{-2} K^{-1}, which could be calculated by,

$$h_v = \frac{J\Delta H_v}{T_{fm} - T_{pm}} \tag{2.4}$$

where ΔH_v is the latent heat of vaporization, J mol^{-1}, and J is the permeation flux, kg m^{-2} h^{-1}. Additionally, h_m is the conductive heat-transfer coefficient of the hollow fibre, W m^{-2} K^{-1}, which can be expressed by (Warner and Science 1995),

$$h_m = \frac{k_m}{\delta_m} = \frac{\varepsilon k_g + (1-\varepsilon)k_s}{\delta_m} \tag{2.5}$$

In the above equation, ε is the membrane porosity (%), δ_m is the thickness of membrane, mm, and k_m is the overall thermal conductivity of the membrane, W m^{-1} K^{-1}. k_g represents the thermal conductivity of equimolar mixtures of air and water vapour in the membrane pores, and k_s refers to the thermal conductivity of polymeric material to fabricate the hollow fibre. Furthermore, h_f and h_p, the film heat-transfer coefficients on the feed and permeate sides, can be obtained by:

$$h_i = Nu_i \, k_i / d_{hi} \quad (i = f, p) \tag{2.6}$$

where d_h is the hydraulic diameter of the flow channel on the feed and permeate sides, mm. Nu_i refers to the Nusselt number which can be correlated with the Prandtl number, Reynolds number and Graetz number (Kubota, Otosaka et al. 2000).

2.1.3 Mass transfer & concentration polarization (CP) effect

The driving force of MD is the water vapour pressure difference between the feed and permeate sides adjacent to the membrane. And the mechanism of mass transfer in MD can be classified as the convective and diffusive transport of water vapour through the micro-porous membrane material. Hence, the mass transfer resistance can be simplified in terms of an electrical analog, as illustrated in Fig. 2.3. In the MD mass transfer process, indeed, the rate limiting step is often the molecular diffusion across the boundary layers on the two sides. The resistance to mass transfer within the membrane can be classified as viscous or momentum transfer resistance due to momentum transfer to the supported membrane, molecular resistance due to collisions of a diffusing molecule with other molecules, and Knudsen resistance due to the membrane itself.

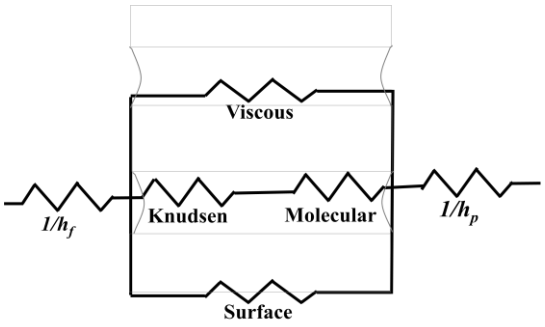

Fig. 2.3 Mass transfer resistance in MD, adapted from (Lawson and Lloyd 1997)

As the non-volatile solutes in the feed solution may retain adjacent to the membrane surface, it could result in the concentration polarization (CP) phenomenon. This phenomenon would inevitably lower the vapour pressure and hence the driving force of mass transfer. In order to quantify the CP phenomenon, the concentration polarization coefficient (*CPC*) was proposed and it can be estimated by the Nernst film model (Sherwood, Brain et al. 2000; Mengual and Peňa 1997),

$$CPC = c_m / c_b = \exp(\frac{J}{\rho K}) \tag{2.7}$$

where c_m and c_b refer to the concentration at the membrane wall and in the bulk respectively. To estimate *CPC*, the value of mass transfer coefficient within the boundary layer, *K*, is required and can be obtained using the Leveque equation at the laminar flow conditions,

$$Sh = 1.62 \times (\mathrm{Re} \times Sc \times d_h / L)^{0.3} \tag{2.8}$$

where the Schmidt number $Sc = \mu / \rho D$ and Reynolds number $\mathrm{Re} = d\upsilon\rho / \mu$

$$K = ShD / d_h \tag{2.9}$$

After simplification, *K* can be calculated by:

$$K = 1.62 \times U_b^{0.33} d_h^{-0.33} D^{0.67} \mu^{0.0} L^{-0.33} \tag{2.10}$$

At the turbulent flow conditions, Dittus-Boelter equation can be applied,

$$Sh = 0.023 \mathrm{Re}^{0.8} Sc^{0.33} \tag{2.11}$$

Hence, *K* can be obtained by:

$$K = 0.023 \times U_b^{0.8} d_h^{-0.2} D^{0.67} \mu^{-0.47} \rho^{0.47} \tag{2.12}$$

2.1.4 Benefits and limitations of MD

As a thermally driven process, only vapour molecules can transport through micro-porous hydrophobic membranes in MD. Hence, high quality pure water product can be obtained and 100% (non-volatile) solute rejection can be achieved in the MD process. Another unparalleled advantage of MD is that it can be operated under lower operating pressure, compared to other membrane processes like RO/NF which must be operated under high pressure. Consequently, the requirement for mechanical property of MD membrane is relatively low. Also, another attractive point of MD is its compact footprint and its operation requires less land and labour. Because MD is often operated at 40 ~ 90 °C, sometimes as low as 30 °C, low grade energies such as industrial waste heat, renewable energy or solar energy can meet the heat requirement of MD. From the economic perspective, a great virtue of MD is energy efficiency. It has been reported by Hogan and Fane that while utilizing solar energy the MD system is cost competitive to RO (Hogan, Fane et al. 1991).

In low concentration MD, CP phenomenon can be negligible and it has no influence on the MD flux decline. However, when the processed feed concentration increases it can still result in a consequently lower driving force and even fouling/scaling issues when the feed concentration reaches saturation/super-saturation. The formed fouling/scaling layer on the membrane surface may accelerate membrane wetting or physical damages. Besides CP, TP phenomenon is another distinguishing barrier to MD operations. There is a temperature gradient in the liquid boundary layer near the membrane wall on the both feed and permeate sides, resulting in the reduction of driving force and thus lower permeation flux. This thermal boundary layer can be disturbed by intensifying the fluid dynamics adjacent to the membrane surface. Furthermore, since the MD membranes are usually thin, the heat loss due to the conductive heat flux across the membrane also limits the thermal efficiency and thus the MD performance.

Overall, for recovering the valuable solutes and minimizing brine disposal MD is an attractive option compared to other membrane processes. Nevertheless, the implementation of MD still faces technological challenges in niche industries due to the mentioned limitations of MD, especially for at high concentration MD operations.

2.2 Membrane distillation at high salt concentrations

Most of the literatures on MD described experiments or studied theories for low-concentration solutions (Martínez-Díez and Vaízquez-Gonzaílez 1999; Martínez-Díez and Florido-Díaz 2001; Li, Xu et al. 2003; Cath, Adams et al. 2004; Macedonio, Curcio et al. 2007). As a main factor, the concentration of feed solution, of course, can affect the MD performance significantly. However, only a few papers have reported to process high-concentration solutions using MD system due to its complexity (Schofield, Fane et al. 1990; Wirth and Cabassud 2002; Yun, Ma et al. 2006). The increase of feed concentration could lead to changes in many operating parameters, such as lower feed vapour pressure, higher penetration pressure and feed viscosity, which decrease the efficiency of evaporation (Safavi and Mohammadi 2009). Several authors have reported the influence of feed solution concentration on the MD performance, which has been specifically summarized in the following.

2.2.1 Lower vapor pressure

The vapour pressure on the feed side gradually decreases with increasing the concentration of feed solution, leading to a decrease in the MD driving force and thus the MD performance. Godino et al. (Godino, Peña et al. 1997) reported that a flux of 3.37×10^{-6} m^3 m^{-2} s^{-1} could be achieved in operations with the pure water feed, while when the feed solution contained 1 M of NaCl salt the value decreased to 2.95×10^{-6} m^3 m^{-2} s^{-1}. However, when the feed concentration reached up to 5M, it was found that the flux dropped to only 0.57×10^{-6} m^3 m^{-2} s^{-1}, which is approximately 6 times lower than the value obtained with pure water feed under the same conditions. In another experiment, it was found that the flux decreased by about 20% while the feed concentration increased from 0.5 to 2 M.

2.2.2 More serious TP effect

It has been reported that a more significant increase in temperature polarization occurs with increasing concentration of sodium chloride salt solution (Martínez-Díez and Vaízquez-Gonzaílez 1999), especially at a higher operating temperature. The authors also mentioned that the heat transfer coefficient of the feed side decreased only slightly with increasing the salt concentration.

2.2.3 Slight change in *CPC*

Martinez et al. (Martínez-Díez, Florido-Díaz et al. 2000) studied the effect of feed concentration on the permeation flux using sodium chloride solutions and found the lower concentration polarization in higher feed concentrations according to their calculated *CPC* values from 1.035 for 1 M to 1.012 for 4 M. The possible reason is that the lower flux was obtained at higher feed concentration. From Martínez-Díez and Vaízquez-Gonzaílez's study (Martínez-Díez and Vaízquez-Gonzaílez 1999), it can be concluded that the concentration polarization effect could be negligible. Calabro and Drioli (Calabro and Drioli 1996) suggested that the concentration polarization effect should be paid more attentions only near saturation and it may lead to appropriately 5% of flux decay. Other works (Tomaszewska, Gryta et al. 1995) reported that the *CPC* values increased slightly with increasing the feed concentration, but the increment can be ignored.

2.2.4 Dramatic flux decline owing to fouling/scaling

If the feed concentration adjacent to the membrane wall is close to saturation/super-saturation, the evaporation and penetration of water vapour through the membrane pores could result in the salt crystals being generated and deposited on the membrane surface, leading to a decrease of the membrane permeability and thus a dramatic flux decline. Calculations made by Gryta have also proved that the formation of a depositing layer on the membrane surface limits the rate of heat transfer in MD and decreases the interfacial feed temperature (Gryta 2008).

Chan Mya Tun (Chan, Fane et al. 2005) summarized the flux profiles for MD in processing salt solutions of high concentrations as shown in Fig. 2.4. As expected, the permeation flux was higher at bigger bulk temperature difference between the feed and permeate sides as the water vapour pressure increased exponentially with the operating temperature in terms of the Antoine equation (Butcher 2008). Furthermore, the flux gradually decreased at the initial stage with the increase of feed concentration. Once the salt concentration near the membrane surface reached a critical level of supersaturation, a dramatic flux decline was observed from the curves. That is due to crystal deposition and scaling formation on membrane surface with the rapid nucleation and growth of crystals. Eventually, the membrane surface was completely covered with crystal deposits and subsequently the flux dropped to essentially zero. Fig. 2.5 also showed the images of fouled membranes covered with crystal deposits from DCMD experiments using highly concentrated NaCl feed solutions.

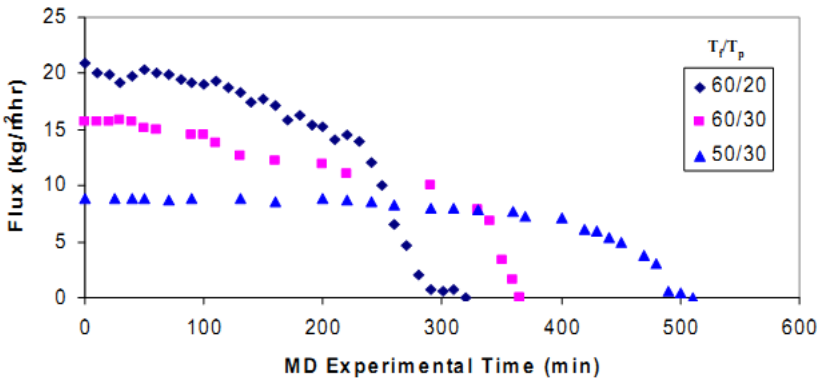

Fig. 2.4 Flux *vs.* time in processing salt solution with high concentration: (Initial feed solution concentration: 4.5 M; initial feed volume: 1500 ml; recirculation rates of feed and permeate: 3 lpm), adapted from (Chan, Fane et al. 2005)

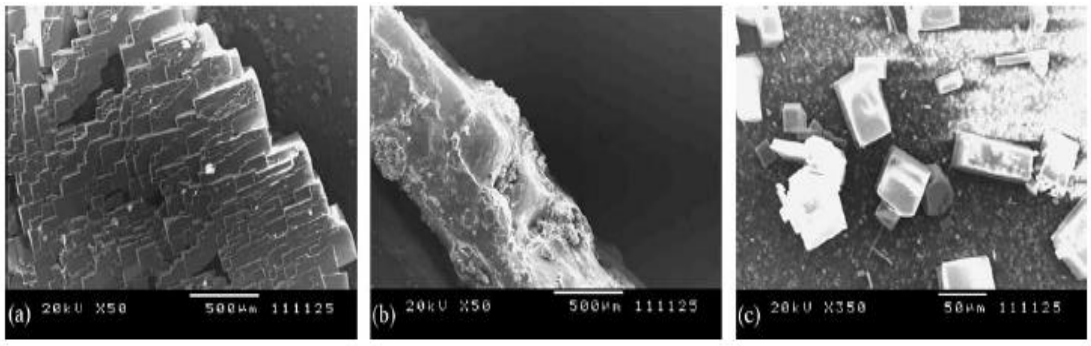

Fig. 2.5 SEM images of fouled membrane surfaces used in MD runs with high NaCl concentration: (a) top view, magnification×50; (b) cross-sectional view showing thickness of crystal deposits on the surface; (c) cubic structure of NaCl crystal deposited on the membrane, adapted from (Chan, Fane et al. 2005)

In summary, MD can be operated with aqueous salt solutions of extreme concentrations under atmospheric pressure while reasonably high fluxes could be obtained. Temperature polarization and vapour pressure lowering associated with an increase in solute concentration are the main factors for a gradual flux decrease up to a critical super-saturation, while concentration polarization can be neglected in this concentrating process. However, beyond this critical level of super-saturation, a drastic decline in flux and a rapid growth of scalants on the membrane surface are the main problems for the subsequent dramatic flux decline.

2.3 Methods for performance enhancement and scaling control in membrane process

In order to prevent the decrease in water permeation and prolong the membrane lifespan in a high concentration shell-feed MD process, hydrodynamic conditions in the module should be improved by optimizing process parameters, such as increasing flow velocities and utilizing novel module designs (*i.e.*, insertion of spacers or baffles), hence the concentration/temperature polarization effects can been mitigated (Teoh, Bonyadi et al. 2008; Yang, Wang et al. 2011). Also, fouling/scaling formation is another troublesome problem. Traditional membrane cleaning techniques (*e.g.*, backwashing and chemical cleaning) have limitations, including the deterioration of

permeate recovery after repeated backwash cycles and the disposal of chemical waste (Kobayashi, Chai et al. 1999).

This review focuses on the development of other alternative methods to increase the shear rate at the membrane surface, for example gas sparging, membrane vibration and low frequency ultrasound. These strategies include pulse flow, high shear devices (rotating and vibratory systems), two-phase flow systems, ultrasound-enhanced filtration, *etc*, which could enhance module performance and prevent the deposition of crystals on membrane surface.

2.3.1 Addition of gas bubbles in the feed side

In chemical engineering processes, it is common to inject gas bubbles to enhance heat transfer in natural convection, forced convection and fluidized beds (Kenning and Kao 1972; Kubie 1975; Kumar, Kusakable et al. 1992). Besides, it has been shown that the introduction of gas-liquid two phase flow could significantly enhance the performance of some membrane process applications (Cui, Chang et al. 2003). In membrane ultra-filtration and micro-filtration processes, the thickness and compatibility of the external fouling layers are greatly affected by the fluid dynamics of feed flow (Mercier-Bonin, Lagane et al. 2000). The use of gas bubbling to create better fluid dynamics, so as to control external fouling, was proposed by Tajima and Yamamoto in 1988 (Tajima and Yamamoto 1988). In the 1990s, a number of studies demonstrated that creating gas-liquid two phase flows on the feed side was an effective method to limit membrane fouling, with the trans-membrane flux being increased by more than 110% (Cui and Wright 1994; Cabassud, Laborie et al. 1997; Mercier, Fonade et al. 1997). Bellara et al. (Bellara 1996) proved that the liquid film thickness between the membrane wall and the slug in small diameter tubes was less than the calculated mass transfer layer thickness in single-phase liquid flow at the same liquid flow rate.

Since 2000, this field has been studied in greater detail. The mechanisms of fouling control by gas bubbling were identified and summarized as bubble induced

secondary flow and pressure pulsing (Cui, Chang et al. 2003; Ding, Liu et al. 2011). It was shown that the induced secondary flow improved the shear stress near membrane surface greatly, thus the foulant deposition was limited. Many studies focused on the measurement and calculation of this shear stress (Vera, Delgado et al. 2000; Yeo, Law et al. 2006; Yeo, Law et al. 2007; Delgado, Villarroel et al. 2008; Ratkovich, Chan et al. 2009). In addition, the effect of gas bubbling on fouling limitation was also ascribed to the induced fiber movement by passing bubbles in the submerged membrane module (Wicaksana, Fane et al. 2006). Several studies found that the efficiency of the fouling limitation was greatly affected by the size of induced bubbles, which mainly depends on the size of employed nozzles. Also, uniformly distributed fine bubbles provide better fouling control than coarse bubbles to prolong the membrane operation (Sofia, Ng et al. 2004; Lu, Ding et al. 2008). Importantly, introducing gas bubbles results in lesser risk of damaging the membrane and they are easily separated from the process stream (Cui, Chang et al. 2003).

For processes dealing with concentrated or highly viscous feed solutions, gas bubbling is also an effective means to enhance the surface shear rate to control fouling, alleviate crystal deposition and scaling formation (Vera, Delgado et al. 2000; Wicaksana, Fane et al. 2006; Yeo, Law et al. 2007; Delgado, Villarroel et al. 2008; Ratkovich, Chan et al. 2009). Introducing bubbling into the feed side of the membrane module may be a better choice to enhance the performance and postpone the crystal deposition for our studies.

2.3.2 Attaching a vibration system to the membrane module

The vibrating membrane module was first proposed by Armando et al. from New Logic International Inc (Armando 1992). This module is designated as vibratory shear enhanced processing (VSEP) and the corresponding assembly diagram is illustrated in Fig. 2.6. It can be seen that this system contains a stack of membrane plates installed in a circular casing and the bottom plate can be vibrated by an eccentric drive motor. A torsion spring was connected to the circular casing and transmitted the oscillations of a bottom disk to the entire membrane module. The top

and bottom clamshells of the membrane module were bolted together and the bottom of the lower clamshell was bolted to the top of the torsion spring. In the VSEP membrane module, the flat sheet membrane can be flatted on top of o-rings and its size cannot exceed the inner or outer perimeter of the bottom clamshell. Consequently, VSEP can disrupt the temperature and/or concentration boundary layers, fouling/scaling layers formed during the processes. Until now, many researchers have studied this dynamic device for filtration and excellent results have been reported. For example, several studies have proved that VSEP could efficiently improve the recovery of macromolecules from fermentation broths (Frenander 1996; Harscoat 1999). However, commercial successes of this device have been hampered by its mechanical complexity as well as the limited membrane area.

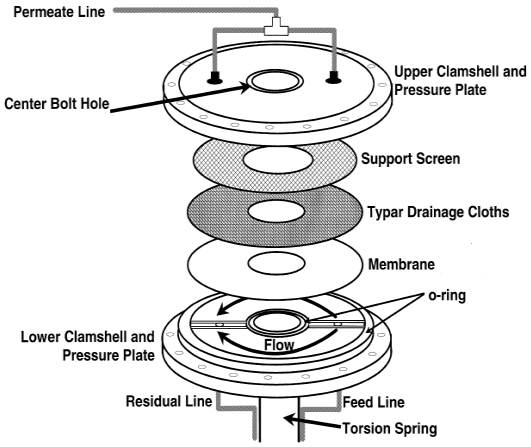

Fig. 2.6 Assembly diagram of VSEP membrane module, adapted from (Leland, Vane 1999)

More recently, another system, namely magnetically induced membrane vibration (MMV), has been reported extremely effective to mitigate fouling in MBRs (Bilad, Mezohegyi et al. 2012). A MMV system equipped in a MBR setup is shown in Fig. 2.7. It can be seen that the magnetic forces induced by a vibration engine attracts or repulses the flat sheet membrane. Either the movement of membrane to the right or left towards the narrow side of the membrane module to prevent membrane damage and reduce energy consumption. Compared to other vibration setups, MMV system

can change the operation modes at any moment as required. Hence, fouling can be controlled in real time by the MMV system induced dynamic vibration. However, both VSEP and MMV as mentioned above can be only used for flat sheet membranes rather than hollow fibre membranes, and thus the applications of these devices are limited.

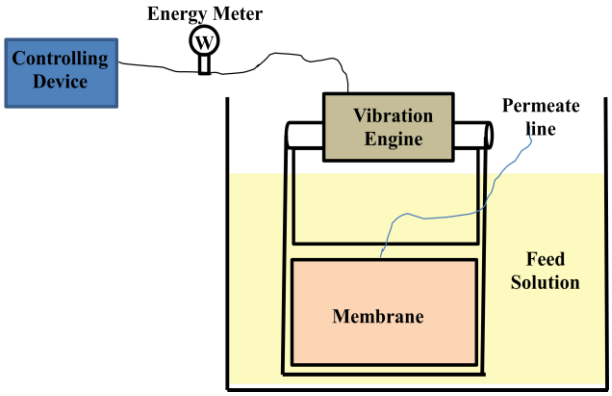

Fig. 2.7 Schematic diagram of a MBR setup equipped with the MMV system, adapted from (Bilad, Mezohegyi et al. 2012)

In recent years, the longitudinal or tensional vibration system has attracted more and more attentions which could move the submerged hollow fibre module vertically (parallel to the fibre axis) (Beier 2006; Genkin, Waite et al. 2006; Beier 2007; Prip Beier 2009; Altaee 2010). Fig. 2.8 shows a schematic diagram of a lab-scale apparatus. As it can be seen, the submerged membrane module with perpendicular hollow fibres connects with a “rotation head” by a strong spring. The rotation of the rotation head can be created in an electro motor to induce longitudinal movement along the hollow fibre membrane. The frequency of the longitudinal movement could be adjusted as required by changing the rotation speed of the rotation head. A promising improvement of fouling mitigation was obtained in this study under relatively low vibrational frequencies (ranging from 0.3 to 33 Hz). Also, Beier et al. (Beier 2006) showed great improvements of critical flux were achieved when yeast solution was filtrated using a similar vibrating vertical hollow fibre membrane module under 5 to 30 Hz frequency and 0.2 to 1.175 mm displacement. Meanwhile,

it was discovered that the critical flux increased as a power function in regard to the average shear rate near the membrane surface.

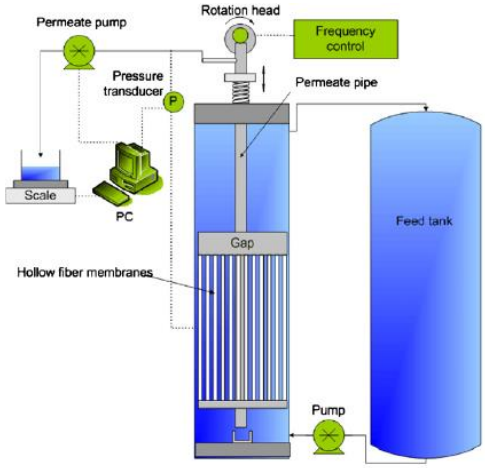

Fig. 2.8 Sketch of the experimental apparatus with longitudinal vibrations along the membrane, adapted from (Prip Beier 2009)

The vertical vibration system and combined vertical and transverse vibration system were compared in other researchers' study (Genkin, Waite et al. 2006). The compared results indicated that the latter was somewhat more efficient. A photograph and kinematic scheme of the combined vertical and transverse vibration system are illustrated in Fig. 2.9. The rotation of the rotation head can induce perpendicular and horizontal displacement of the submerged hollow fibre membrane cassette simultaneously and generate the variable shear stress adjacent to the membrane surface.

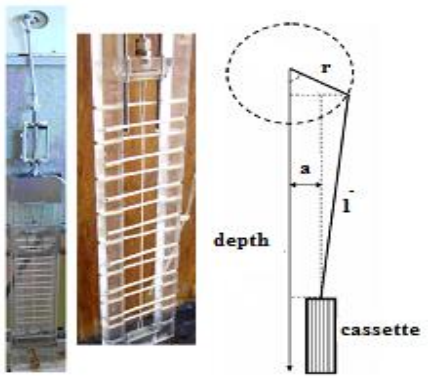

Fig. 2.9 Photograph and kinematic scheme of the vibrating unit, adapted from

(Genkin, Waite et al. 2006)

To date, a handful of literatures have reported the detailed study on transverse membrane vibration system (Kim, Garzotto et al., 2011; Kola, Ye et al. 2012; Li, Law et al. 2014; Kola, Ye et.al 2014). For instance, Kola and Ye et al. (Kola, Ye et al. 2012) found that the linearly transverse membrane vibration unit (as illustrated in Fig. 2.10) can directly generate the shear force near the membrane surface rather than induce the recirculation of bulk solution. Thus, it could limit fouling/scaling formation more effectively. Additionally, compared with vertical vibration units, the transverse vibrating system could physically separate the boundary layers from the hollow fibres, leading to more secondary flows. Because of avoiding lifting membrane modules vertically, it is expected that the transverse membrane vibration could offset the energy penalty while providing more effective local mixing. Also, the transverse vibration units could oscillate or pulse the bulk liquid.

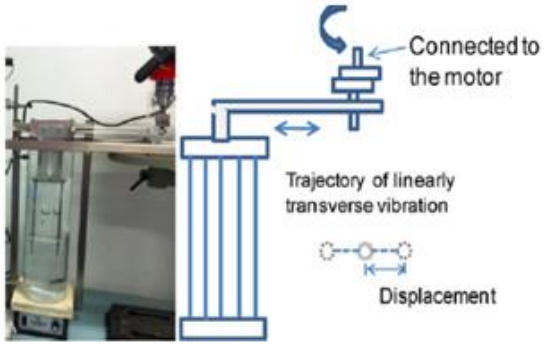

Fig. 2.10 Linearly transverse membrane vibration, adapted from (Kola, Ye et al. 2012)

In summary, vibratory systems could be integrated with the membrane process with low permeability or severe polarization. Furthermore, compared with other methods/equipments, vibration systems have competitive advantages of equipment investment and operating cost in high-salinity water treatment. Nevertheless, the potentially high demand of external energy input has also restricted the application of vibration systems.

2.3.3 Applying an ultrasound system for cleaning fouled membrane

Being recognized as a widely used technique for surface cleaning, ultrasound is a promising strategy to clean the fouled membrane. While applying an ultrasound system in membrane processes, no chemical reagent is required. And another distinct advantage of ultrasound technique is that the high performance can be remained throughout the process, not only very brief time after the implementation of cleaning techniques (Chen, Weavers et al. 2006).

The increase of permeate flux could be attributed to the effects of ultrasonic cavitations, acoustic streaming, ultrasonic-induced membrane vibration and other ultrasound principles (Zhu and Liu 2000), as illustrated in Fig. 2.11. One of the most important mechanisms is ultrasonic cavitations, which could lead to hydraulic pressure impulses through acoustically excited bubble break-ups near the membrane surface. Another main mechanism is acoustic streaming, which could induce acoustical fluctuations near the membrane surface in the form of an averaged jet stream. All these mechanisms of ultrasound could attribute to the intensification of local mixing adjacent to the membrane surface.

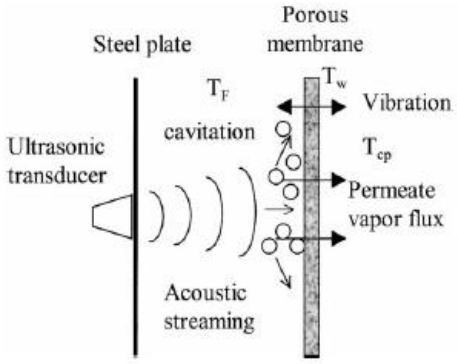

Fig. 2.11 Ultrasonic irradiation modeling system, adapted from (Zhu and Liu 2000)

Fouling/scaling control by ultrasound irradiation can be mainly contributed by ultrasonic cavitations, including micro-streaming and micro-streamers (Lamminen, Walker et al. 2004). Micro-streaming refers to the fluid circulation that frequently occurs near cavitation bubbles generated (Leighton 1994). During the compression of

cavitation bubbles, the cavitation bubbles size would oscillate resulting in the fluid circulation. The shear forces generated could detach or loosen the foulants from the membrane surface. On the other hand, micro-streamers are defined as the fluid movement caused by the motion of cavitation bubbles toward a mutual "node" or "antinode" in the fluid. An additional mechanism of ultrasound is acoustic streaming, which refers to the fluid movement induced by the absorption of acoustic energy. Acoustic streaming scours previously the foulants from the membrane surface and prevents further fouling formation. Recently, more and more authors reported that the ultrasonic technique could effectively recover and maintain the performance of membrane processes. The extent of permeate flux recovery could reach up to over 80% of the clean water test under optimal operating conditions (*e.g.*, low frequency and reasonably high power intensity) (Kobayashi, Chai et al. 1999; Kobayashi, Kobayashi et al. 2003; Kyllönen, Pirkonen et al. 2005; Muthukumaran, Kentish et al. 2005; Kyllönen, Pirkonen et al. 2006).

Notwithstanding the excellent flux enhancement ratio achieved in various membrane processes, membrane damages and even wetting are often encountered in the ultrasound applications. (Chen, Weavers et al. 2006; Lamminen, Walker et al. 2006; Li, Yu et al. 2011). For instance, Li, Yu et al. (Li, Yu et al. 2011) reported that pore dilation and breakage was induced on the hollow fibre UF membrane by the ultrasonic irradiation. Therefore, in order to ensure the integrity of membrane structure and avoid membrane wetting, cautions must be taken in selecting the operating conditions of ultrasonic intensity and irradiation duration.

2.4 Investigation and measurement of membrane fouling/scaling

As mentioned in Section 2.3, increasing the shear stress adjacent to the membrane surface can effectively mitigate fouling/scaling issue and prolong membrane lifespan. In order to develop and optimize the fouling/scaling control strategies effectively, it is necessary to observe and measure the information of fouling/scaling on the membrane surface with operation time. By probing the fouling/scaling phenomena, it can provide valuable insights into the working mechanisms of the fouling/scaling

control. Therefore, in situ monitoring techniques for membrane fouling/scaling are summarized in the review.

2.4.1 Direct observation through/above the membrane

In order to probe the particle deposition, the most straightforward method is direct observation by an optical microscope. According to this principle, a direct observation through the membrane (DOTM) technique (Li, Fane et al. 2003) was proposed and developed by A.G. Fane's research group to examine the deposition and removal of submicron bacteria during cross-flow microfiltration. The schematic diagram of DOTM technique is illustrated in Fig. 2.12. As it is shown, the key part of DOTM technique is incident-light fluorescence microscopy. A glass window is installed in the permeate chamber of the membrane module and the objective lens of the microscope is located at this glass window. For the sake of the focusing of the objective lens on to the feed side, a transparent membrane is used in the membrane module.

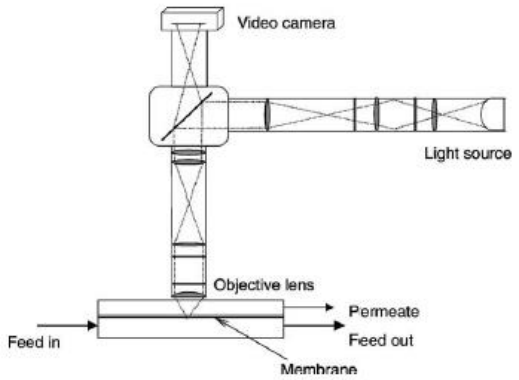

Fig. 2.12 Schematic diagram of DOTM technique, adapted from (Li, Fane et al. 2003)

However, there are several constrains for the DOTM technique to be extensive applications. Major limitations include the necessary to use a transparent membrane and to position the microscope objective at the permeate side. In order to overcome these limitations, a rectangular membrane module was designed and constructed by some researchers (Mores and Davis 2001). In the rectangular membrane channel, the

microscope objective can be installed above the membrane material to observe the foulant/scalant deposition from the feed solution. Furthermore, on the microscope objective, a CCD camera is mounted to download the images in real time to a laboratory PC for post-processing and further image analysis.

This technique can be also applied in high pressure membrane processes. Some researchers (Subramani, Huang 2009; Subramani, Hoek 2008) employed direct microscopic observation onto NF and RO membranes. Nevertheless, foulant/scalant generally requires staining in order to obtain a quite obvious contrast between the images of membrane surface and foulant/scalant layer. It restricts this technique, whether via direct visualization through or above the membrane, to merely laboratory-scale studies.

2.4.2 Laser triangulometry and optical laser sensors

In the technique of laser triangulometry, a surface of varying elevation, such as a developing particle cake layer, is focused by a laser beam (Altmann and Ripperger 1997). A CCD camera is installed to capture the reflection of the laser beam off the surface. The location where the reflected laser beam is photographed by the CCD camera will shift with the change of the surface elevation. Hence, it can build a direct correlation between the measurement of the shift and the displacement of the surface elevation. In membrane filtration process, laser triangulometry can not only measure the cake layer thickness but also probe the growth of a particle cake layer. However, this technique is limited by lacking of direct link between the cake layer thickness and rate of flux decline because the structure change of cake layer may influence the permeation flux once the cake thickness reaches a steady state.

Based on the principle of laser technique, another technique, namely an optical laser sensor, has been proposed to detect the growth of a particle cake layer (Hamachi and Mietton-Peuchot 1999; Hamachi and Mietton-Peuchot 2001). The mechanism of this technique is that light will be absorbed from a bypassing laser beam in the process of deposit layer formation. After the laser beam has traversed through the particle cake

layer, the variation of the signal intensity will correspond to the thickness of depositing layer. A calibration procedure is executed with known values of cake layer thickness to extract the correlation. This technique could make up the limitation of laser triangulometry. Also, the cake compaction can be taken into account during the operations of this technique. However, the measured maximum cake thickness is restricted by dimensions of the membrane channel and the choice of calibration procedure. According to the experimental apparatus, this restriction should be adjusted in situ.

2.4.3 Ultrasonic time-domain reflectometry (UTDR)

On the basis of ultrasonic devices, a new indirect observation technique was proven to be effective in the detection of the inorganic scaling and colloidal fouling in RO and NF recent studies (Mairal, Greenberg et al. 1999; Mairal, Greenberg et al. 2000; Cobry, Yuan et al. 2011; Lu, Kujundzic et al. 2012; Mizrahi, Wong et al. 2012; Sim, Chong et al. 2012). This technique, namely ultrasonic time-domain reflectometry (TDR), adopts sound waves to probe the location of a moving or stationary interface. This versatile measurement technique can provide information on the physical characteristics of the media through which the waves travel. Thus, ultrasonic TDR seems to be an ideal technique which is suitable for in situ monitoring membrane fouling and other phenomena of interest.

Some researchers (Mairal, Greenberg et al. 1999) used the technique of ultrasonic TDR to real-time measure the variation of Ca_2SO_4 fouling noninvasively in RO process and a good correspondence was shown between the decline in the ultrasonic signal amplitude and the growth of a fouling layer. Furthermore, the results suggested that ultrasonic TDR can partially respond to the initiation of fouling layer and its subsequent removal during membrane cleaning. Nevertheless, this technique is restricted by complex operation procedures and costly equipment to lab-scale studies.

2.4.4 Electrical impedance spectroscopy

Chilcott et al. (Chilcott, Chan et al. 2002) and Gaedt et al. (Gaedt, Chilcott et al. 2002) proposed the technique of electrical impedance spectroscopy (EIS) which can be used to investigate membrane fouling and characterize membrane properties. In this technique, in order to enhance conduction properties, the membrane surfaces are first sputtered on a metal layer. Then, by external electrical contact, an alternating current is injected directly into the membrane with the membrane edges, which results in dispersion of the current into the bulk solution and the membrane pores. This dispersion phenomenon can be characterized by the capacitance and conductance of various components in the system, such as the bulk solution and the membrane material, and the possibly existing polarization phenomenon or fouling layers. Thus, it can serve as a means to monitor in situ accumulation of foulant/scalant in membrane process by measuring the changes in the capacitance dispersion of the system.

However, this method is mainly limited by the requirement of coating of the membrane surface with thin metal films. Due to this requirement, the coating of the membrane surface not only departs from a true representation of the system but may also occlude some of membrane pores and even change the operating conditions. Therefore, it is possible that the results for in situ observation of the dynamics of fouling behaviour using this technique in membrane process are indeterminate and obscure.

2.4.5 Crystallization kinetics

In 2008, with the aid of a novel ex-situ scale observation detector (EXSOD) (Uchymiak, Rahardianto et al. 2007), Uchymiak and Rahardianto reported that the development of crystal deposits on the membrane surface can be quantified by the crystallization kinetics. They have also investigated the possibility of an early stage scaling formation before the measurable flux decline occurred. The technique can be expressed in terms of crystal nucleation and growth rate associated with operating conditions of membrane process (Nývlt 1968; Tavare and Garside 1986; Qiu and

Rasmuson 1991; Tavare 1991; Dash and Rohani 1993; Tavare 1993; Warner and Science 1995). On the basis of the principle of crystal nucleation and growth, it provides the possibility of quantifying the information on the scalant (inorganic foulant) on the membrane surface. Hence, it can quantify the scaling information accurately at any running time of membrane process, which is an overwhelming superiority of this technique.

In this thesis, we attempted to study the crystallization kinetics of sodium chloride in a polyvinylidene fluoride (PVDF) hollow fiber DCMD module. Furthermore, a new mathematical method, namely crystallization on membrane surface (COMS) modelling, combining the crystal kinetic mechanism and the transfer process in MD, was established. The developed modelling was verified experimentally in terms of MD performance (critical point of major flux decline) and deposited crystal characteristics (median size and total number). More details are illustrated in Chapter 5. Obviously, the main drawback of this technique is that it is only suitable for inorganic foulants and this limits its applications.

2.5 Crystallization and coupled process of membrane and crystallization operations

2.5.1 Basic concepts of crystallization

The crystallization process is widely used to separate, purify and produce chemicals in the chemical and pharmaceutical industries (Mersmann 2001; Myerson 2002; Ding, Liu et al. 2011). The operating conditions of this process and the crystallizer design can both affect the final crystallized products. Nevertheless, these products have high purity, crystal shape and polymorphic form. Also, the crystals should have as narrow size distribution as possible.

The deviation of the system from thermodynamic equilibrium required to change the liquid phase into solid phase is a prerequisite of the crystallization processes. This thermodynamic force is the so-called supersaturation. Common expressions for

supersaturation can be expressed as Eqs. (2.13), (2.14) and (2.15) (Mulin 1972), which contain the concentration driving force,

$$\Delta c = c - c^* \tag{2.13}$$

the ratio of supersaturation,

$$S = \frac{c}{c^*} \tag{2.14}$$

and the relative supersaturation,

$$\sigma = \frac{\Delta c}{c^*} = S - 1 \tag{2.15}$$

where c is the concentration of the solution and c^* is the equilibrium saturation at the given temperature. Fig. 2.13 shows the relationship between temperature and solubility of the components, which is requisite to create the necessary operation conditions for the crystallization process.

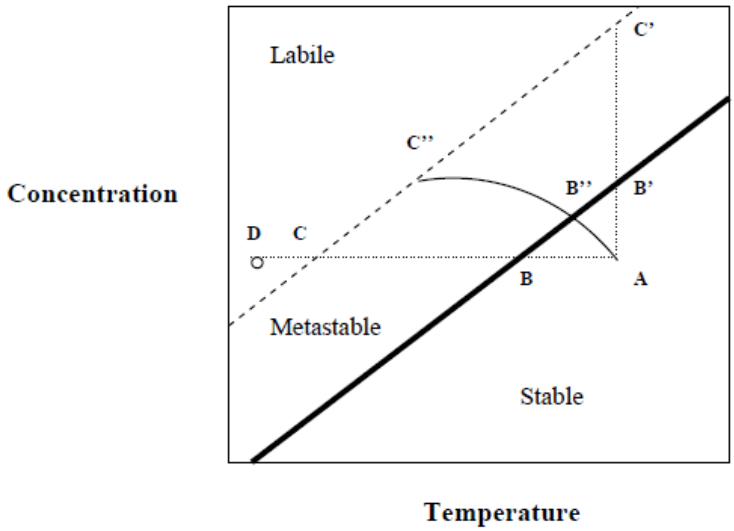

Fig. 2.13 The diagram of the relationship between solubility and temperature, adapted from (Mulin 1972)

In Fig. 2.13, the normal solubility is indicated by a solid line and super-solubility by a dashed line. The phenomenon of crystallization impossibly occurs in the stable zone due to the unsaturated status. Between the solid and dashed lines, it is the metastable zone region in which no crystallization occurs spontaneously unless seed

crystals are introduced to encourage crystal growth. Only in the labile zone region, spontaneous crystallization possibly occurs because of the supersaturation. The process of solution cooling without solvent loss is represented by Line ABC and it is expected that spontaneous crystallization probably occurs at the point C. If the substance is easily dissolved, it is often necessary to further cool the solution to the point D. Line AB′C′ shows another formation process of supersaturation by evaporating some part of the solvent at a constant temperature. Line AB″C″ represents a combined process of Line ABC and AB′C′, which often occurs in the actual application. In hybrid processes combining membrane processes with crystallization operations, the feed solution is concentrated in membrane processes and thus the desired supersaturation is generated, which can serve as the driving force of crystallization.

In all the crystallization units, various phenomena may be observed such as crystal nucleation, growth, agglomeration, breakage and even dissolution. Among them, the crystal nucleation and growth are the two predominant phenomena which are theoretical basis for most of crystallization models in the literature (Abbas and Romagnoli 2007). If the formation of crystal nucleation is subdivided, it can be divided into primary and secondary nucleation, as illustrated in Fig. 2.14. The formation of crystal nuclei primarily occurs when no solid particles of the crystallized substance exist, while nuclei are also often generated simultaneously when seed crystals present in a supersaturated solution, which is referred to as ‘secondary’ nucleation in Fig. 2.14.

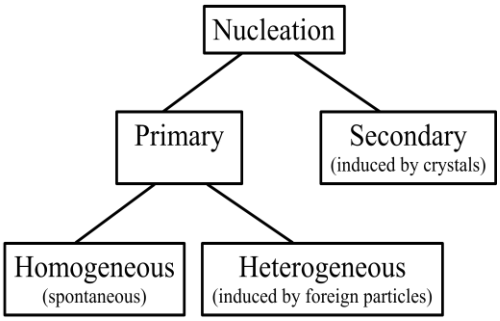

Fig. 2.14 Scheme of crystal growth due to nucleation, adapted from (Mulin 1972)

The kinetic processes of crystal nucleation and growth ('secondary' nucleation) are closely related to the size distribution of crystal products. The balanced equation for the product particles number can be expressed as Eq. (2.16).

$$\frac{dn}{dt} = \frac{\partial}{\partial L}(nG) + \frac{n\overset{o}{V}t}{V} = 0 \tag{2.16}$$

where G is the crystal growth rate, $\overset{o}{V}$ is the volume flow-rate, V is the volume of the crystallizer and t is the time. By the strict derivation of a series of formulas, the curves of crystal nucleation and growth rates can be obtained as a function of supersaturation level, as shown in Fig. 2.15.

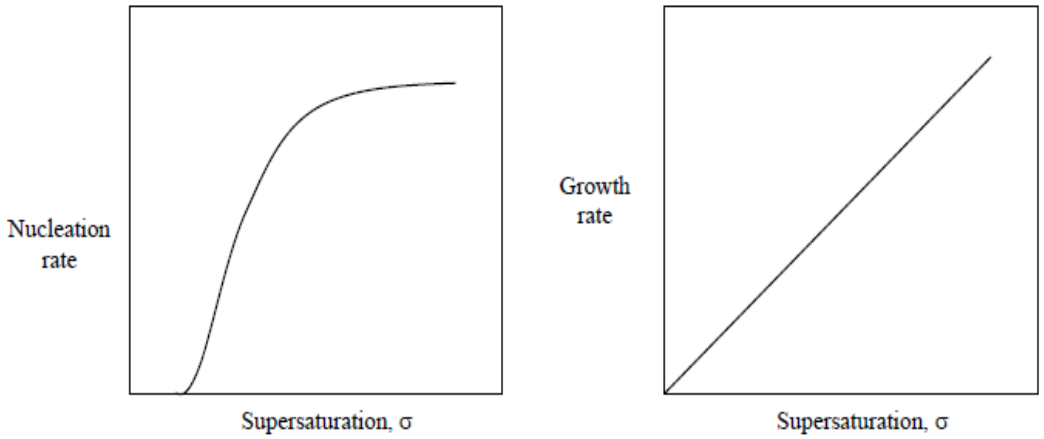

Fig. 2.15 The crystal nucleation and growth rates as a function of supersaturation, adapted from (Davey and Garside 2000)

Thus, the supersaturation is one of key linked parameters in the combined process of membrane and crystallization operations. In this integrated process, the feed solution is concentrated and a certain supersaturation level is generated in the membrane process, which serves as the driving force for crystal growth in the following crystallizer.

Due to the determination of the resulting usable properties for the crystal products, crystal size distribution (CSD) is quite an important parameter. In crystallization operations, the problems are frequently encountered associated with the crystal size

distribution (Randolph and Larson 1971). Fig. 2.16 illustrates the theoretical dependency relationship between particle mass *M(L)* and the dimensionless crystal size *l*. According to the CSD information, productivity, controlled size and shape distribution could be obtained, which is a prerequisite for the optimization of the membrane-assisted crystallization process.

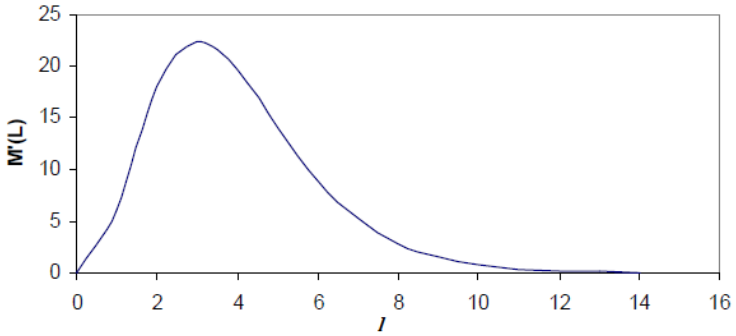

Fig. 2.16 Differential distribution of crystal size, adapted from (Nývlt, Söhnel et al. 1985)

2.5.2 Coupled processes of membrane and crystallization operations

The coupled process of membrane and crystallization operations has shown great potential for the comprehensive energy utilization and process intensification (Charpentier 2002; Stankiewicz 2003). The main characteristic features of this combined system are summarized in the following:

(i) It becomes easier to control and limit the maximum level of supersaturation because of defined mass transfer across the membrane;
(ii) It could act as heterogeneous nucleation-inducing substrates;
(iii) It is easier to control product features such as crystal size, purity and polymorphic form, shape;
(iv) It could reduce the energy consumption compared to the traditional crystallization by cooling the solution or evaporating the solvent (Fritzmann, Wintgens et al. 2007).

However, so far, only a few membrane separation processes have been used to combine with the crystallization operation, such as RO, membrane contactor, membrane templates, and membrane distillation.

2.5.2.1 Osmosis and reverse osmosis

RO is a pressure-driven process in which a semi-permeable membrane is applied to separate two different concentration solutions (Fritzmann, Wintgens et al. 2007). Because of the osmotic pressure, water is driven from the low precipitant concentration solution to the high concentration solution. Hence, the low-concentration solution is concentrated resulting in the occurrence of crystallization in the presence of a suitable precipitant. Fig. 2.17 shows the principle of osmotic dewatering (Lee 1997).

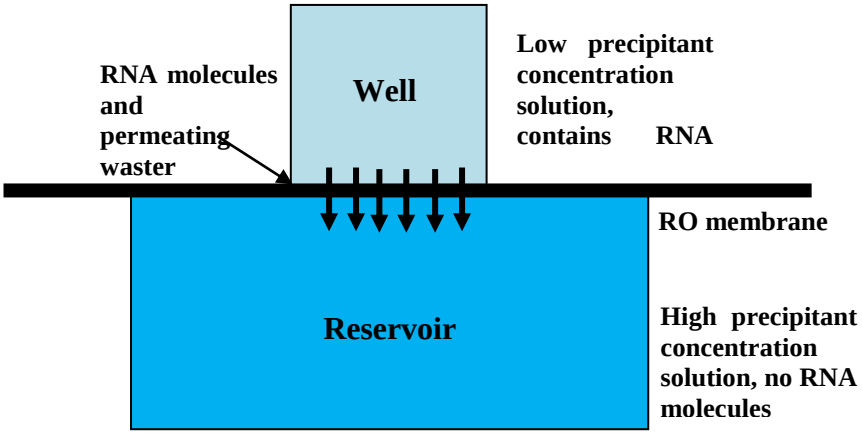

Fig. 2.17 Schematic diagram of the principle of osmotic dewatering, adapted from (Lee 1997)

Compared to traditional crystallization methods, the superiority of osmotic dewatering crystallization is that it is easy to control the quantity of water removal and in turn the supersaturation level of the concentrated solution, which significantly influences both the crystal nucleation and growth rates and further the particle size (Lee, Sportiello et al. 1997; Lee, Todd et al. 1998). Compared to the evaporative

crystallization, this method provides potential alternatives for increasing energy transformation efficiency. (Kuhn, Lakerveld et al. 2009).

2.5.2.2 Membrane contactor

The membrane contactor involves two phases: one transfers through the membrane pores and contacts with the other on the other side of membrane material. The principle of the process is illustrated in Fig. 2.18. In recent years, the membrane contactor was applied and studied in the process of precipitation and anti-solvent crystallization (Kieffer, Mangin et al. 2009). The maximum achievable supersaturation level was inspected by several mixing studies using this device. The results showed that the necessary supersaturation level can be achieved for anti-solvent crystallization. Also, because of a large quantity of membrane pores introducing feed solution, the uniform supersaturation could be created. Moreover, different from traditional tubular devices, there is substantial radial mixing in the membrane contactor. For the required typical time and the device residence time, they are comparable items (Zarkadas 2006).

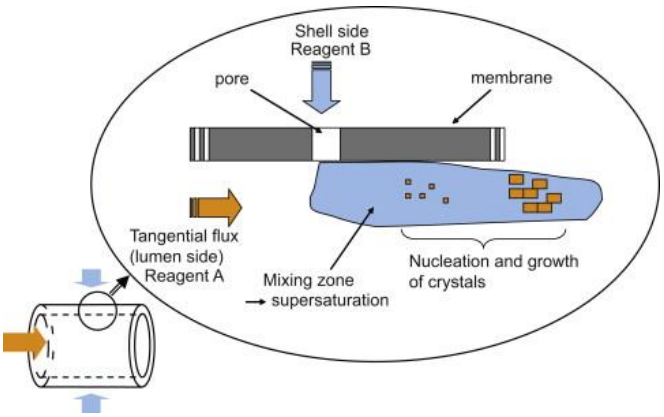

Fig. 2.18 Schematic diagram showing the principle of a hollow fiber membrane device for precipitation, adapted from (Kieffer, Mangin et al. 2009)

This device provides an interesting alternative geometry for other micro-mixers (Fritzmann, Wintgens et al. 2007). An distinct advantage of the membrane contactor is that it is easy to scale-up (Charcosset 2005; Zarkadas 2006). In order to attain the

desired conversion rate and productivity, the capability of membrane contactors can simply be improved by adding more fibres into the module and paralleling multiple devices.

However, there are also several drawbacks of the membrane contactor. For instance, the setup must be cleaned after each product run and the membrane has to be recovered its initial permeability before next run. Furthermore, like those classical membrane techniques, such as ultra-filtration and micro-filtration, membrane fouling is a big challenge during the operation, which may result in a flux drop and thus a decrease in the process yield and efficiency.

2.5.2.3 Membrane templates

In contrast to previous membrane techniques, the membrane in membrane templates is not porous but a hard template, across which no mass transfer to control the supersaturation level. The product parameters can be controlled by the size and shape of the membrane. Additionally, a lot of desired material, such as precursors, polymers, metals, semiconductors, or carbon, fills in the nano-channels between the hard templates. The formed nano-tubes, nano-rods and nano-wires can replicate the membrane size and morphology and the membrane may be removed subsequently, as shown in Fig. 2.19. (Martin 1996; Hulteen and Martin 1997; Huczko 2000; Schmid 2002; Charcosset, Fiaty et al. 2007).

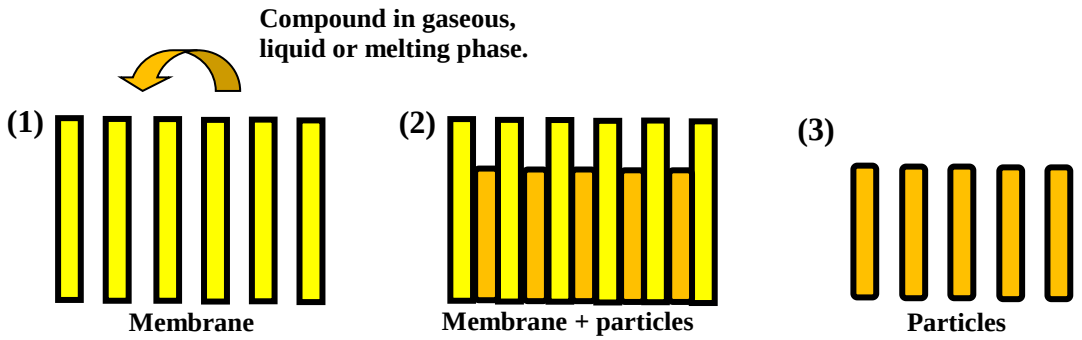

Fig. 2.19 Schematic diagram showing the membrane template method for the preparation of particles, adapted from (Chan 2005)

In the membrane template method, single crystals with unique shapes can be produced by this versatile approach. The overwhelming advantage of this method is that it is easy to control the properties of the product particles (*e.g.*, dimensions and compositions) by varying the operating conditions. Nevertheless, it is possible to cause damage to the particles during post synthesis removal of the membrane. Furthermore, the use of a membrane template restricts the process yield and the efficiency of such template-directed synthesis are probably not sufficient for the use in industry.

2.5.2.4 Membrane distillation and crystallization

Basically, MDC is the combined process of membrane distillation with crystallization. The principle of MDC is shown in Fig. 2.20. The pure water could be obtained from MD stage and the resulting supersaturation of concentrated solution can serve as the driving force of the subsequent crystallizer. Although MDC is a relatively new technology, a handful of studies of MDC phenomenon can be found in the literature (Charcosset, Kieffer et al. 2010), most of which focus on sodium chloride as a model solution. Details of the MDC process have been summarized in the next section.

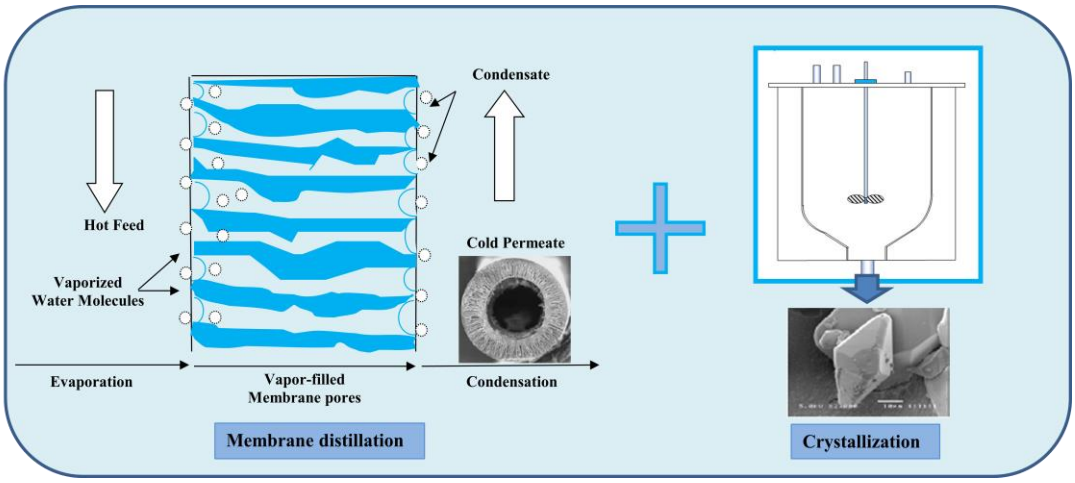

Fig. 2.20 The principle of membrane distillation crystallization

2.6 The MDC process and recent works

Recently, in order to increase the process productivity and overcome the drawbacks of the individual process, it can be seen that various hybrid processes have been developed and studied. MDC combining membrane distillation and crystallization is one of such hybrid technologies, which can be potentially applied in a range of industries, especially desalination and the concentrated aqueous solutions. The basic concept of the MDC hybrid technology is illustrated in Fig. 2.21.

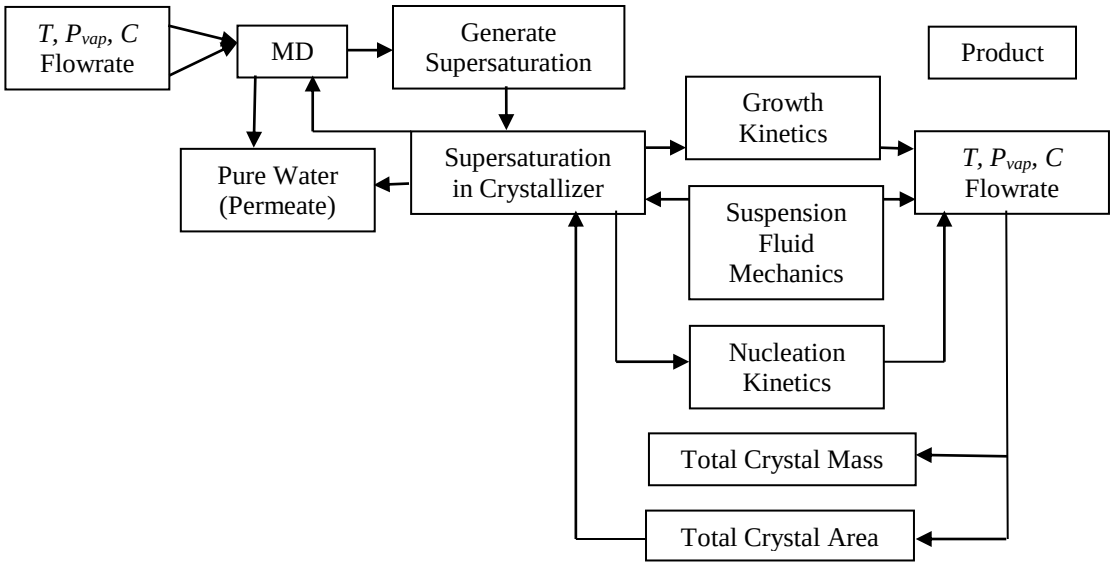

Fig. 2.21 Basic concepts of the MDC process, adapted from (Chan 2005)

In 1989, Wu and co-workers (Wu and Drioli 1989) first observed the membrane crystallization phenomenon in which the crystal deposited from the concentrated solution outside the membrane module. Also, they found that the behaviour of membrane distillation operated at high feed concentration has distinct differences from that of dilute solutions.

Later, the membrane-distillation crystallization process has been reported to be applied for treating waste water in taurine production by Wu and co-workers in 1991 (Wu, Kong et al. 1991). In their study, it was found that, after the treatment of pharmaceutical wastewater by means of membrane distillation crystallization, the dissolved taurine and NaCl can be separated according to the re-crystallization

technique and the purity of recovered taurine can reach up to 60%. Their results showed that it was required to keep enough temperature difference between the feed and permeate to run the MD process normally, especially under saturated conditions. The reason is that when the average temperature difference was only 8 K no crystal deposits occurred in the MD process until the permeate flux has dropped to zero. Unfortunately, in their study, they neglected the point of the equilibrium solubility of the taurine-NaCl-water ternary solution at operating temperatures. In the actual operation, they kept the permeate flux constant and then conducted continuous crystallization. However, no information was mentioned regarding the temperature control program and concentration change in the membrane module to keep this constant flux value. Overall, their work highlighted a great deal of potential applications of the MD-crystallization technique in industrial wastewater treatment for maximum resource recovery.

The researchers have also investigated the hybrid process combining other membrane processes with a crystallization process (Karelin, Askerniya et al. 1996). For instance, the integrated process of NF and crystallizer has been reported to treat multi-component solutions with 0.96 wt % of Na_2SO_4 and 5.2 wt % of NaCl. The capability of RO process has been also studied and the results showed that RO has an advantage of treating high concentration solutions but it is economically infeasible once the concentration of salt solutions exceeds 100 g L^{-1}.

Compared with other membrane processes, the overwhelming advantage of MD technique is low energy consumption especially the attractive economical feasibility in the treatment of high concentration solutions. Recently, it has been reported that the integrated process of DCMD and crystallization was applied to process high concentrations of salt solutions in both batch and continuous modes (Gryta 2002). In the continuous mode, a series of tanks were connected with different temperatures. It is quite necessary to consider the economic factors for the requirements of cooling water and energy. In Gryta's study, in order to achieve a flux of approximately 23 kg m^{-2} h^{-1}, the operating feed temperature was kept as high as 85°C while the permeate temperature was maintained at 20°C. Such high temperature difference may

accelerate the occurrence of membrane wetting. But the author also found that membrane wetting could be relieved by using a helically wound module and the possible reason was better flow distribution in such a module. And the productivity of the coupled process could reach up to 100 kg m^{-2} d^{-1} of NaCl.

However, if the process was operated at a low temperature, the low flux would be obtained accordingly, resulting in a practically unattractive operation and more membrane area required. In the recent studies, Curcio et al. have proved this point, and their results demonstrated that when MD was operated at 29 °C and crystallization at 25 °C the production of NaCl crystals was quite low (Curcio, Criscuoli et al. 2001). Also, they demonstrated the use of MDC in protein science to obtain the crystal product of lysozyme from supersaturated solutions and macromolecular solutions (Curcio 2002; Curcio 2003).

Another hybrid process combining an AGMD module and fluidized bed crystallizer (FBC) has been evaluated by Salah and Dahbi in 2003 (Bouguecha 2003). The results were presented including the operating conditions of AGMD, growth of the seeded particles as well as characterization of the fluidized bed. The results showed that when the feed concentration increased from 3 to 35 g L^{-1} the permeate flux accordingly decreased from 3.6 kg m^{-2} h^{-1} to 2.6 kg m^{-2} h^{-1}. This concentration used in their study is pretty low for the MD process, which has an advantage for treating high concentration solutions and even saturation solutions. The highest flux value could reach up to 7.5 kg m^{-2} h^{-1} when the operating temperature difference is 45 K. The low flux and rapid flux decline occurred even at a low concentration of 35 g L^{-1} and the possible reasons should be the unsuitable membrane material and the non-optimal module design.

The concentration polarization phenomena could accelerate the crystal deposition on the membrane surface if one kind of salt solution with positive solubility-temperature coefficient is used in the membrane process. For instance, the crystals of NaCl easily deposit near the membrane surface because its solubility decreases at relative lower temperatures adjacent to the membrane wall. Some researchers used mathematical

models to calculate the concentration and temperature distribution along the feed flow direction (Chernyshov 2003).

Due to the distinct characteristics of each inorganic salt, there are no similar results for the studies of the MDC process with different inorganic salts. In 2005, Chan Mya Tun first proposed the operating strategies for two different salts with opposite solubility-temperature coefficients (negative and positive) (Chan, Fane et al. 2005). In his study, for NaCl with a positive solubility temperature coefficient, the operation temperature in the crystallizer was maintained lower than the MD feed temperature. In contrast, for anhydrous Na_2SO_4 with a negative-temperature solubility coefficient, the crystallization temperature was higher than that of the MD feed. However, the higher temperature difference between MD feed and crystallization must be at the expense of more energy consumption.

2.7 Summary

In summary, MD can operate with aqueous salt solutions of extreme concentrations under atmospheric pressure with reasonably high fluxes. Concentration and temperature polarization as well as vapour pressure lowering associated with an increase in solute concentration cause a gradual flux decrease up to a critical super-saturation. However, flux drastic decline and scaling formation beyond this critical super-saturation are the main problems for processing high concentration MD. Traditional membrane cleaning techniques (*e.g.*, backwashing and chemical cleaning) have limitations, including the deterioration of permeate recovery after repeated backwash cycles and disposal of chemical waste. In membrane processes, other alternative methods to increase the shear rate at the membrane surface, for example gas sparging, membrane vibration and low frequency ultrasound, could be used to reduce and remove the deposition of crystals on membrane surface.

In order to develop and optimize effective scale mitigation strategies, there is a need for observation and measurement of surface fouling/scaling formation and removal. Techniques for monitoring membrane fouling/scaling were summarized in this

chapter, such as direct observation through/above the membrane, laser triangulometry, optical laser sensor, ultrasonic time-domain reflectometry, electrical impedance spectroscopy and crystallization kinetics. It is anticipated that these techniques for probing the fouling/scaling phenomena can provide valuable insights into the mechanisms controlling the fouling/scaling phenomena, which is beneficial for the commercialization of high concentration MD/MDC applications.

Additionally, the basic crystallization concepts and coupled processes of membrane and crystallization operations were briefly introduced in this chapter. The principles and advantages of the existing coupled processes, show great potential in the control of super-saturation maximum level, uniform solid product features and energy consumption reduction. A relatively new hybrid technology is membrane distillation crystallization, especially desalination and the concentration of aqueous solutions. MDC has been increasingly studied by researchers from Australia, Italy, Singapore, and Poland, and other countries. It can be seen that brine processing by MDC has the potential for the development of a technically and economically viable brine concentration process. Hence, intensifying hydrodynamic conditions and improving shear stress in the shell side of membrane module should be one of biggest challenges in industrial applications.

However, thus far there has been no related work done to develop novel methods for enhancing the hollow fiber membrane module performance and controlling scaling formation on the membrane surface in both high concentration MD and MDC processes. Thus this thesis would focus on the improvement of fluid dynamics and shear stress in the membrane module with the aid of new design module or optimizing operating regime in a high concentration process. The success of this project will have direct benefits for the water industry for enhanced water recovery and provide reduced material volume for disposal or potential solids reuse. It will also bring strategic benefits to Singapore by meeting the national goals in sustainability through water reclamation.

CHAPTER 3

PERFORMANCE ENHANCEMENT AND SCALING CONTROL WITH GAS BUBBLING IN DIRECT CONTACT MEMBRANE DISTILLATION

3.1 Introduction

As mentioned in Chapter 2, MD is well recognized as a potential alternative technology for desalination due to the benefits of moderate operating temperature with acceptable permeation rate, high salt rejection and low GHG emissions when operated with available low-grade waste heat (Kubota, Ohta et al. 1988; Lawson and Lloyd 1996; Lawson and Lloyd 1997; Banat, Jumah et al. 2002; Alklaibi and Lior 2005). Importantly, MD has an attractive advantage over other desalination processes (*e.g.* RO), which is that the elevated salt concentration in the feed stream has a smaller impact on the mass flux (Alklaibi and Lior 2005; Chan, Fane et al. 2005).

However, one of the major barriers in MD applications is the decrease of driving force due to concentration and temperature polarization phenomena (Schofield, Fane et al. 1987; Schofield, Fane et al. 1990; Calabro and Drioli 1996; Calabro and Drioli 1997; Martínez-Díez 1999; Chan 2005). In addition, if the salt concentration in the feed is close to the super-saturation, the evaporation at the membrane pores could lead to salt crystals being formed and deposited on the membrane surface, resulting in a dramatic flux decline because of the blockage of water transport passage (Chan, Fane et al. 2005). Therefore, in order to prevent the decrease of water permeation and prolong membrane life in a high concentration MD process, the surface shear near membrane surface needs to be increased, and techniques should be adopted (Teoh,

Bonyadi et al. 2008; Yang, Wang et al. 2011). Gas bubbling is one of effective ways to enhance the surface shear rate for fluid dynamic improvement and fouling control. The research finding and progress of introducing gas bubbling system into membrane processes (Cui and Wright 1994; Bellara 1996; Wicaksana, Fane et al. 2006; Cabassud, Laborie et al. 1997; Mercier, Fonade et al. 1997; Vera, Delgado et al. 2000; Mercier-Bonin, Lagane et al. 2000; Cui, Chang et al. 2003; Sofia, Ng et al. 2004; Yeo, Law et al. 2006; Yeo, Law et al. 2007; Delgado, Villarroel et al. 2008; Lu, Ding et al. 2008; Ratkovich, Chan et al. 2009; Ding, Liu et al. 2011) was summarized in Section 2.3.1. The results of these researches shown that the bubbling induced secondary flow improved greatly the shear stress near membrane surface, thus the concentration polarization was mitigated and the foulant deposition was limited. In addition, for submerged hollow fiber modules the effect of gas bubbling on fouling limitation was also ascribed to induced fiber movement.

To date the use of bubbling with MD has been limited to the studies on the MD bioreactor, in which the gas sparging serves double purposes of providing aeration and creating two-phase flow to enhance flux and control fouling (Cabassud, Laborie et al. 1997; Mercier, Fonade et al. 1997; Cui, Chang et al. 2003; Psoch and Schiewer 2006; Delgado, Villarroel et al. 2008; Phattaranawik, Fane et al. 2008). To our knowledge, no prior work on MD for high concentration applications has systematically studied gas bubbling to mitigate concentration and/or temperature polarization effects and control crystal deposition and scaling formation. The aim of this chapter is to explore the potential of gas bubbling in the MD process using DCMD with hollow fibers especially with elevated salt concentrations in the feed stream. The following aspects have been studied: (1) the optimization of process parameters in a low concentration (3.5%) DCMD process with bubbling system; (2) the evaluation of scaling status on the membrane surface in a non-bubbled and a bubbling MD system.

3.2 Theory and methodology

3.2.1 Mass and heat transfer analysis in DCMD

In a membrane separation process, the permeation flux *J* can be calculated from experimental parameters (*i.e.*, the mass of the permeate, the effective membrane area and time interval taken). Also, *J* can be determined theoretically by the product of the overall mass transfer coefficient and the 'average' transmembrane vapor pressure difference (Zhang 2010).

Due to the presence of the concentration and temperature polarization phenomena in DCMD, the wall concentrations and temperatures can be significantly different from the bulk phase. In the heat and mass transfer processes of MD, temperature polarization can affect the driving force significantly, while concentration polarization may affect the MD performance only when the feed concentration is close to the salt saturation (Martínez-Díez and Vaízquez-Gonzaílez 1999; Yang, Wang et al. 2011).

To assess the heat-transfer efficiency in DCMD, the membrane wall temperatures can be estimated from the inlet and outlet diameters of the membrane fibers, the heat-transfer coefficient of the membrane, the heat transfer coefficient associated with vapor flow, and the film heat-transfer coefficients of the feed and permeate sides, as shown in Eqs. (2.2) & (2.3). Furthermore, the heat transfer coefficients can be expressed in terms of the Nusselt number (*Nu*). And the Nu_i is correlated with the Reynolds number, Prandtl number and Graetz number. The shell-side Nu_f can be obtained via Short's equation:

$$Nu_f = 0.16 \times R_{ef}^{\ 0.6} \times \mathrm{Pr}_f^{\ 0.33} \times (\mu_f / \mu_{fm})^{0.14} \quad (200 \le \mathrm{Re}_f \le 20000) \qquad (3.1)$$

Meanwhile, the tube-side Nu_p can be calculated based on the Hausen's (Eq. (3.2)) or the Sieder-Tate's equation (Eq. (3.3)) (Perry 1997) under the respective conditions:

$$Nu_p = 3.66 + \frac{0.19 Gz_p^{\ 0.18}}{1 + 0.1117 Gz_p^{\ 0.467}} \times (\frac{\mu_p}{\mu_{mp}})^{0.14} \quad (0.1 \le Gz_p \le 100) \qquad (3.2)$$

$$Nu_p = 1.86 + Gz_p^{0.33} \times (\frac{\mu_p}{\mu_{pm}})^{0.14} \quad (Gz_p > 100) \tag{3.3}$$

where μ_f and μ_p are the viscosity at the bulk fluid temperature of the feed and permeate, and μ_{fm} and μ_{pm} are the viscosity at the heat-transfer boundary surface temperature of the feed and permeate, Pa s.

To evaluate the effect of temperature polarization phenomenon in MD, the *TPC* is defined as the deviation of the transmembrane temperature difference from the bulk temperature difference, expressed as Eq. (2.1) (Schofield, Fane et al. 1990; Yu, Yang et al. 2011). As a major cause of trans-membrane driving force reduction, the temperature polarization phenomenon could result in significant flux decline in MD.

3.2.2 Flux decline in a high concentration DCMD

As mentioned previously, the MD performance will be greatly affected by the temperature polarization due to the relationship between the vapour pressure and the temperature at the membrane surface. Also, the vapour pressure difference (driving force) is modestly influenced by the solute content when the concentration goes up to a certain level. In general, an increase in the concentration will lead to a flux decline, which is due to the reduction of vapour pressure in feed side.

Therefore, in a batch MD operation without feed supplement, a gradual increase in salt concentration of the feed solution will result in a gradual flux decline before a critical level of saturation. Once a certain super-saturation of feed solution reached adjacent to membrane surface, crystals would deposit on membrane surface and a dramatic flux decline would occur due to decrease the permeability of membrane fibres.

3.3 Experimental

3.3.1 Material properties and MD module specifications

A PVDF hollow fiber membrane made by a commercial supplier was used in this chapter. Relevant membrane properties were characterized and are reported in Table 3.1. Dynamic contact angle was measured by a tensiometer (DCAT11 Dataphysics, Germany), the mechanical strength was tested by a Zwick 0.5 kN Universal Testing Machine at room temperature and the pore size distribution were determined by a capillary flow porometer (model CFP 1500A, from Porous Material. Inc.). The performance of LEPw was measured by single hollow fiber membrane module with a dead-end. When a continuous flow of water was observed on the feed side, the applied pressure was assumed to be the membrane LEPw. Moreover, the membrane porosity is defined as the volume of membrane pores divided by the total volume of the membrane and it can be calculated according to the dimensions of the hollow fiber, the weight and density of PVDF material. From the results of characterizations in Table 3.1, it can be seen that this highly porous PVDF fiber showed reasonably high liquid entry pressure for water (LEPw), good mechanical strength, small maximum pore size and a narrow pore-size distribution.

Table 3.1 PVDF membrane properties

Dimension	**Pore size (μm)**	**Contact angle (°)**	**Porosity ε (%)**	**LEPw (bar)**	**Tensile module E_t (MPa)**	**Strain at break δ_b (%)**
d_o: 1.525mm δ_m: 206.8 μm	r_{max}: 0.125 r_{mean}: 0.082	106-120	82-88	3.5	42.05	105.4

Using this commercial hollow fiber membrane, the lab-scale MD modules were fabricated. Several fibres were potted into Teflon housings and the two ends of the housing were sealed with one kind of adhesive. Fig. 3.1 shows the photographs of the fabricated membrane module. Furthermore, the specifications of the membrane modules prepared with two different sizes of Teflon housings are listed in Table 3.2. Module #1 (d_s=6 mm) was packed with hollow fibers for flux assessment, the fiber length ranges from 210 to 480 mm and packing density from 8% to 49% for the

configuration study; while modules #2 and #3 have the same d_s of 9.5 mm and were used for scaling observation. In the design of module #3, the fibres were knitted into the mesh of the spacer, as shown in Fig. 3.2 (a)~(b)).

(a) (b)

Fig. 3.1 Photographs of (a) fabricated membrane module; (b) cross section of the module.

Table 3.2 Membrane module specifications

Experiment type	**Housing diameter, d_s(mm)**	**No. of fibers**	**Effective fiber length, L_m(mm)**	**Packing density, (%)**	**Membrane area, A(m^2)**
Module #1	6	1-6	210-480	8-49	0.001-0.006
Module #2 & #3	9.5	6	340	26	0.0098

Four different flow patterns (displayed in Fig. 3.2(c)) were used to investigate the effect of module orientation in the presence of gas bubbling in a 340 mm long module, which included the modes of 45° inclined flow, horizontal flow, vertical up-flow of feed and vertical down-flow of feed. For all other experiments, the mode of vertical up-flow of feed was adopted.

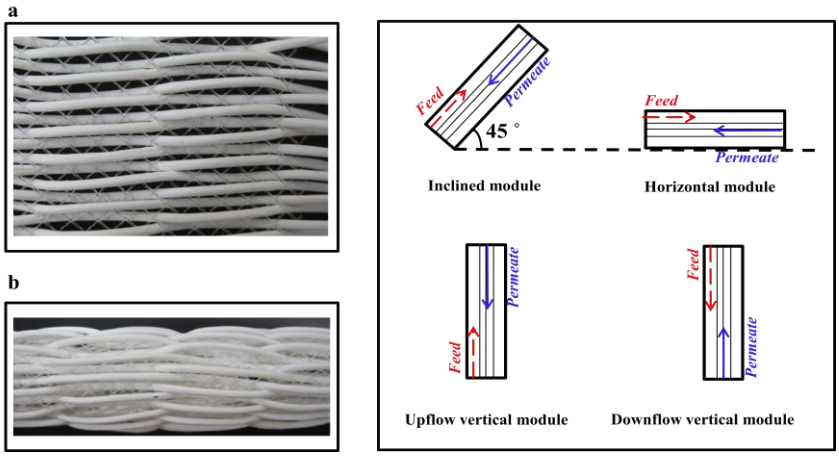

Fig. 3.2 Several explanations for MD modules (a. Fibers knitted with spacers before packing; b. Hollow fibers in the membrane module after packing; c. Membrane module orientations).

3.3.2 Bubble-assisted DCMD process set up

The DCMD equipment is shown in Fig. 3.3 with details of the bubbling set-up. As illustrated in Fig. 3.3(a), the bulk temperatures were measured by thermocouples connected to data acquisition and the flow rates were monitored by in-line digital flow meters. The water flux was measured as weight gain in the cool permeate reservoir and recorded every thirty minutes. The feed solution was heated by a heating bath (Polyscience® 9105) and the temperature of the permeate reservoir was kept constant using a cooler (Julabo® F25). The feed and permeate were circulated counter-currently using a peristaltic pump (Masterflex®, Cole Palmer). Furthermore, gas bubbling is supplied by a nitrogen cylinder. The gas inlet at the feed side entrance of the membrane module and the gas nozzle for dispersing the gas are shown in Fig. 3.3 (b)&(c).

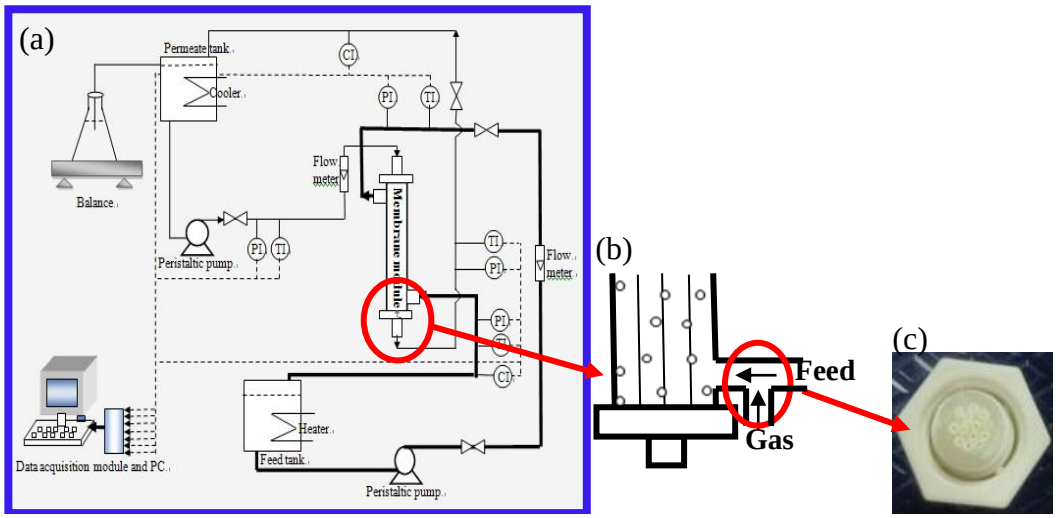

Fig. 3.3 Diagram of DCMD process with bubbling. (a. DCMD system assisted with bubbling; b. Gas inlet connected to the membrane module; c. Gas nozzle)

3.3.3 Experimental procedure and error assessment

During DCMD experiments, both the feed and permeate solutions were cycled through the hollow fibre module in countercurrent mode. On the shell side, the liquid feed (sodium chloride solution) was heated (in the range of 313~340 K) and circulated by a peristaltic pump (0.1~1 L min^{-1}). On the lumen side, the permeate side (DI water) was cooled down by a cooling circulator and cycled by another peristaltic pump (0.01~0.05 L min^{-1}). The distillate was collected in an overflow tank sitting on a balance (±0.1 g). Subsequently, the set of experiments were repeated with bubbling using the same membrane module. At the inlet of the membrane module, the gas flow from the nitrogen cylinder was added and mixed with the liquid feed, so that a two-phase flow passed over the membrane surface of the feed side.

For experiments involving crystal deposition, the DCMD system was run separately for a specified time using different modules. After high concentration DCMD experiments, the membrane modules were dismantled immediately for autopsy. The fouled hollow fibres taken from the module were cut carefully to remain the depositing crystals on the membrane. Membrane cross section and surface with non-destructive crystals were selected and made for SEM (Scanning Electron Microscope) samples. These SEM samples were then dried in the vacuum drying oven. After 12

hours, the status of scaling and crystal deposition on the samples was investigated using SEM.

To characterize the performance improvement achieved by gas bubbling, the flux enhancement ratio Φ is defined as:

$$\Phi = J_w / J_{w/o} \tag{3.4}$$

where J_w and $J_{w/o}$ are the permeate fluxes in the DCMD process with and without bubbling, respectively.

All the experiments were repeated and showed good reproducibility with water fluxes within ±8% (illustrated as error bars in the figures). The conductivity meter had an accuracy of ±0.1 ms cm^{-1} (feed side) and ±0.1 μs cm^{-1} (permeate side), respectively. The temperature and flow rate variations were strictly controlled within ±0.4 K and ±0.01 L min^{-1}, respectively.

3.4 Results and discussion

3.4.1 Process optimization in bubbling assisted DCMD process

3.4.1.1 Effect of feed temperature

In the MD process, the operating temperature is an essential parameter as the driving force increases exponentially with increasing temperature. Fig. 3.4 shows the flux enhancement ratio Φ as a function of the feed temperature. It can be seen that the water flux has increased considerably ($\Phi > 1$), which indicates that the introduction of gas bubbles has enhanced the permeation rate compared to a non-bubbling system. The enhancement may be due to the fiber movement and enhanced mixing caused by the flowing bubbles. With the flow disturbance by bubbling, the thermal boundary layer in the feed side may be reduced, leading to an increase of the trans-membrane temperature difference (driving force). As a result, the permeation rate increases significantly with the aid of bubbles.

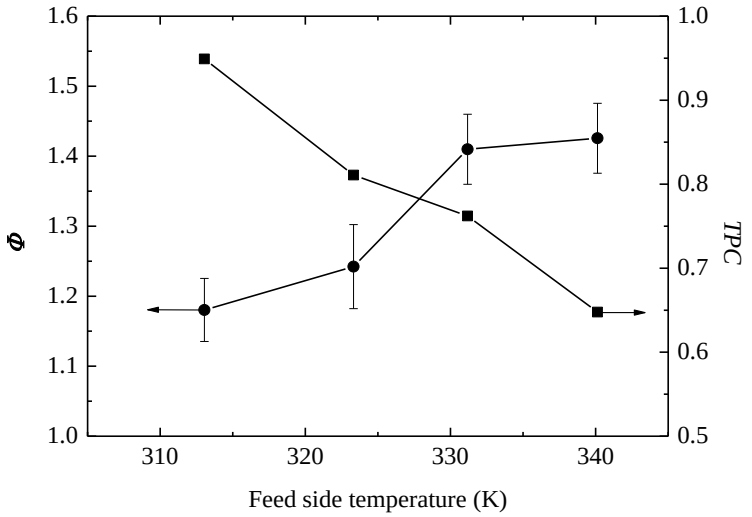

Fig. 3.4 Effect of feed side temperature on Φ in a bubbling-assisted system (Q_g = 0.2 L min^{-1}) and the calculated *TPC* values in a non-bubbling system. (3.5% NaCl solution as feed: Q_f = 0.3 L min^{-1}; Q_p = 0.025 L min^{-1}; T_p = 298 K; Module #1; Packing density: 8%; Module length: 340 mm)

In addition, it is observed that Φ increases with increasing feed temperature T_f from 1.18 (at T_f = 313 K) to 1.43 (at T_f = 340 K). This tendency illustrates that gas bubbling tends to be more effective in a higher temperature of the feed side, which can be explained by the *TPC* results shown in Fig. 3.4. It can be seen that the *TPC* decreases from 0.93 to 0.65 with increasing feed temperature from 313 K to 340 K in a DCMD system without bubbling. This decreasing trend is due to a more significant decrease of the membrane wall temperature on the feed side, T_{fm}, induced by the higher evaporation rate at a higher temperature, and a rapid increase of the wall temperature at the permeate T_{pm} caused by the condensation of a larger amount of vapor. As a result, a lower trans-membrane temperature difference (T_{fm} - T_{pm}) and hence a smaller *TPC* occur at a higher operating temperature. Thus, a more effective role of gas bubbling and a higher Φ value could be obtained at a higher operating temperature.

3.4.1.2 Effect of hydrodynamic conditions

Besides the operating temperature, another essential aspect in MD is the hydrodynamic conditions, which are associated with the feed, permeate and gas flow velocities in a bubbling-assisted DCMD system. Experiments studied the effects of gas flow rate and liquid flow velocities (characterized as Reynolds numbers, *Re*, of the feed and permeate) on the flux enhancement induced by the gas bubbling.

a) Gas flow rate under laminar and turbulent conditions

Fig. 3.5 shows the effect of gas flow rate on the flux enhancement ratio Φ under laminar (Re_f = 842) and turbulent (Re_f = 2808) flows (based on liquid flows), respectively. It is observed that these two Φ curves present a similar trend, i.e., the Φ initially increases with increasing gas flow rate (corresponding to a range of $0 \leq Q_g \leq$ 0.2 L min^{-1} for the laminar flow and $0 \leq Q_g \leq 0.5$ L min^{-1} for the turbulent flow, respectively) and then decreases at higher gas rates. The reason for the increase may be due to the greater surface shear generated by the different bubble shapes at various gas flowrates, which effectively disrupts the boundary layer and promotes local mixing near the membrane surface. Hence, the mass and heat transfer processes have been significantly intensified. Also, the secondary flow and fibre movement induced by the flowing bubbles contributed the improvement of flux enhancement ratio to some extent. However, the Φ value decreases from 1.54 to 1.26 for the laminar condition and from 1.20 to 1.07 for the turbulent flow with a further increase of gas flow rate. This may be because that the amplitude of membrane movement had reached a plateau value, and large bubbles or slugs in the feed side led to local by-passing and a lower temperatures on the feed side. Also, an unreasonably high gas flow rate might increase energy consumption and result in potential damage of the fibres. Therefore, it is necessary to identify an optimal range of gas flow rates that are able to contribute to significant enhancements of mass and heat transfer.

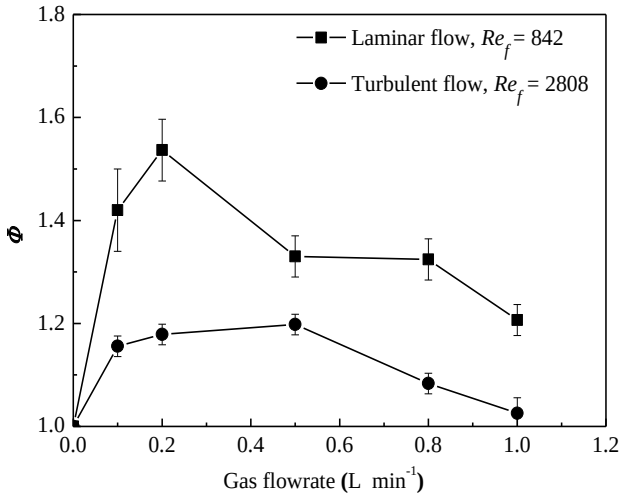

Fig. 3.5 Effect of gas flowrate on Φ in laminar and turbulent flows. (3.5% NaCl solution as feed; Re_p = 552; T_f = 333 K; T_p = 298 K; Module #1; Packing density: 8%; Module length: 340 mm)

Furthermore, Fig. 3.5 shows that the Φ value of the laminar condition is much higher than that of the turbulent flow with the other operating parameters kept constant. That is due to a thicker liquid boundary layer is apt to form and more severe temperature and concentration polarization phenomena easily occur at laminar conditions compared to a turbulent flow, where local mixing is already intensified and boundary layer minimized. Hence, the introduction of gas bubbles is more helpful for a laminar flow, due to the improved flow conditions and increased transmembrane driving force with a reduced boundary layer.

b) Flow velocities of the feed and permeate

Fig. 3.6 presents the flux enhancement ratio Φ as a function of the liquid feed flow velocity (Re_f) at a fixed gas flow rate Q_g = 0.2 L min^{-1} and fixed Reynolds number of the permeate side Re_p = 552. The results show that the Φ value decreases dramatically from 1.72 to 1.18 at a relatively low Re_f ranging from 280 to 1400. However, a fairly insignificant decrease is observed at a higher Re_f range of 1400 to 2808. The significant flux enhancement at a lower flow velocity (Re_f) could be due to an effective fiber movement and the formation of intensive vortices caused by the

bubbles, which induce local mixing and surface renewal to enhance mass and heat transfer. The decrease of the enhancement ratio Φ is probably because the original liquid boundary layer has already been effectively reduced at a high flow velocity, so that the trans-membrane temperature difference (driving force) is not much affected by the introduction of gas bubbles. Moreover, the resistance of fiber movement at a higher Re_f is higher. In this case, the introduction of gas bubbles might not be an ideal option for flux enhancement. This observation is consistent with that of Fig. 3.5.

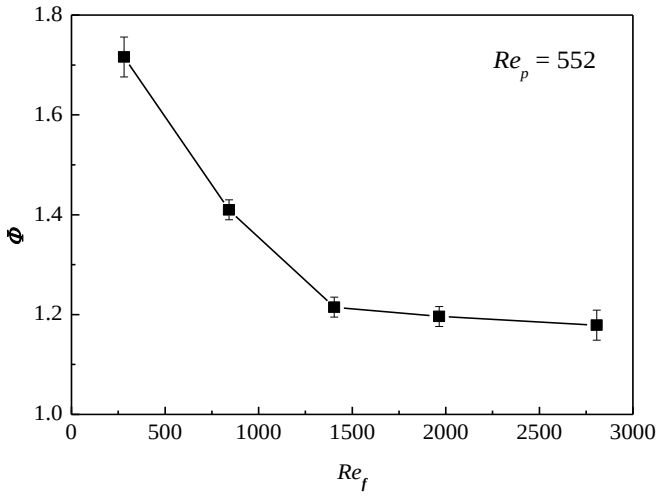

Fig. 3.6 Effect of feed side Reynolds number on Φ. (3.5% NaCl solution as feed; Q_g = 0.2 L min^{-1}; T_f = 333 K; T_p = 298 K; Module #1; Packing density: 8%; Module length: 340 mm)

Experiments were also conducted to investigate the effect of permeate flow velocity (Re_p) in the lumen on the flux enhancement ratio Φ. Fig. 3.7 plots the Φ value as a function of the Re_p (350 ~ 1200) under the same gas flow rate (Q_g = 0.2 L min^{-1}) and a fixed Reynolds number in the feed side (Re_f = 842, laminar flow). Similar to that in Fig. 3.6, the Φ value decreases with increasing Re_p. The reason may be due to increased resistance for fiber movement when the permeate flow velocity increases and hence the amplitude of fiber movement induced by gas bubbling reduces. Therefore, the local mixing adjacent to the feed-side membrane surface becomes less

intensive and consequently a lower flux enhancement ratio Φ is obtained at a higher permeate velocity.

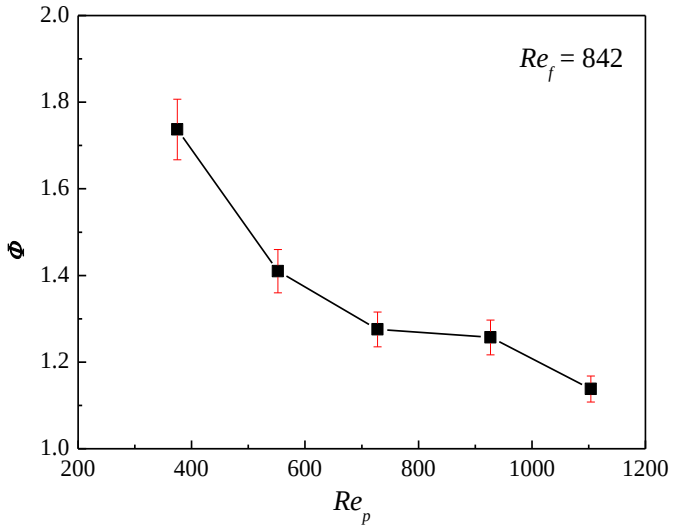

Fig. 3.7 Effect of permeate side Reynolds number on Φ. (3.5% NaCl solution as feed; Q_g = 0.2 L min^{-1}; T_f = 333 K; T_p = 298 K; Module #1; Packing density: 8%; Module length: 340 mm)

Based on the discussions of Figs. 3.6 & 3.7, lower feed and permeate flow velocities are preferable for a bubbling-assisted DCMD system, in which the local mixing near the membrane surface is intensified and the boundary layer in the feed side is disturbed physically, and hence the driving force is maximized.

3.4.2 Influence of module configuration with bubbling

In a bubbling system, module configuration is an important element for the process design. Under the same operating conditions, experiments were performed to study the effects of module orientation, fiber length and packing density on the flux enhancement with the aids of gas bubbling.

3.4.2.1 Hollow fiber module orientation

Fig. 3.8 shows the comparison of the flux enhancement ratios Φ obtained by four different module orientations in the presence of gas bubbling − 45° inclined, vertical up-flow of feed, vertical down-flow of feed and horizontal flow. With other operating parameters kept constant, the highest Φ value of 1.34 is achieved by the module with inclined 45˚ angle, followed by the vertical up-flow (Φ=1.28). The horizontal orientation gains the least enhancement (Φ=1.12). This is probably because the gas slugs in an inclined tube move faster than in a vertical and horizontal tube, which shows the smallest Φ value. The horizontal mode could also experience by-passing due to gas buoyancy. Interestingly, the vertical module with an upward flow performs better than that with downward flow. It may be attributed to a longer retention time of gas bubbling in the vertical module with an upward flow than that in vertical downward flow module.

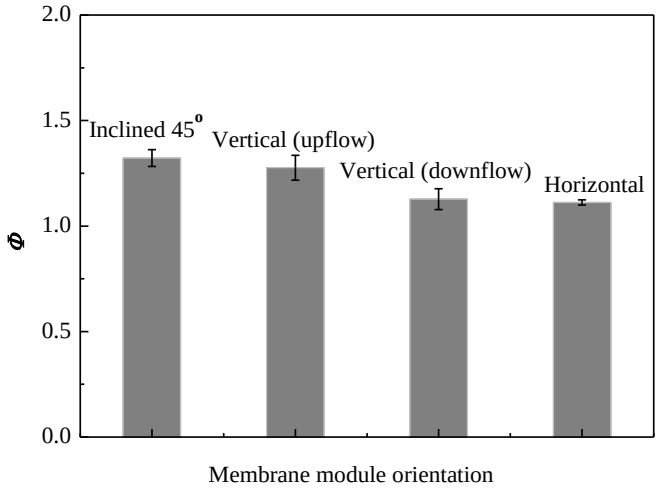

Fig. 3.8 Effect of membrane module orientation on Φ. (3.5% NaCl solution as feed: Q_f = 0.3 L min^{-1}; Q_p = 0.025 L min^{-1}; Q_g = 0.2 L min^{-1}; T_f = 333 K; T_p = 298 K; Module #1; Packing density: 8%; Module length: 340 mm)

3.4.2.2 Module length and packing density

The relationship between the flux enhancement ratio Φ and the fiber length is plotted in Fig. 3.9, which shows that the Φ value decreases with increasing module length.

This may be because the gas bubbles break and merge as they arise from the bottom. Therefore, the bubble size increases and the total number of bubbles decreases significantly along the fibers. As a result, the flux enhancement from gas bubbles is weakened as the module length increases.

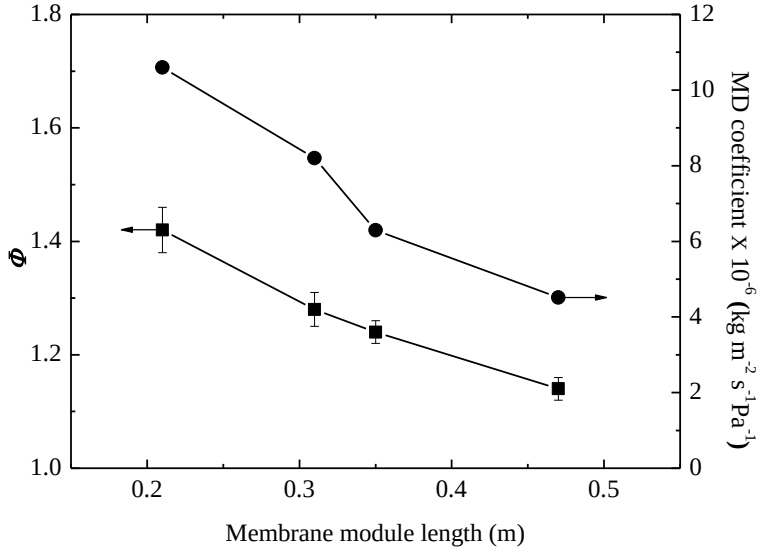

Fig. 3.9 Effect of membrane module length on *Φ*. (3.5% NaCl solution as feed: Q_f = 0.3 L min^{-1}; Q_p = 0.025 L min^{-1}; Q_g = 0.2 L min^{-1}; T_f = 333 K; T_p = 298 K; Module #1; Packing density: 8%)

The relationship between the overall mass transfer coefficient, *C*, and the fiber length is also plotted in Fig. 3.9. The *C* value was calculated from the permeation flux dividing by the log-mean vapor pressure difference for the different length modules. Similarly, the *C* value curve shows a decreasing trend with increasing module length (Yang, Wang et al. 2011). In other words, the driving force (trans-membrane temperature difference) decreases with increasing the length of the modules, which is consistent with the trend of the *Φ* curve. Overall, a reasonably short hollow fiber module is preferable for a higher enhancement ratio and *C* value in the bubbling MD process.

To further explore the effect of gas bubbles in different module configurations, Fig.

3.10 shows the flux enhancement ratio Φ and global mass transfer coefficient C as a function of module packing density. The experimental results reveal that the Φ value decreases with increasing packing density. That is probably due to the Reynolds number in a loosely packed module is lower than that of a tightly packed configuration under the same feed flow rate. The better turbulent effect caused by gas bubbling appears at a relative lower Reynolds number than a non-bubbling system, which is consistent with the result of Fig. 3.6. The global mass transfer coefficient C, as shown in Fig. 3.10, decreases as the module packing density increases (similar results obtained in (Yang, Wang et al. 2011)). This result indicates the driving force (T_{fm} - T_{pm}) decreases with increasing packing density in a MD module, as bubbles break and disappear more easily in modules packed with more fibers. Hence, better performance (higher Φ and C values) was attained in a loosely packed module. Based on the above discussion, a higher flux enhancement ratio Φ can be achieved using a hollow fiber module with an inclined orientation, shorter fibers and a lower packing density.

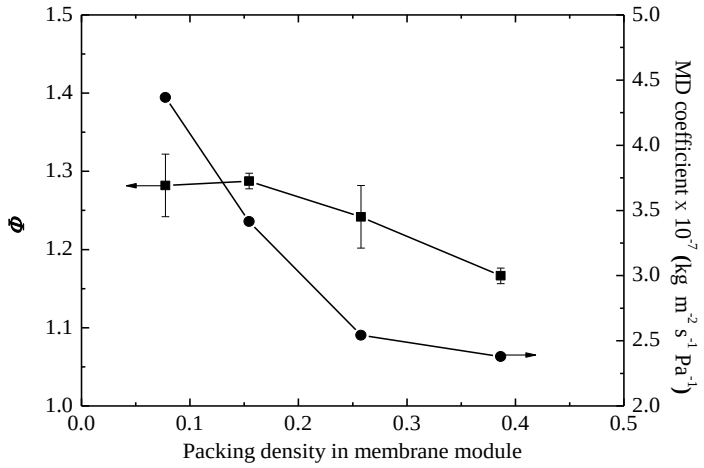

Fig. 3.10 Effect of packing density in membrane module on Φ. (3.5% NaCl solution as feed: Q_f = 0.3 L min^{-1}; Q_p = 0.025 L min^{-1}; Q_g = 0.2 L min^{-1}; T_f = 333 K; T_p = 298 K; Module #1; Module length: 340 mm)

3.4.3 Scaling control in a high concentration DCMD process

Although MD is resilient in treating high concentration brines, a rapid flux decline has been reported (Chan, Fane et al. 2005), due to the crystal deposition and scaling formation on the membrane surface in a high concentration MD system. To investigate approaches for scaling mitigation in the high concentration DCMD process, experiments were carried out using three MD systems, which involve the original modules with and without bubbling as well as a modified module with spacers, respectively. The results are compared in Fig. 3.11, which shows the trends of permeation flux and NaCl mass fraction of the effluent with operation time.

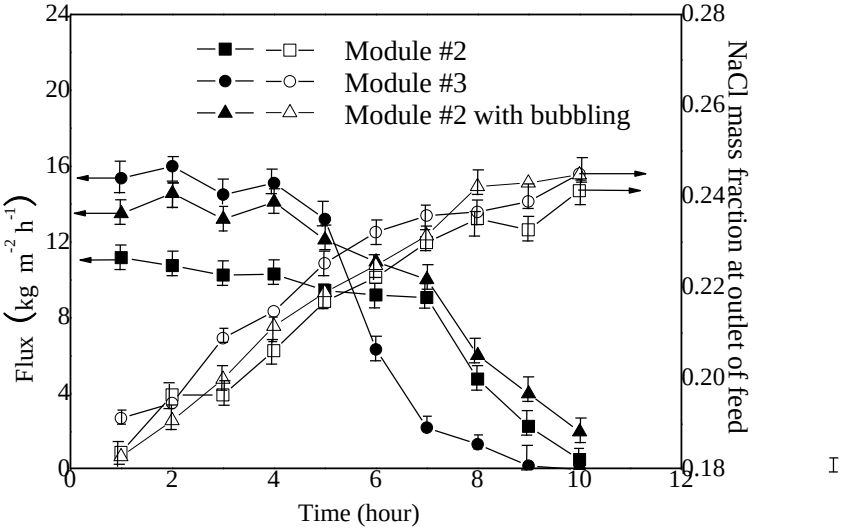

Fig. 3.11 Flux and NaCl mass fraction at outlet of feed side *vs.* time (Q_f = 0.6 L min^{-1}; Q_p = 0.15 L min^{-1}; Q_g = 0.2 L min^{-1}; T_f = 333 K; T_p = 298 K; initial feed volume: 4000 ml)

For the permeation flux, all curves under different conditions show a general decreasing trend with increasing operation time — a slow initial decrease followed by a dramatic major decline. The initial decrease is due to an increase of salt concentration and hence a slight decrease of vapour pressure difference across the membrane. It can be seen that none of the NaCl mass fractions at the outlet of the feed is higher than 27% (saturation concentration at 333 K) for the three modules.

However, due to the concentration polarization and salt accumulation on the membrane surface with time, the salt concentration on the membrane surface may be over the critical saturation point, resulting in salt crystal formation and deposition on the membrane surface. Consequently, a significant flux decline occurred, as observed in earlier studies (Chan, Fane et al. 2005).

In the initial stage, the module with spacers performs the best, followed by the original module with bubbling; while the non-bubbling original module has the lowest flux. However, a dramatic flux decline occurs to the module with spacers after 5-hour operation; while both the original modules with and without gas bubbling show prolonged critical points at the 7^{th} hour. The mass fraction of NaCl at which flux starts to rapidly decline is about 0.225 for the spacer module and > 0.23 for the other two modules. An earlier occurrence of the critical point for the module with spacers is probably due to the presence of insertions, which tend to retain NaCl crystals on the membrane surface after saturation. With the presence of gas bubbles, although the frequency of crystal collision is increased due to a decreased physical volume of the feed solution, the moving bubbles are still able to enhance the surface shear rate and clean the membrane surface to some extent. Therefore, the original membrane modules with and without bubbling show similar critical points of super-saturation. However, the membrane module with spacers has a disadvantage in the high concentration MD process.

To associate the flux decline phenomenon with the tendency of crystal deposition and/or scaling formation on the membrane surface, the membrane surfaces of the high concentration systems presented in Fig. 3.11 were examined using SEM. Fig. 3.12 shows the SEM pictures of the cross-sections and surfaces of the membranes in the three MD systems after 1-hour, 5-hour and 7-hour operation, respectively. In Fig. 3.12, no crystal deposition is observed from the cross sections or surfaces of the membrane in any of the modules after 1-hour operation. Fig. 3.13 shows the SEM images of the membrane surfaces and cross sections after 5-hour operation. Consistent with the flux results presented in Fig. 3.11, the surface of the module with spacers is almost completely covered with NaCl crystals; while the original modules

only have a relatively small amount of crystals formed, and the membranes used in the bubbling system shows the least deposition. This set of SEM pictures explains why a drastic flux decline occurs to the module with spacers after the fifth hour and a relatively slow decrease for the original modules. Taking the bubbling module as an example, the thin film induced by the slug flow can help to isolate the membrane wall from the super saturated salt solution at the liquid boundary layer. Hence, scaling formation on the membrane surface is postponed and heat transfer is enhanced under a high shear region created by the bubble flow.

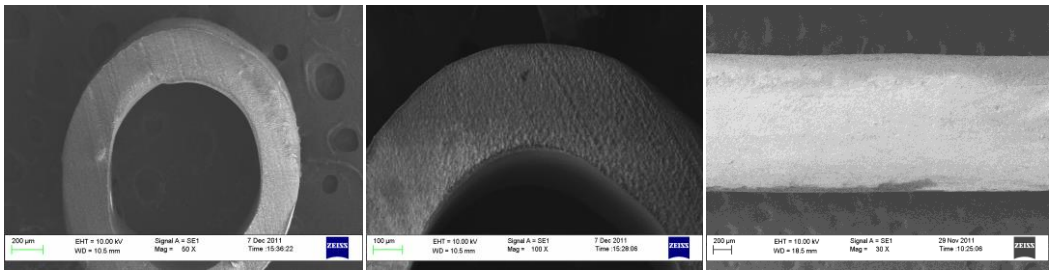

Fig. 3.12 SEM images of cross section and membrane surface after 1 hour high concentration DCMD running (Module #2&3)

Module #2

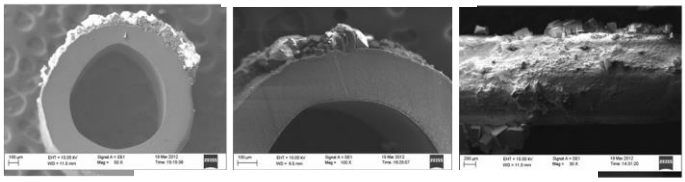

Module #2 with bubbling

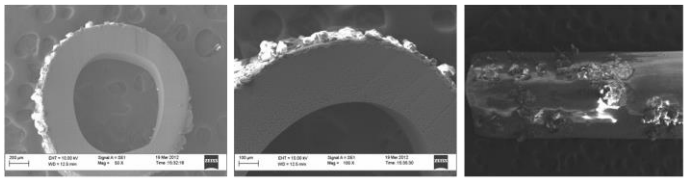

Module #3

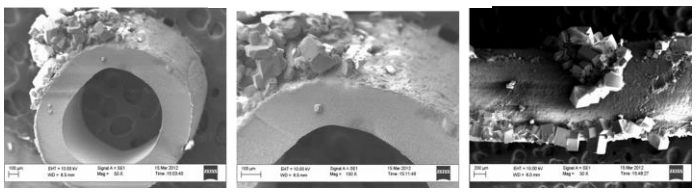

Fig. 3.13 SEM images of cross section and membrane surface after 5 hours high concentration DCMD running

Module #2

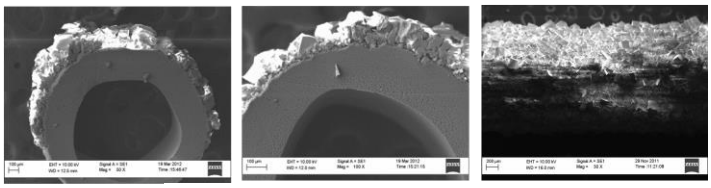

Module #2 with bubbling

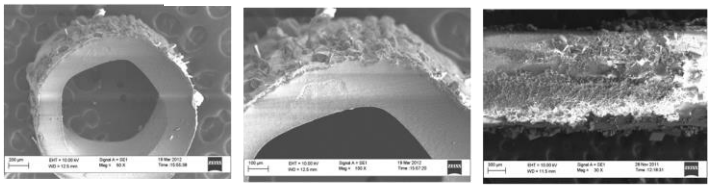

Module #3

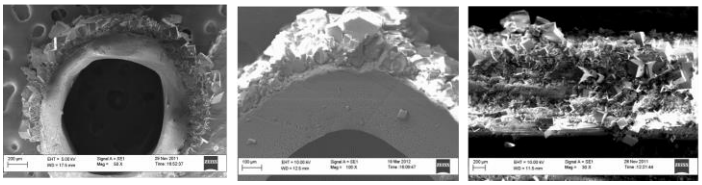

Fig. 3.14 SEM images of cross section and membrane surface after 7 hours high concentration DCMD running

After 7 hours of operation (Fig. 3.14), complete crystal coverage on the membrane surfaces for all the systems is observed. Again, this confirms the major flux decline in Fig. 3.11, which shows a similar critical point at the seventh hour for the original modules with and without bubbling. It can be concluded that the modified module with spacers is the most vulnerable to severe salt deposition within a short period of time; while bubbling can help to prolong the effective operating time with a higher permeation flux and delay the critical point for major flux decline. More importantly, it can illustrate that the module with bubbling can dispose such high concentration of feed solution, while the modified module with spacers cannot do it. However, from an applications point of view, operations close to saturation increase the risk of crystal formation and scaling.

3.5 Summary

From this chapter, it was found that in a bubbling assisted DCMD module, the permeate flux enhancement ratio could reach up to 1.72 at an optimized gas flow rate.

A higher flux enhancement ratio could be achieved at either a high feed operating temperature, low feed and permeate Reynolds numbers and a module with 45° inclined orientation, shorter fiber length or lower packing density. In all of these conditions the improved hydrodynamics due to bubbling could reduce temperature polarization. However it is observed that beyond an optimal gas flow the enhancement ratio falls, possibly due to excessive flow by-passing.

Compared to a modified module with spacers, the introduction of gas bubbles is also able to alleviate scaling formation on the membrane surface and delay the critical point of super saturation that leads to a major flux decline. These results were consistent with the membrane surface inspection by SEM, which showed that the least severe crystal deposition occurred in the original module incorporating bubbling.

Overall, the introduction of gas bubbles in the DCMD process not only mitigates the temperature polarization effect, but also enhances surface shear rate to postpone scaling formation on the membrane surface. It is beneficial to high concentration MD applications and would be studied in depth in Chapter 4.

CHAPTER 4

HEAT TRANSFER INTENSIFICATION AND SCALING MITIGATION IN BUBBLING-ENHANCED MEMBRANE DISTILLATION FOR BRINE CONCENTRATION

4.1 Introduction

Although the MD has an attractive advantage of low sensitivity to feed salinity (Schofield, Fane et al. 1990; Alklaibi and Lior 2005; Chan, Fane et al. 2005; Guan, Wang et al. 2012), technical challenges, including membrane development and polarization effects as well as fouling/scaling issues, still impede the industrialization of MD brine processing. In recent years, there is an emerging interest on novel MD membrane material development (Yang, Wang et al. 2011; Edwie and Chung 2012; Liao 2013; Liao, Wang et al. 2013) and heat/mass-transfer analysis (Alklaibi and Lior 2006; Yu, Yang et al. 2011; Yang, Yu et al. 2012; Yu, Yang et al. 2012) associated with flow studies in membrane modules (Teoh, Bonyadi et al. 2008; Yang, Wang et al. 2011; Xing Yang 2013; Yang, Fridjonsson et al. 2014) for general desalination applications. However, only a handful of papers are available in the open literature for high concentration MD systems, which are subject to surface scaling deposition and major flux decline (Schofield, Fane et al. 1990; Hsu, Cheng et al. 2002; Chan, Fane et al. 2005; Goh, Zhang et al. 2012; Guan, Wang et al. 2012; Yang, Yu et al. 2012). For instance, Chan et.al (Chan, Fane et al. 2005) observed a dramatic flux decline in the MD crystallization (MDC) brine concentration process due to crystal deposition and scaling formation on the surface of flat sheet membranes, when the feed concentration reached a critical level of supersaturation. Later on, other researchers (Edwie and Chung 2013) found that the flux declined rapidly at higher

feed temperatures (*e.g.,* 70 ^{o}C), which was attributed to membrane scaling and wetting accelerated by salt saturation within the boundary layer in hollow fiber-based MDC module. Nevertheless, thus far only few attempts have been made to explore the intensification methods for improving thermal efficiency and mitigating scaling formation in MD brine processing (Ding, Liu et al. 2011; Chen, Yang et al. 2013), not to mention a lack of development on scaling control strategies associated with quantitative resistance analysis of the scaling layer.

Chapter 3 has demonstrated that a bubbling-assisted MD system can achieve up to 72% flux enhancement and effectively postpone the occurrence of critical point of flux decline caused by the supersaturation of salt solution (Chen, Yang et al. 2013). Yet, gas bubbling has only been recently reported in the MD process, not to mention the studies on working principles for improving heat transfer and alleviating fouling. For example, a recent MD study has examined the effectiveness of intermittent gas bubbling on the concentration process of Chinese tea extract in terms of foulant removal rate and fouling resistance analysis (Ding, Liu et al. 2011). However, a comprehensive evaluation is still to be carried out for characterizing the performance of two-phase flow MD system and distinguishing the intensification effect from bubbles of different properties (size & size distribution, *etc*). Hence, as an extension of the bubbling studies, this current chapter aims to explore the working mechanisms of gas bubbling on heat transfer intensification and scaling alleviation for MD brine processing.

In this current work, the bubble characteristics (*i.e.,* bubble size and bubble size distribution) were quantified through the mathematical function GuassAmp (*i.e.,* Amplitude version of Gaussian peak function), with the aid of direct observation on the flowing bubbles in the MD module. An in-depth theoretical analysis is conducted to further demonstrate the benefits of utilizing gas bubbling for MD heat-transfer intensification, via the calculation of heat-transfer and temperature-polarization coefficients. Also, the effectiveness of scaling alleviation in two-phase flow MD with supersaturated feed solution is evaluated through the scaling resistance, which is quantified based on the resistance-in-series theory. The practicability to operate the bubbling-assisted MD process beyond supersaturation is also investigated.

4.2 Theory

4.2.1 Assessment of heat transfer process intensification by bubbling

4.2.1.1 Heat transfer mechanisms in DCMD

Theoretically, the permeation flux of DCMD *J* could be calculated in term of the transmembrane temperature difference, as:

$$J = C\frac{dP}{dT}|_{T_m}\ (T_{fm} - T_{pm}) \tag{4.1}$$

where *C* is the overall mass transfer coefficient (Yu, Yang et al. 2011), kg m^{-2} s^{-1} Pa^{-1}. T_m is the membrane temperature, K. T_{fm} and T_{pm} are the membrane surface temperature on the feed and the permeate sides, K, respectively. By assuming that the temperature polarization effect is similar on both sides of the membrane, T_m can be estimated by $(T_f + T_p)/2$. The above equation is accurate with $(T_{fm} - T_{pm})$ less than 10 K and pure water used as feed. In this case, the Clausius-Clapeyron equation is applicable to determine the vapor pressure gradient dP/dT across the membrane (Yang, Wang et al. 2011),

$$\frac{dP}{dT}|_{T_m} = \frac{P\gamma_{vap}M_{water}}{RT^2}|_{T_m} \tag{4.2}$$

where γ_{vap} is the latent heat-of-vaporization, J kg^{-1}, M_{water} is the molecular weight of water, g mol^{-1}, *R* is the gas constant (8.314 J K^{-1}) and *P* is obtained from the Antoine equation (Sherwood, Pigford et al. 1975).

The overall heat-transfer flux in MD, *q*, consists of the conductive heat flux q_c across the membrane and the latent heat transfer q_v accompanying the vapor flux *J* (Hsu, Cheng et al. 2002):

$$q = q_c + q_v = (\frac{k_m}{\delta_m})(T_{fm} - T_{pm}) + \gamma_{vap}C\frac{dP}{dT}|_{T_m}\ (T_{fm} - T_{pm}) = H(T_{fm} - T_{pm}) \tag{4.3}$$

where *H* is the overall heat-transfer coefficient based on the transmembrane temperature difference, δ_m is the wall thickness of the membrane, and k_m is the overall thermal conductivity of the membrane, W m^{-1} K^{-1}. The k_m/δ_m value of the PVDF fiber used in this study is determined as 274 W m^{-2} K^{-1} (Sarti, Gostoli et al. 1985). The overall heat-transfer flux can be re-expressed as:

$$q = h_f (T_f - T_{fm}) = h_p (T_{pm} - T_p) \tag{4.4}$$

where h_f and h_p are the local heat-transfer coefficients for the hot feed and the cold permeate sides, respectively, J K^{-1}. Defined as the fraction of effective driving force $(T_{fm} - T_{pm})$ over the total thermal input $(T_f - T_p)$, the temperature polarization can be quantified via the combination of Eqs. (4.3) and (4.4), as:

$$(T_{fm} - T_{pm}) = \frac{T_f - T_p}{1 + H / h_f + H / h_p} = TPC \times (T_f - T_p) \tag{4.5}$$

Therefore, *TPC* can be determined through the calculation of various heat transfer coefficients. Combing Eqs. (4.1) with (4.5) for dilute solutions

$$J = C \frac{dP}{dT} (T_f - T_p) / (1 + H / h) \tag{4.6}$$

where *h* is termed as the overall film heat transfer coefficient $1/(1/h_f + 1/h_p)$. Substituting the definition of *H* ($H = C\gamma_{vap} dP/dT + k_m / \delta_m$ from Eq. (4.3)) into Eq. (4.6) and rearranging gives:

$$\frac{\Delta T}{J \gamma_{vap}} = \frac{1}{dP/dT} \frac{1}{C \gamma_{vap}} (1 + \frac{k_m / \delta_m}{h}) + \frac{1}{h} \tag{4.7}$$

Therefore, with the measurable quantities k_m / δ_m, $\Delta T = T_f - T_p$ and *J* as well as the predetermined points of *dP/dT* from Eq. (4.2), the unknown parameters *h* and *C* can be calculated from the intercept and the slope by plotting $\Delta T / J \gamma_{vap}$ against *1/(dP/dT)*(Schofield, Fane et al. 1987). Hence, the temperature polarization coefficient (*TPC*) and ratio of conductive heat loss q_c/q can be quantified.

According to the above mechanism of heat transfer analysis in DCMD, the comparison of the overall film heat transfer coefficient *h*, *TPC* and conductive heat loss q_c/q with and without gas bubbling can be determined to indicate the intensification effect on heat and mass transfer in two-phase flow MD. Also, the MD performance improvement can be evaluated by the flux enhancement ratio Φ (Eq. (3.4)).

4.2.2 Analysis of scaling resistance in DCMD with and without bubbling

4.2.2.1 Resistance-in-series heat transfer model for general DCDM with scaling

In DCMD, by introducing the equivalent overall mass transfer resistance, r_{ov}, the trans-membrane flux J can be re-expressed as (Martínez and Rodríguez-Maroto 2007):

$$J = \frac{P_f - P_p}{r_{ov}} \tag{4.8}$$

where P represents the vapor pressure of the bulk fluid, Pa; f and p denote feed and permeate, respectively. The vapor pressure difference ($P_f - P_p$) is the equivalent overall driving force for mass transfer in DCMD, corresponding to the bulk temperature difference ($T_f - T_p$).

In the high concentration brine treatment process using batch-mode DCMD, scalant components such as NaCl tend to nucleate from the liquid phase due to super-saturation of the feed solution. As a result, the crystal particles would deposit on the membrane surface and form a scaling layer because of the membrane-solute interaction, which may greatly reduce the local driving force (transmembrane vapor pressure difference) and impose an additional heat-transfer resistance in MD (Chan, Fane et al. 2005). Nevertheless, compared to pressurized membrane processes (Singh and Sirkar 2012), the scaling layer in MD composed by NaCl crystals is much thinner and hence negligible to account for the hydrodynamic resistance of the bulks. Based on the temperature profiles across the entire domain in DCMD with scaling formation, as illustrated in Fig. 4.1, this overall driving force can be divided into four parts (Singh and Sirkar 2012):

$$P_f - P_p = (P_f - P_{sl}) + (P_{sl} - P_{fm}) + (P_{fm} - P_{pm}) + (P_{pm} - P_p) \tag{4.9}$$

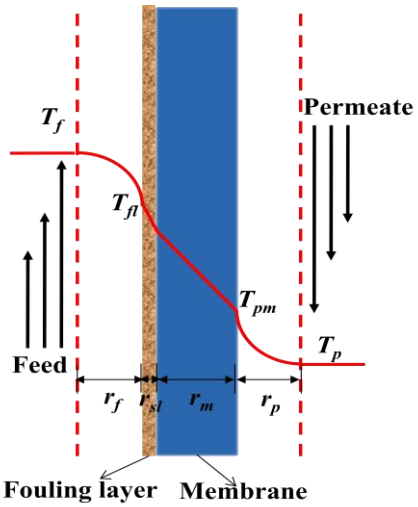

Fig. 4.1 The temperature and resistance profiles in DCMD with membrane fouling/scaling

Also, the overall heat-transfer resistance r_{ov} consists of four steps in series: (1) resistance due to polarization effect on the feed side, r_f; (2) resistance of the scaling layer, r_{sl}; (3) resistance of the membrane, r_m; (4) resistance due to polarization effect on the permeate side, r_p. Hence, the r_{ov} can be expressed as:

$$r_{ov} = r_f + r_{sl} + r_m + r_p \tag{4.10}$$

in which r_f, r_{sl}, r_m and r_p represent the respective local vapor pressure drop per unit flux generated (Pa m^2 h kg^{-1}) associated with the decrease of temperature due to the heat transferred across step 1 to 4.

4.2.2.2 Quantification of scaling-layer resistance with and without bubbling

In high concentration DCMD with continuous scalant nucleation and deposition adjacent to the membrane surface, the scaling layer thickens along the operation time. At the beginning of NaCl scaling formation, *i.e.*, time t = 0 when r_{sl} = 0, based on Eq. (4.8) the initial trans-membrane flux can be expressed as:

$$J_{w/o|t=0} = \frac{P_f - P_p}{r_{f_{w/o}} + r_m + r_p} \tag{4.11}$$

Hence, the overall resistance of non-bubbling DCMD is written as:

$$r_{f_{w/o}} + r_m + r_p = \frac{P_f - P_p}{J_{w/o|t=0}} \tag{4.12}$$

With an increasing number of crystals depositing on the membrane surface at $t = t_1$, when $r_{sl} \neq 0$, the permeation flux can then be calculated as:

$$J_{w/o|t=t_1} = \frac{P_f - P_p}{r_{f_{w/o}} + r_m + r_p + r_{sl\_w/o}} \tag{4.13}$$

By combining Eqs. (4.11), (4.12) and (4.13) and rearranging, the scaling-layer resistance of the non-bubbling DCMD system $r_{sl\_w/o}$ at $t = t_1$ can be quantified as:

$$r_{sl\_w/o} = (\frac{J_{w/o|t=0}}{J_{w/o|t=t_1}} - 1) \times \frac{(P_f - P_p)}{J_{w/o|t=0}} \tag{4.14}$$

With the introduction of gas bubbles in DCMD, only the hydrodynamics (boundary layer) at the feed side would be affected while the rest of the local resistances remain unchanged. Thus, the trans-membrane flux of a bubbling-assisted DCMD system $J_{w|t=0}$ and $J_{w|t=t_1}$, at t=0 and t=t_1, respectively, are expressed as:

$$J_{w|t=0} = \frac{P_f - P_p}{r_{f_w} + r_m + r_p} \tag{4.15}$$

$$J_{w|t=t_1} = \frac{P_f - P_p}{r_{f_w} + r_m + r_p + r_{sl\_w}} \tag{4.16}$$

Similar to the derivation of Eq. (4.14), the overall resistance of a bubbling-assisted DCMD is written as:

$$r_{sl\_w} = (\frac{J_{w|t=0}}{J_{w|t=t_1}} - 1) \times \frac{(P_f - P_p)}{J_{w|t=0}} \tag{4.17}$$

In a word, the scaling-layer resistance in DCMD with and without bubbling can be quantified as a function of time t through Eqs. (4.14) and (4.17), respectively, where the permeation fluxes $J_{w|t=0}$, $J_{w|t=t1}$, $J_{w/o|t=0}$ and $J_{w/o|t=t1}$ can be obtained experimentally and the corresponding vapor pressure P_f & P_p can be calculated based on known temperature conditions (T_f & T_p) using the Antoine equation (Sherwood, Pigford et al. 1975).

4.2.3 Bubble characteristics in two-phase flow

With the gas stream continuously introduced into the membrane module, bubbles of various shapes and sizes are formed depending on the gas flow rate, gas sparger dimension and fluid viscosity. The number of bubbles in a sufficiently small size domain, namely frequency, could quantify bubble characteristics under certain bubbling conditions. A built-in GaussAmp mathematical function was applied to the changing curves of frequency with the bubble size (bubble size distribution) in Origin software (OriginLab 2014):

$$y = y_0 + y_1 e^{(-\frac{(x-x_c)^2}{2x_w^2})} \tag{4.18}$$

where y is the bubbling frequency for a specific size range, x is the bubble size, mm, y_0, y_1, x_c and x_w are constants. Based on Eq. (4.18), the bubble size distribution curve of a two-phase flow could be obtained accordingly, including key parameters such as the mean bubble size, x_c, and variance of size distribution, x_w^2. Thus, the module performance can be associated with the bubble characteristics under various bubbling conditions.

4.3 Experimental

4.3.1 Material properties, module fabrication and gas sparging

In this chapter the same polyvinylidene fluoride (PVDF) hollow fiber membrane as those used in Chapter 3 was used to fabricate lab-scale membrane modules. Relevant membrane properties are listed in Table 3.1 and the module specifications are listed in Table 4.1. To introduce gas bubbles into the MD system, specially-designed modules with gas sparger, as illustrated in Fig. 4.2a, were fabricated by potting the PVDF hollow fiber membranes into an 85 mm × 8 mm × 256 mm rectangular Teflon housing. Six 1-mm diameter pinholes as gas inlets were created and evenly distributed at the bottom of the module; they were then connected to a nitrogen cylinder to introduce even bubble distribution inside the membrane module, as presented in Fig. 4.2b. It is noted that the modules were installed in a vertical orientation to maintain regular bubble shape and movement. Also, for direct observation and image collections of the bubbles, a transparent module housing/shell was adopted and a scale was attached to the observation region to measure bubble

size with varying flow rate, as shown in Fig. 4.2c. Hence, bubble images can be clearly captured and analyzed under various gas flow rates, which were measured by a gas flow meter (Dwyer, 0.1~1.0 L min^{-1}). The bubble characteristics, *i.e.*, mean bubble size and variance of bubble size distribution can be obtained according to Eq. (4.18).

Table 4.1 Membrane module specifications

Modules	**Module width (mm)**	**Module depth (mm)**	**Effective fiber length *L* (mm)**	**No. of fibers**	**Membrane area, (cm^2)**
#1	85	8	256	6	73.6
#2				35	429.1

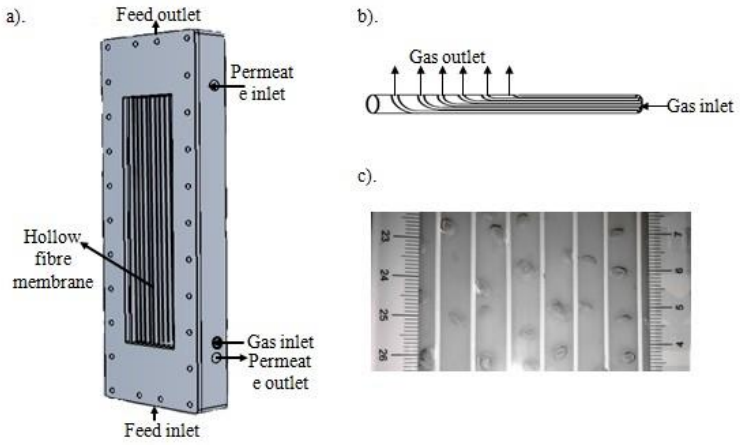

Fig. 4.1 The schematic diagram of (a) bubble-assisted membrane module, (b) gas sparger and (c) direct observation window for bubble flow

4.3.2 DCMD experiments

In this study, three sets of MD experiments (as shown in Table 4.2) were carried out: 1) Set A, to study the effect of gas flow rate on the bubble characteristics and MD performance, with 3.5 wt% NaCl solution as feed; 2) Set B, to analyze the local heat-transfer resistance under different bubble flow conditions, via pure water tests; 3) Set C, to investigate the growth of NaCl scaling resistance on the membrane surface and anti-scaling efficiency by gas bubbles, with 7.0 kg 23.5 wt% NaCl solution as feed. The Module #4 (6 hollow fibers packed) was used in Set A experiments for conveniently capturing and analyzing bubble characteristics; while Module #5 (35

fibers packed) was employed for Sets B and C experiments to minimize the experimental errors from permeation flux fluctuation.

Table 4.2 MD experiments

	Module	Initial feed solution	Feed temperature (K)	Permeate temperature (K)	Feed flowrate (L min^{-1})	Permeate flowrate (L min^{-1})
Set A	Module #4	3.5 wt% NaCl solution	330	299	0.41	0.15
Set B	Module #5	Pure water	300 ~ 340	292 ~ 328	0.41	0.15
Set C	Module #5	23.5 wt% NaCl solution	334	294	0.41	0.28

All the experiments were conducted in a batch-mode DCMD setup, which was described in Chapter 3. In brief, both the feed and permeate streams were circulated countercurrently through the shell and lumen sides of the hollow fiber modules by peristaltic pumps (Masterflex®, Cole Palmer), respectively. The effect of gas flow rate on module performance was investigated at 0.2 L min^{-1}, 0.5 L min^{-1} and 0.8 L min^{-1}, respectively. The permeation flux was recorded and measured in every 10 minutes. In addition, the operating temperature ranges were deliberately controlled for different sets of experiments. For instance, in Set B pure water tests, the feed-side temperature T_f was kept in a range of 300 K ~ 340 K; while the permeate-side temperature T_p was varied between 292 K ~ 328K, respectively, to ensure a transmembrane temperature difference lower than 10 K (Schofield, Fane et al. 1987). For Set C tests with highly concentrated feed, the T_f and T_p were kept at 334 K and 294 K, respectively. The starting point ($t = 0$) for scaling formation (saturation concentration of NaCl solution) was identified and marked when a dramatic flux decline was observed during the batch-mode operation (Chan, Fane et al. 2005).

It is noted that the Sodium chloride used to prepare the synthetic brine was purchased from Merck with an analytical purity of 99.5%. All the experiments were repeated three times and showed good reproducibility with water fluxes within ± 5%. The conductivity meter had an accuracy of ±0.1 ms cm^{-1} (feed side) and ±0.1 μs cm^{-1}

(permeate side), respectively. The temperature and flow rate variations were strictly controlled within ±0.4 ℃ and ±0.01 L min^{-1}, respectively.

4.4 Results and Discussion

4.4.1 Heat transfer process intensification by bubbling

4.4.1.1 Permeation flux *vs.* gas flow rates

Fig. 4.3 shows the ratio of flux enhancement Φ (Eq. (3.4)) as a function of gas flow rate based on the results of Set A DCMD experiments with low salinity feed. Clearly, the Φ values for all gas flow rates are above unity, which is mainly due to the two-phase flow intensification effect on mass and heat transfer. With the improved flow mixing and intensified surface shear rate induced by bubbling, the thickness of the feed-side thermal boundary layer adjacent to the membrane surface is greatly reduced, leading to an increase of driving force (*i.e.,* trans-membrane temperature gradient, vapor pressure difference) and subsequently the permeation rate. Interestingly, it is observed that the Φ initially increases till reaching a maximum value of 1.27 at Q_g = 0.2 L min^{-1} and then slightly decreases with increasing gas flow rate. The slight decrease of Φ with a further increase on the gas flow rate may be caused by the formation of large bubbles or slugs resulting in local channeling/by-passing and uneven flow distribution, which slightly offsets the flux enhancement ratio Φ due to the negligible increment of the surface shear intensity at a higher gas flow (Section 4.2.3). Hence, finer bubbles tend to be more effective in terms of performance enhancement.

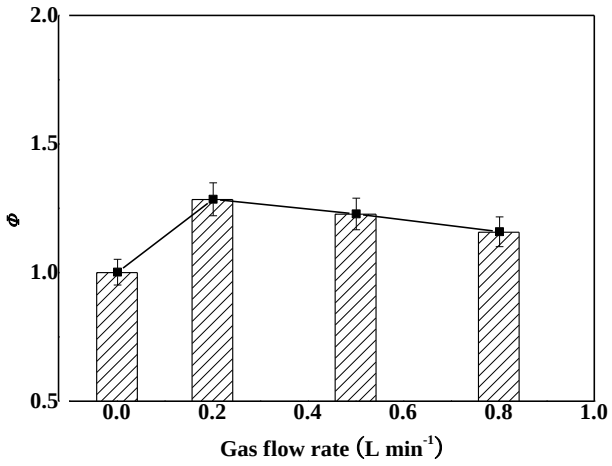

Fig. 4.2 The flux enhancement ratio Φ at varied gas flow rate (Set A experiments, Q_f = 0.41 L min^{-1}, Q_p = 0.15 L min^{-1}, T_f = 330 K, T_p = 299 K)

4.4.1.2 Characterization of bubble properties *vs.* MD performance

To study the working mechanisms induced by bubbling in DCMD, bubble images were captured during experiments to analyze the bubble frequency in every sufficiently small size domain and size distribution curves in Origin (Eq. (4.18)). Figs. 4.4 a, b & c show the captured bubble images at various gas flowrates based on Set A experiments, with the corresponding histograms of bubble size distribution displayed in Figs. 4.4 d, e & f, respectively. In general, the images in Fig. 4.4 a, b & c qualitatively illustrate that the larger bubbles with more uneven diameters are formed at a higher gas flowrate. Accordingly, the distribution curves obtained from bubble size analysis in Figs. 4.4 d, e & f show that the bubble size distribution tends to be more spread out with increasing gas flowrate, *i.e.*, the size deviation from the mean value increases and the percentage of number of large bubblers increases as the curve flattens along the *x* direction (bubble size). According to the relationship between the bubbling frequency and bubble size given in Eq. (4.18), the mean bubble size and variance of size distribution curves at different gas flowrates were derived and presented in Fig. 4.5. The results show that the mean bubble size increases steadily from 2.80 mm to 3.81 mm and the corresponding variance increases dramatically from 0.28 to 1.80 with increasing gas flowrate from 0.2 L min^{-1} to 0.8 L min^{-1}, which

have quantitatively confirmed the information obtained from the bubble images illustrated in Fig. 4.4. Combined with the MD performance results shown in Fig. 4.3, it is clear that a narrow bubble size distribution with a smaller mean size at a lower gas flow rate has helped to achieve a higher permeation flux, due to more effective local mixing and surface renewal of the liquid boundary layers. Thus, a careful choice of gas flowrate has to be made to avoid large bubbles or slugs that compromise module performance, not to mention the unnecessary energy consumption of aeration and potential fiber breakage and/or membrane wetting problems during long-term operation.

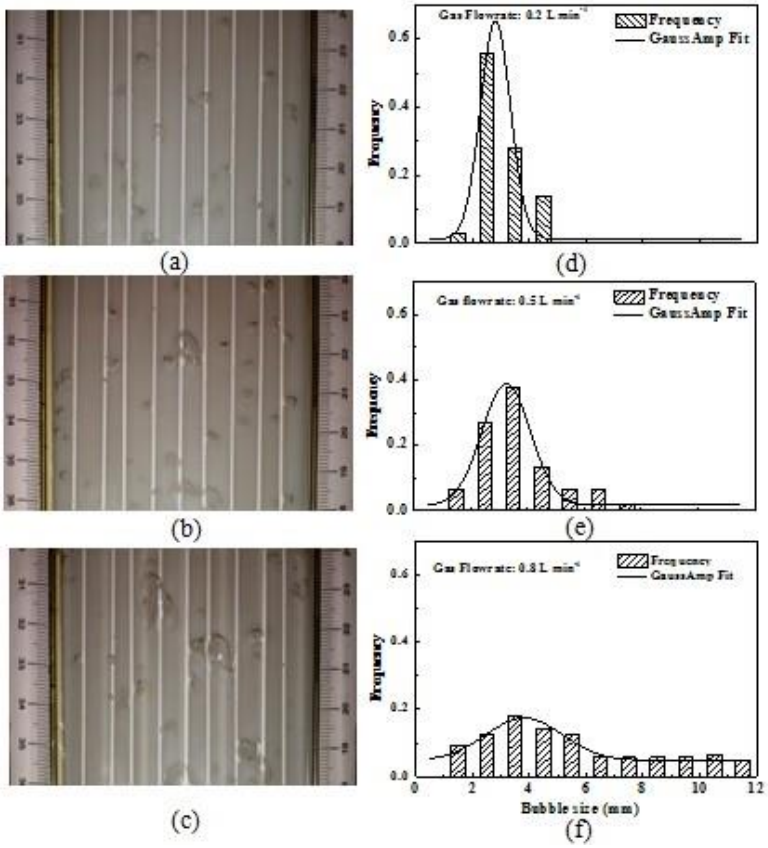

Fig. 4.3 Bubble images and bubble size distribution at varied gas flowrates: (a)&(d) 0.2 L min^{-1}; (b)&(e) 0.5 L min^{-1}; (c)&(f) 0.8 L min^{-1}. (Set A experiments, Gas sparger: six 1-mm gas inlets)

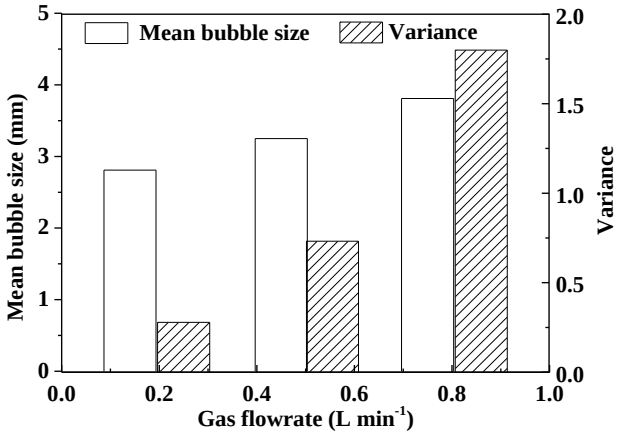

Fig. 4.4 Mean bubble size and variance of bubble size distribution curves at different gas flowrates (Set A experiments, Gas sparger: six 1-mm gas inlets)

4.4.1.3 Heat-transfer assessment with and without gas bubbling in MD (pure water test)

The Set B experiments were conducted to investigate the intensification mechanisms of heat transfer in bubbling-assisted DCMD. Based on Eq. (4.7), experimental data was analyzed and plotted following the linear relationship of $\Delta T / J\gamma_{vap}$ and $1/(dp/dT)$, as shown in Fig. 4.6, which shows the comparison between the original (Fig. 4.6 a) and bubbling-assisted DCMD systems (Figs. 4.6 b-d, with gas flow rates of 0.2, 0.5 and 0.8 L min^{-1}, respectively). The linearity of the data with a correlation coefficient R^2 > 0.99 further confirms the accuracy of applying Eq. (4.7) for the selected temperature range (T_f–T_p<10 K). Therefore, the film heat transfer coefficient h and overall mass transfer coefficient C were calculated based on the intercept and slope of the linear regression equation. Compared to a non-bubbling system, Figs. 4.6 b & d show that the heat transfer coefficients were found to increase by 130%, 102% and 53% for gas flow rates of 0.2, 0.5 and 0.8 L min^{-1}, respectively. Obviously, the enhancement ratio decreases with increasing gas flow rate, which can be well-associated with the MD flux results and bubble size distribution curves discussed in Sections 4.4.1.1 and 4.4.1.2.

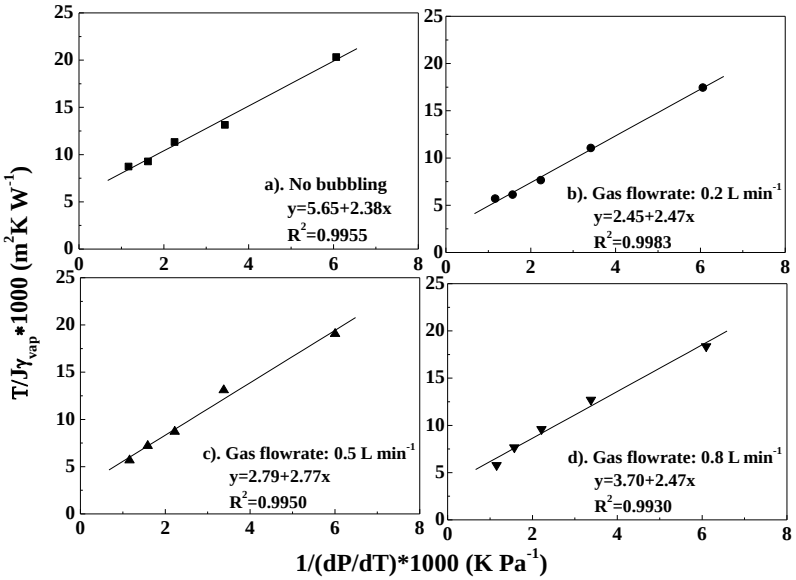

Fig. 4.5 Relationship between $\Delta T/J\gamma_{vap}$ *vs. 1/(dP/dT)* in DCMD at varied gas flow rate (Set B experiments, Q_f = 0.41 L min^{-1}, Q_p = 0.15 L min^{-1}, T_m = 296 ~ 333 K)

Also, based on the heat transfer coefficients obtained from Fig. 4.6, the corresponding temperature polarization coefficient (*TPC*) and the ratio of conductive heat loss to overall heat flux (q_c/q) were calculated at varied gas flowrates. The respective results are given as the functions of membrane temperature T_m in Figs. 4.7 & 4.8. In Fig. 4.7 it is observed that the *TPC* values decrease generally with increasing membrane temperature T_m (296 ~ 333 K) for a DCMD system with or without bubbling. This is because with the bulk temperature conditions kept constant (T_f, T_p), a higher evaporation rate is caused by a higher membrane wall temperature at the feed side, T_{fm}, and subsequently leads to a higher condensation rate and a more rapid increase of the wall temperature at the permeate, T_{pm}. As a result, a lower trans-membrane temperature difference (T_{fm} - T_{pm}) and hence a smaller *TPC* occur at a higher membrane temperature T_m (Eq. (4.5)). Nevertheless, compared to the non-bubbling DCMD system, the introduction of gas bubbling obviously showed a significant improvement on the temperature polarization coefficient *TPC* and DCMD driving force (T_{fm} - T_{pm}) at a given membrane temperature T_m. Consistent with the heat transfer coefficients obtained from Fig. 4.6, the *TPC* curves in Fig. 4.7 decreases with increasing gas flowrate when gas bubbles are introduced – the highest *TPC*

enhancement ratio of 113% (over the non-bubbling DCMD system) is achieved at a lower gas rate of 0.2 L min^{-1} and membrane temperature of 333 K. It has again confirmed that a gas stream with fine bubbles and narrow bubble size distribution can greatly intensify the heat-transfer process and facilitate the mitigation of temperature polarization effect.

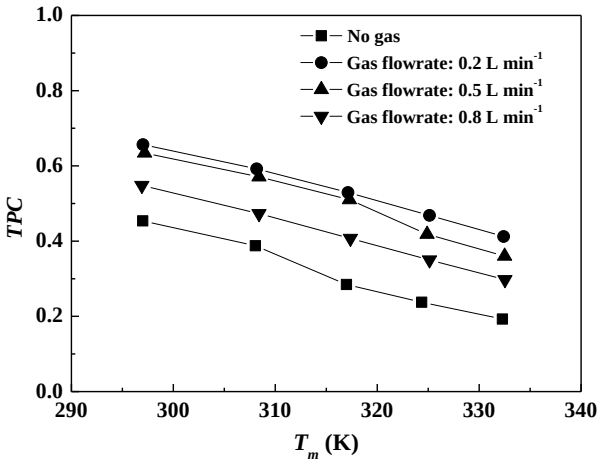

Fig. 4.6 Comparison of temperature polarization coefficient (*TPC*) in DCMD at varied gas flow rate (Set B experiments, Q_f = 0.41 L min^{-1}, Q_p = 0.15 L min^{-1}, T_m = 296 ~ 333 K)

Similarly, in Fig. 4.8 the ratio of conductive heat loss to total heat flux, q_c/q, also decreases with increasing membrane temperature at a constant q, regardless of the gas rate. The main reason is that the q_c increases linearly with the trans-membrane membrane temperature difference (T_{fm} - T_{pm}); while the q_v has an exponentially relationship with (T_{fm} - T_{pm}), as indicated in (Eq. (4.3)). Clearly, the non-bubbling DCMD presents a lower ratio of q_c/q (from 24.36% at T_m = 297 K to 5.55% at T_m = 332 K) than any bubbling-assisted systems. This can be explained by the lower *TPC* and hence a smaller trans-membrane temperature difference (T_{fm} - T_{pm}) (*i.e.*, driving force) caused by the poorer mixing and flow dynamics on the feed side under non-bubbling system. On the contrary, with enhanced hydrodynamics and reduced liquid boundary layers under bubbling conditions, a dramatic increase of the driving force (T_{fm} - T_{pm}) and higher permeation flux is the penalty for a subsequent rise of the conductive heat q_c. Therefore, a compromise has to be made for MD system design

based on this trade-off relationship between permeation flux and conductive heat loss.

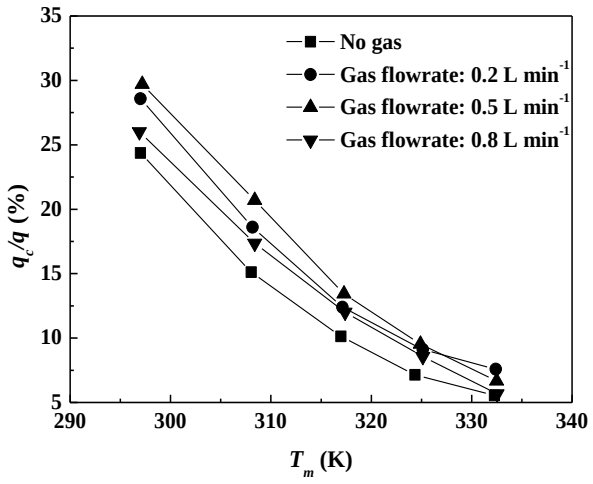

Fig. 4.7 Comparison of conductive heat loss in DCMD at varied gas flow rate (Set B experiments, Q_f = 0.41 L min^{-1}, Q_p = 0.15 L min^{-1}, T_m = 296 ~ 333 K)

4.4.2 Quantification of scaling resistance in DCMD with and without bubbling

With the encouraging results of flux enhancement achieved (Section 4.4.1) in two-phase flow MD systems, further investigations are conducted to evaluate its effectiveness in scaling control in treating highly concentrated feeds.

4.4.2.1 Flux decline *vs.* scaling growth in non bubbling MD

To explore the relationship of permeation flux decline and growth of scaling layer on the membrane surface, Set C experiments were carried out for high concentration batch-mode DCMD without incorporating bubbling. The results are shown in Fig. 4.9 in terms of the relative permeation flux ($J_{w/o|t=t1}/J_{w/o|t=0}$) (*i.e.*, the ratio of instantaneous trans-membrane flux to the initial flux value at t=0) and the ratio of scaling resistance to the overall resistance (r_{sl}/r_{ov}) along the operating time. Clearly, a drastic flux decline of 65% is observed after 3.5-hour operation under supersaturation conditions of the concentration process. This is mainly due to the continuous NaCl crystal deposition on the membrane surface and hence rapid growth of scaling layer

with time, which is consistent with the previous research findings (Chan, Fane et al. 2005; Edwie and Chung 2012; Chen, Yang et al. 2013; Chen, Lu et al. 2014).

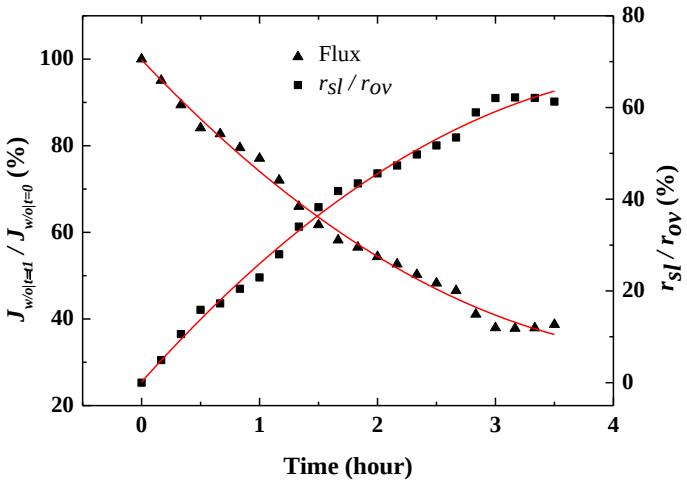

Fig. 4.8 Relative permeation flux ($J_{w/o|t=t1}/J_{w/o|t=0}$) and scaling resistance (r_{sl}/r_{ov}) as functions of operation time in non-bubbling DCMD (Set C experiments, Q_f = 0.41 L min^{-1}, Q_p = 0.28 L min^{-1}, T_f = 334 K, T_p = 294 K)

To ascertain the relationship of flux decline and scaling formation, the ratio of scaling resistance to overall resistance (r_{sl}/r_{ov}) (Eqs. (4.12) and (4.14)) was calculated and also plotted against operation time t in Fig. 4.9. Obviously, the curve of (r_{sl}/r_{ov}) shows an increasing trend: at t = 0, the scaling resistance r_{sl} is close to zero because of the insignificant initial deposition of fine crystals on the membrane surface; as t increases and more pure water is extracted from the feed, the ratio (r_{sl}/r_{ov}) increases rapidly due to the constant rise of supersaturation level (driving force for crystallization) and subsequent accumulation of more and larger crystals on the membrane surface, which inevitably leads to severe membrane pore blockage and declined permeation flux (Fig. 4.9). Eventually, the resistance of scaling r_{sl}/r_{ov} reaches 65% at t=3.5 h and has clearly become the dominant factor for major flux drop and deterioration of heat and mass transfers in MD.

To associate the results presented in Fig. 4.9 with the tendency of crystal deposition and/or scaling formation on the membrane surface, post-experiment membrane inspection was conducted at different operation times. The SEM imaging results are

shown in Fig. 4.10. At t = 0 h, no crystal deposition is observed on the membrane surface, as shown in Fig. 4.10(a); while at t = 1.5 h a small amount of fine crystals appear on the surface (Fig. 4.10(b)). Later on, a substantial crystal coverage is found at t = 3.5 h (Fig. 4.10(c)). Therefore, consistent with the tendency of flux decline along the operation time (Fig. 4.9), the physical observation of gradual crystal deposition on the membrane surface has confirmed the increasing proportion of scaling resistance (*i.e.*, r_{sl}/r_{ov}) in high concentration DCMD.

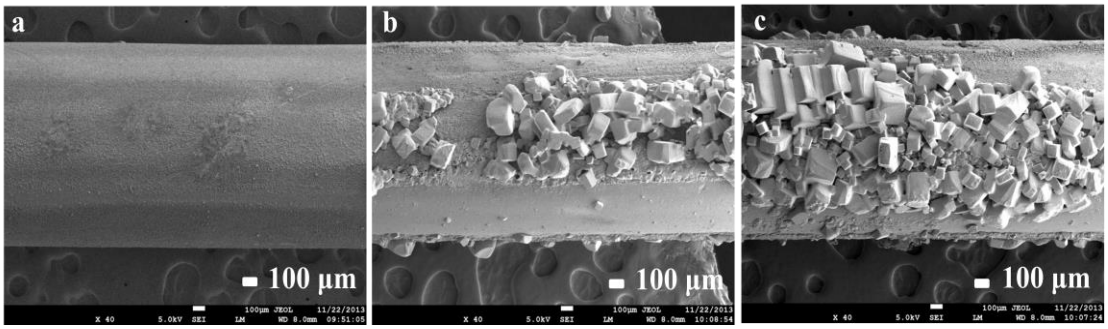

Fig. 4.9 SEM images (magnification factor: 40 ×) of membrane surface in batch-mode DCMD at different operation times of (a), t=0; (b) t=1.5-hour and (c) t=3.5-hour

4.4.2.2 Flux enhancement *vs.* scaling mitigation in bubbling-assisted MD

To reveal the fundamentals of process enhancement and scaling mitigation by incorporating gas bubbling into MD, Set C experiments including four contrast tests for high concentration batch-mode DCMD were carried out at varied gas flowrates with other operating conditions held constant. With the non-bubbling system as benchmark (*i.e.*, gas flowrate=0), the scaling resistance in high concentration DCMD with bubbling was quantified based on Eq. (4.17). The scaling-resistance curve as a function of operating time for each gas flowrate is plotted in Fig. 4.11. Similarly to the discussions for Fig. 4.9, a general increasing trend of the scaling resistance curve is observed at a given gas flowrate. Overall, compared with the non-bubbling MD system, the scaling resistance curves at gas flowrates of 0.2 & 0.5 L min^{-1} are significantly lower with the introduction of two-phase flow. However, a further increase of gas flowrate to 0.8 L min^{-1} has an unexpected influence on the scaling resistance compared to the benchmark – an initial reduction and a subsequent

dramatic increase as the solution saturation level elevates. The main reason is that in the initial stage of crystal formation, the introduction of bubble flow can effectively enhance the surface shear intensity and prevent crystal deposition on the membrane surface; while at high gas flowrate (*e.g.*, at 0.8 L min^{-1} with mean bubble size of 3.81 mm and variance of 1.80, Fig. 4.5), the introduction of large and uneven bubbles or slugs would instead lead to severe flow channelling and rapid decrease on the volume of the feed solution fed into the module, which has further accelerated the nucleation of new crystals and growth of existing particles adjacent to membrane surface. Subsequently, more severe scaling phenomenon was observed. As previously discussed in Section 4.4.1, a high gas flowrate is not necessarily cost-effective and could even cause an adverse effect on the module performance and scaling issue in MD.

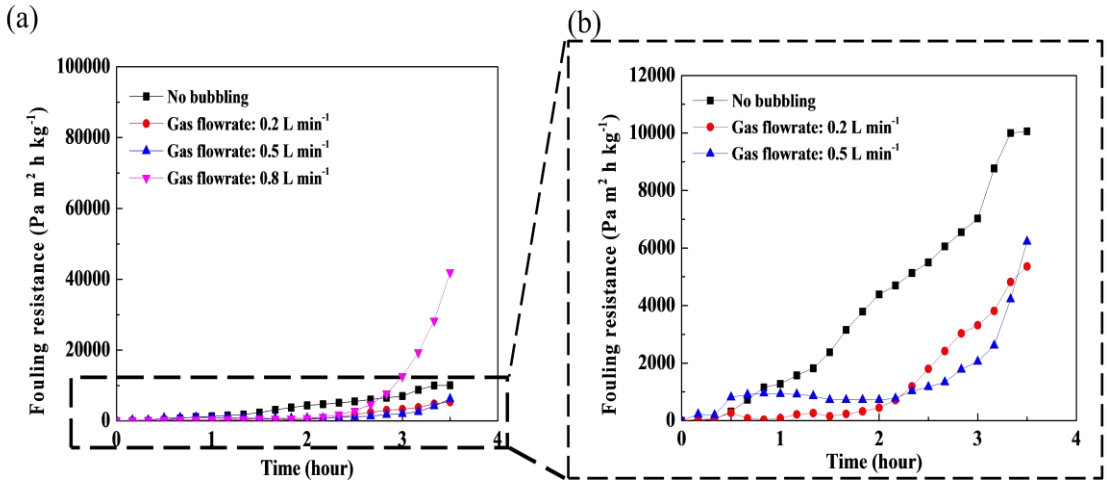

Fig. 4.10 Comparison of scaling resistance growth at varied gas flowrates in high concentration DCMD (Set C experiments, Q_f = 0.41 L min^{-1}, Q_p = 0.28 L min^{-1}, T_f = 334 K, T_p = 294 K)

To further analyze the effectiveness of fine and uniform bubbles under deliberately-selected gas flowrate of 0.2 & 0.5 L min^{-1}, a magnified local snapshot is given in Fig. 4.11 for a clear display of their scaling resistance curves benchmarked against that of the non-bubbling MD system with saturated feed solution. As stated previously, it is observed that scaling resistance has been significantly reduced with the injection of gas bubbles, which may induce secondary flows and physically displace the

concentration layer adjacent to membrane surface. In general, compared to steadily increasing trend of the non-bubbling curve, the resistance curves with bubbling initially show an insignificant increase (*i.e.*, 0~2 hour, Fig. 4.11) and then a relatively rapid rise after certain operation time (*i.e.*, > 2 hour, Fig. 4.11). The possible reason is: as initial nucleation occurs with the increasing solution saturation level, the enhanced shear stress on the membrane surface induced by the two-phase flow is expected to partially remove small crystals from the nascent scaling layer. This observation is consistent with our previous research findings (Chen, Yang et al. 2013), which have confirmed that the critical point of major permeation flux decline associated with scaling formation could be significantly delayed with the introduction of two-phase flow into high concentration MD. Yet, a continuously increasing supersaturation level and more rapid nucleation rate in batch-mode MD would inevitably lead to a deterioration of crystal aggregation and deposition on the membrane surface.

A further comparison is made to evaluate the operability of gas-bubbling DCMD system beyond supersaturation in terms of its capacity to remove water and reduce discharge in a given operation time, defined as water product, W, g m^{-2}. The values of W can be obtained via dividing the weight of water removed in the range of given time by the membrane area used in the batch mode DCMD. The results are displayed via a bar chart in Fig. 4.12 for various gas flowrates. Compared to the non-bubbling MD system, the introduction of bubbling exhibits great potential in maximizing the water removal from supersaturated brines– the highest enhancement ratio of 2.3-fold at gas flowrate of 0.5 L min^{-1}, followed by 2- and 1.83-fold at 0.2 and 0.8 L min^{-1}, respectively. Clearly, appropriately chosen bubbling conditions can help achieve maximum anti-scaling effect and postpone the water flux decline in MD brine concentration.

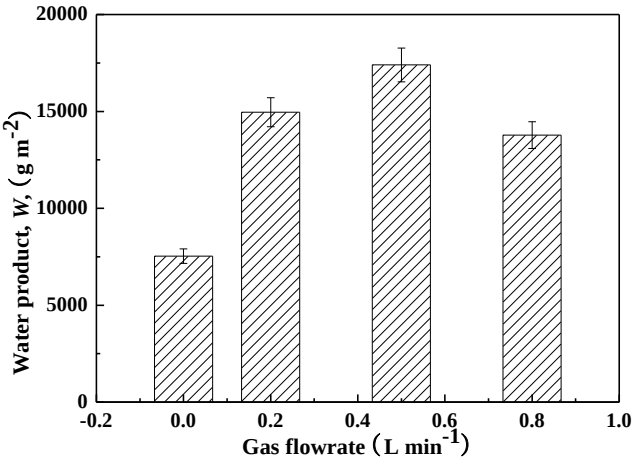

Fig. 4.11 Comparison of total water removal from concentrated salt solutions in DCMD at varied gas flow rate (Set C experiments, Q_f = 0.41 L min^{-1}, Q_p = 0.28 L min^{-1}, T_f = 334 K, T_p = 294 K)

4.5 Summary

This chapter has explored the intensification mechanisms of gas bubbling for heat transfer enhancement and scaling alleviation in MD brine processing. Relatively small bubble size and narrow size distribution are preferred to attain even flow distribution and enhanced surface shear intensity. The highest heat-transfer coefficients were obtained with fine bubbles at optimized bubbling conditions. Correspondingly, the temperature polarization effect was greatly mitigated with the penalty of an unavoidable higher conductive heat loss to the membrane matrix. The trade-off relationship suggested that a compromise has to be made to accomplish a desired MD thermal efficiency.

Besides heat transfer resistance, fouling/scaling is another significant roadblock to the widen adoption of membrane distillation technology, especially for high concentration operation. In the MD brine concentration experiment without bubbling, the rapid decline of the measured relative flux ($J_{w/o|t=t1} / J_{w/o|t=0}$) accorded with the increasing contribution of the scaling resistance to the overall mass transfer resistance (r_{sl} / r_{ov}), implying that the resistance of scaling has become the controlling factor for permeation flux drop. In comparison, the introduction of gas bubbling into MD could

significantly reduce the scaling resistance, due to the high shear stress induced by gas bubbles and the removal of tiny deposited crystals from the membrane surface. However, an unreasonably high gas flow rate has the adverse effect due to the formation of large and uneven bubbles or slugs resulting in local by-passing and increased frequency of crystal collision.

In a word, to effectively control scaling formation for a more operable MD brine concentration process (especially beyond supersaturation level), optimized aeration conditions with a smaller mean bubble size and narrower bubble size distribution are preferred. Nevertheless, the incorporation of supplementary membrane cleaning techniques is still necessary for effectively restoring the membrane performance as the scaling layer matures.

CHAPTER 5

QUANTITATIVE STUDY ON CRYSTALLIZATION INDUCED SCALING IN HIGH CONCENTRATION DIRECT CONTACT MEMBRANE DISTILLATION (DCMD)

5.1 Introduction

As mentioned previously, mainly initiated by the concentration and temperature polarization effects (Schofield, Fane et al. 1987), potential salts precipitation/scaling (inorganic fouling) on the membrane surface could lead to major flux decline and eventually shortened membrane lifespan. Being recognized as a complex phenomenon, membrane fouling/scaling has been studied using various direct observation methods in different membrane applications (Li, Fane et al. 2003; Chen, Li et al. 2004; Hughes, Tirlapur et al. 2006; Uchymiak, Rahardianto et al. 2007), as summarized in Section 2.4. It is worth mentioning that a new indirect observation technique, which has incorporated ultrasonic devices, was proven to be useful in detecting the onset of inorganic scaling and colloidal fouling on the membrane surface for RO and NF studies (Mairal, Greenberg et al. 1999; Mairal, Greenberg et al. 2000; Cobry, Yuan et al. 2011; Lu, Kujundzic et al. 2012; Mizrahi, Wong et al. 2012; Sim, Chong et al. 2012). Nevertheless, costly equipment and complex operation procedures have restricted these techniques to merely lab-scale studies.

Fundamentally, to prolong membrane lifespan and mitigate scaling formation, it is crucial to predict the critical point of major flux decline in high concentration MD operation. However, to date no method has been reported for in-situ scaling

monitoring. There is a lack of clear definition and qualitative prediction for the critical point in the scaling process, which is mainly due to the complex temperature\concentration polarization phenomena (Schofield, Fane et al. 1987) and ion activity coefficient (Pazuki and Rohani 2006) near the membrane surface in MD process. Based on the literature review in Section 2.4.5 and 2.5, the development of crystal deposits can be quantified via the crystallization kinetics. Additionally, Gryta (Gryta 2008) reported that the dramatic flux decline was mainly caused by salt crystals formation and subsequent deposition on the membrane surface. Hence, in the process of combined MD mass/heat transfer and crystal growth, a good understanding on crystallization kinetics (Nývlt 1968; Tavare and Garside 1986; Qiu and Rasmuson 1991; Tavare 1991; Dash and Rohani 1993; Tavare 1993; Söhnel, Bravi et al. 1996) on the membrane surface is essential for a timely prediction of the critical point and scaling control in high concentration MD process.

In this chapter, a new method was proposed based on the crystallization kinetics to quantify scaling formation and predict critical point in high concentration MD process. Sodium chloride (NaCl) was adopted as a model crystal species to study the crystal nuclei growth and scaling process in polyvinylidene fluoride (PVDF) hollow fiber DCMD modules, both experimentally and numerically. In experiments, the crystal size distribution (CSD) was analyzed for the crystals deposited on the membrane surface when the feed solution exceeded its supersaturation point. Thus, the crystallization kinetics of sodium chloride nucleation and growth on the membrane surface were derived. Combined with the derived kinetic expressions and MD transport equations, a new modelling approach namely crystallization on membrane surface (COMS) was proposed to quantify the status of crystal deposition along the operating time and to identify the critical point of major flux decline. By defining a critical crystal size, the corresponding critical point was able to be predicted effectively under different operation conditions.

5.2 Theory

5.2.1 Crystallization kinetics

5.2.1.1 Population balance equation

In the crystallization process the population balance theory was widely recognized as an effective method to model the crystal nucleation and growth (Hulburt and Katz 1964). It is established as a basic theoretical framework for various particulate development processes, based on the mass balance to account for the number of crystals formed during crystallization (Randolph and Maurice 1988). The output of this theory is expressed as a number distribution of crystals across both time (t) and size (l) domains (Randolph and Maurice 1988):

$$\frac{\partial n(l,t)}{\partial t} = -G\frac{\partial n(l,t)}{\partial L} + B' \tag{5.1}$$

where n denotes the population density of crystals, No. m^{-4}. The term on the left-hand side describes the accumulation of crystal numbers in a size range from l_i to l_{i+1} in a time interval of Δt. The first term on the right-hand side represents the net mass of particles increased through the same size range by a crystal growth rate of G (m s^{-1}); while the second term B' gives the overall crystal birth rate associated with nucleation growth by supersaturation and simultaneous crystal death by dissolution in the same size range of l_i to l_{i+1}, No. $m^{-4}s^{-1}$ (Abbas and Romagnoli 2007).

5.2.1.2 Kinetic expressions for nucleation and growth rate

Crystal nucleation and growth are two predominant and competing phenomena in a crystallization process, in which the former mechanism involves the formation of new crystal nuclei while the latter is due to the transformation/growth of existing small particles into big crystals through solutes deposition from the supersaturated solution (Costa, da Costa et al. 2005). To investigate this simultaneous process, in the current study a power law model is employed to simply express the crystal nucleation rate B and growth rate G:

$$G = K_G(c_{fm} - c^*)^g \tag{5.2}$$

$$B = K_B G^b \tag{5.3}$$

where the kinetic rate constant for crystal growth K_G (kg^{-g} m^{3g+1} s^{-1}), nucleation rate constant K_B (No. m^{-3-b} s^{-1+b}), exponents g and b can be obtained from experimental data regression. The c_{fm} and c^* are the salt concentrations adjacent to the membrane surface and the equilibrium saturated concentration at membrane wall temperature T_{fm}, respectively, kg m^{-3} or wt %. The difference between c_{fm} and c^* is mainly due to the temperature polarization (TP) and concentration polarization (CP) effects in MD, where T_{fm} is lower than that of the bulk solution and c_{fm} is higher than that of the bulk. Therefore, the difference of c_{fm} and c^* is the driving force for the crystallization process.

Generally, the crystal growth rate can be described as the size variation from size l (m) at time t to size (l+Δl) at time (t+Δt). The average crystal growth rate, G, over a given time interval, Δt (s), can be calculated through a linear relationship (Söhnel, Bravi et al. 1996; Kubota, Otosaka et al. 2000):

$$G(l,t) = \Delta l / \Delta t \tag{5.4}$$

Therefore, the experimental G values can be obtained at different time intervals according to Eq. (5.4). Additionally, Eq. (5.2) is transformed into its logarithmic form:

$$\log G = \log K_G + g \times \log(c_{fm} - c^*) \tag{5.5}$$

With the experimental G values and concentration difference (c_{fm} - c^*) the crystal growth rate constant K_G and the exponent g can be derived through a linear regression based on Eq. (5.5).

Similarly, the average crystal nucleation rate, B, can be expressed as the total crystal number changed ΔN_c over the same time interval Δt:

$$B(l,t) = \Delta N_c / \Delta t \tag{5.6}$$

With the experimental B values obtained from Eq. (5.6) at different time intervals, the crystal kinetic nucleation constant K_B and the exponent b in Eq. (5.3) can be derived. The derivation of the crystallization kinetic constants and the specific

expressions of the crystal growth and nucleation rates will be further discussed in Section 5.4.2.1.

5.2.1.3 Numerical solutions for population balance equation

Since the population balance equation is a partial differential equation in both time and size domains (Eq. (5.1)), which precludes obtaining a precise analytical solution, a method named discretised population balance is adopted in this study to correlate the crystal growth function in a given size domain. It can convert the population balance equation into a series of linear ordinary differential equations along the size domain l (Abbas and Romagnoli 2007):

$$\begin{cases} \dfrac{dN_{c\_1}}{dt} = -\dfrac{G}{2\phi_1} N_{c\_1} + B_1 \\ \dfrac{dN_{c\_i}}{dt} = -\dfrac{G}{2\phi_i} N_{c\_i} + \dfrac{G}{2\phi_{i-1}} N_{c\_i-1}, \; i=2,3,\ldots,\; n\text{-}1 \\ \dfrac{dN_{c\_n}}{dt} = -\dfrac{G}{2\phi_n} N_{c\_n} + \dfrac{G}{2\phi_{n-1}} N_{c\_n-1} \end{cases} \tag{5.7}$$

where N_{c_i} is the number of crystals in the size range of (l_i, l_{i-1}), defined as $N_{c\_i} = \int_{l_{i-1}}^{l_i} n_i(l,t)dl$ (Costa, da Costa et al. 2005). The discretisation of size domain indicates that a fixed crystal size difference ϕ_i ($\phi_i = l_i - l_{i-1}$) is used in this study; while the time interval Δt (s) varies accordingly. Overall, this set of linear ordinary differential equations (Eq. (5.7)) can be solved using the conventional Runga-Kutta Algorithm (Butcher 2008).

5.2.2 Mathematical model development in high concentration DCMD

To gain a better understanding on the effect of scaling behaviour on the process performance in batch mode high concentration DCMD, a combined mathematical model named crystallization on membrane surface (COMS) was established based on the relationship between the MD transport mechanisms and crystallization kinetics.

In the COMS model, a hollow fiber is axially divided into *I* pieces of microelements along the length (Fig. 5.1(a)). In a sufficiently thin element E_i (Fig. 5.1(b)), Q_{f_i} and Q_{f_i+1} represent the inlet and outlet flow rates of the feed; while Q_{f_i+1} and Q_{p_i} are the inlet and outlet flow rates of the permeate, respectively. The local average temperature of the influent and effluent in each element is considered as local temperature T_{f_i} and T_{p_i}, based on which the MD mass and heat flux can be determined. It is worth mentioning that in the COMS model the MD related parameters were determined based on the mass- and heat-transfer analyses in prior MD studies (Schofield, Fane et al. 1990; Yang, Wang et al. 2011; Yu, Yang et al. 2011; Guan, Wang et al. 2012; Yang, Yu et al. 2012; Yang, Yu et al. 2012; Yu, Yang et al. 2012; Chen, Yang et al. 2013). A summary of key MD equations (*i.e.*, Eqs. (5.8) – (5.18)) included in this study is given in Table 5.1. For the crystallization part in the COMS model, the kinetic constants (K_G, K_B, g and b) of sodium chloride nucleation and growth expressions (Eqs. (5.2) & (5.3)) were derived from experimental CSD results on the membrane surface in high concentration DCMD.

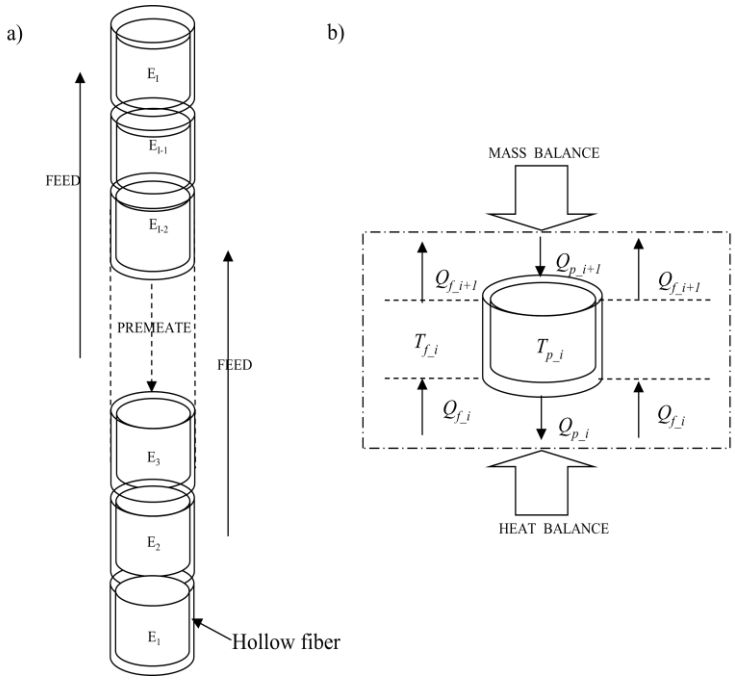

Fig. 5.1 Flow diagram of membrane element in modeling membrane distillation process

Table 5.1 Summary of key equations of heat and mass balance for membrane element and transfer process in DCMD

Mass balance for an element of membrane	$Q_{f\_i} - Q_{f\_i+1} = Q_{p\_i} - Q_{p\_i+1} = JA\Delta t$	(5.8)
Heat balance for an element of membrane	$q = q_v + q_c = Q_{f\_i} C_{p\_f} (T_{f\_i} - T_{f\_i+1}) = Q_{p\_i} C_{p\_p} (T_{p\_i} - T_{p\_i+1})$	(5.9)
Temperature and flowrate calculation for every membrane element	$T_{f\_i} = T_{f\_i+1} - \frac{q_v + q_c}{Q_{f\_i} C_{p\_f}}$; $T_{p\_i} = T_{p\_i+1} + \frac{q_v + q_c}{Q_{p\_i} C_{p\_p}}$	(5.10)
	$Q_{f\_i} = Q_{f\_i+1} - JA\Delta t$; $Q_{p\_i} = Q_{p\_i+1} + JA\Delta t$	(5.11)
Heat transfer coefficient	$h_f = \frac{Nu_{\_f} \times k_{\_f}}{d_{h\_f}}$; $h_p = \frac{Nu_{\_p} \times k_{\_p}}{d_{h\_p}}$	(5.12)
	$h_m = k_m / \delta_m$	(5.13)
	$T_{fm} = T_f - (T_f - T_p) \frac{1/h_f \times d_i / d_o}{1/h_f \times d_i / d_o + 1/(h_m + h_v) + 1/h_p}$	(5.14)
Temperature at membrane surface and *TPC*	$T_{pm} = T_p - (T_f - T_p) \frac{1/h_p}{1/h_f \times d_i / d_o + 1/(h_m + h_v) + 1/h_p}$	(5.15)
	$TPC = \frac{T_{fm} - T_{pm}}{T_f - T_p}$	(5.16)
Concentration at membrane surface and *CPC*	$c_{fm} = c_f \times CPC$	(5.17)
	$CPC = \exp(J / \rho_w k_s)$	(5.18)

During the scaling formation, it can be assumed that the MD permeation flux, *J*, decreases linearly with the percentage of membrane surface covered by crystal deposition (Uchymiak, Lyster et al. 2008). In this study, the values of flux were determined from the measured data experimentally. The accumulated mass of water vapor across the membrane in a given time interval and surface area, m_{flux}, kg, can be calculated as:

$$m_{flux} = \int_{t_0}^{t} JA dt \tag{5.19}$$

Based on the mass balance of the solute, the bulk concentration in feed solution c_f, kg m^{-3} or wt%, varies with operation time and can be obtained as:

$$c_f = \frac{c_0 M_0}{M_0 - m_{flux}} \tag{5.20}$$

where c_0 is the initial feed concentration, kg m^{-3} or wt%, and M_0 is the initial weight of feed solution, kg.

As mentioned in our previous work (Guan, Wang et al. 2012; Yang, Yu et al. 2012; Yu, Yang et al. 2012; Chen, Yang et al. 2013), both concentration polarization (CP) and temperature polarization (TP) play important roles in determining the membrane wall concentration c_{fm} and temperature T_{fm} (its corresponding salt solubility c^*). Thereinto, c_{fm} can be obtained from $(c_f \times CPC)$, in which CPC is the concentration polarization coefficient and correlated with J and the solute mass transfer coefficient k_s (Eq. (5.18)) (Schofield, Fane et al. 1990). T_{fm} can be calculated from bulk temperature and the calculation requires estimation of the four heat transfer coefficients (Eq. (5.14)), h_f and h_p, the heat transfer coefficient of the membrane, h_m, and the vapor heat transfer coefficient, h_v (Schofield, Fane et al. 1990; Guan, Wang et al. 2012; Chen, Yang et al. 2013). Substituting c_{fm} & c^* (corresponding salt solubility at T_{fm}) into Eq. (5.2), the crystal growth G can be rewritten as:

$$G = K_G(c_f \times CPC - c^*)^g \tag{5.21}$$

As a result, the driving force of crystallization, Δc, can be acquired from c_{fm} and c^*, as illustrated in Fig. 5.2, which includes the detailed COMS modelling procedures. The evolution of temperature and concentration were calculated by the discrete membrane element in DCMD. Firstly, with known operating conditions and system specifications as well as experimentally measured permeation flux J, the MD related parameters (membrane wall temperatures T_{fm}, T_{pm}, solution wall concentration at the feed side c_{fm}, temperature polarization coefficient (TPC), and concentration polarization coefficient (CPC)) are obtained. Secondly, the driving force of crystallization Δc can be determined based on c_{fm} and c^* (the salt solubility *at* T_{fm}). When Δc is less than 0, no crystal nucleation and growth occurs in the module; while when the calculated Δc is larger than 0, the regressed expressions of G and B are introduced in the Eq. (5.7) to simulate the process of crystal nucleation and growth using Runga-Kutta Algorithm. With the crystal number N_{c_i} (Eq. (5.7)) of any given size range (l_i, l_{i-1}) derived separately at different operation stage, the total crystal number N across the whole operation can be calculated as:

$$N_c(t) = \sum_{i=1}^{m} N_{c\_i} \qquad (i=1, 2, \ldots\ldots m) \tag{5.22}$$

The mid-point crystal size, newly termed as crystal median size, is identified as a boundary where half of the crystals formed are smaller and the other half are larger. The crystal median size and total number are the final outputs as key parameters to characterize crystal properties. It is worth mentioning that the calculated crystal median size at the corresponding critical point of MD flux dramatic decline is defined as the critical size, which would be further discussed in Section 5.4.2.2.

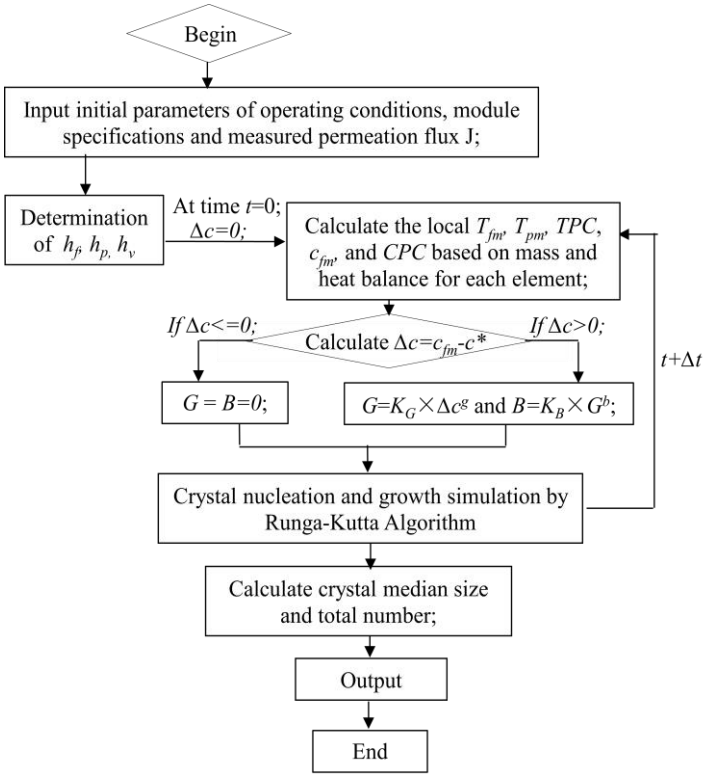

Fig. 5.2 Flow diagram of modelling for crystallization on membrane surface (COMS) in batch high concentration DCMD

Furthermore, to evaluate the accuracy of this COMS model, average absolute relative error (*AARE*) is used as verification criteria:

$$\mathrm{AARE} = \frac{1}{N_{com}} \sum_{1}^{N} \frac{\left|\alpha_{cal} - \alpha_{\exp}\right|}{\alpha_{\exp}} \tag{5.23}$$

where α_{cal} and $\alpha_{\exp}$ represent the simulated results and experimental data (the crystal median size or total number), respectively; N_{com} is the number of experimental points.

5.3 Experimental

5.3.1 Materials and module fabrication

In this chapter similar PVDF membrane (characterized experimentally in Chapter 3) was used to fabricate MD modules. Relevant module specifications are listed in Table 5.2. To study the crystallization process on the membrane surface without the interference from fiber-fiber interaction, four single-fiber MD modules were fabricated by potting the PVDF hollow fiber membranes into Teflon housings with an inner diameter of d_s=4.5 mm and an effective length of 340 mm. The effective membrane area is calculated as 65 cm^2 for flux assessment and scaling observation. More details on module fabrication procedure can be found in the literature (Yang, Wang et al. 2011).

Table 5.2 Parallel module specifications

Parallel module number	Housing diameter, d_s (mm)	No. of fibers in each module	Effective fiber length, L_m (mm)	Membrane area, A (cm^2)
4	4.5	1	340	65

The sodium chloride used to prepare synthetic brine solution was purchased from Merck Pte Ltd with an analytical purity of 99.5%. The HPLC-grade Isopropyl Alcohol (IPA) for crystal analysis was from Fisher Scientific Pte Ltd.

5.3.2 DCMD performance test and crystal analysis

The batch mode (no fresh feed supplement) DCMD experimental set-up with four parallel hollow fiber membrane modules installed is shown in Fig. 5.3. Both the feed and permeate solutions were cycled through the shell and lumen sides of the hollow fiber modules, counter-currently. On the shell side, the feed solution (synthetic brine:

18 wt% sodium chloride (NaCl) solution as an initial concentration) was heated by a water bath in the range of 334~340 K (Polyscience® 9105) and circulated by a peristaltic pump (Masterflex®, Cole Palmer). On the lumen side, the permeate (deionized water) was maintained at 292 K by a cooler (Julabo® F25) and cycled by another peristaltic pump (0.2 L min^{-1}). The bulk temperatures and pressure of both streams were measured by thermocouples connected to the data acquisition system. Flow rates were monitored by in-line digital flow meters. The water flux was measured as weight gain in the permeate reservoir and recorded in every 30 minutes. It is noted that the four membrane modules with the same configuration, as shown in Fig. 5.3(b), were installed in parallel to keep the fluid streams equally distributed.

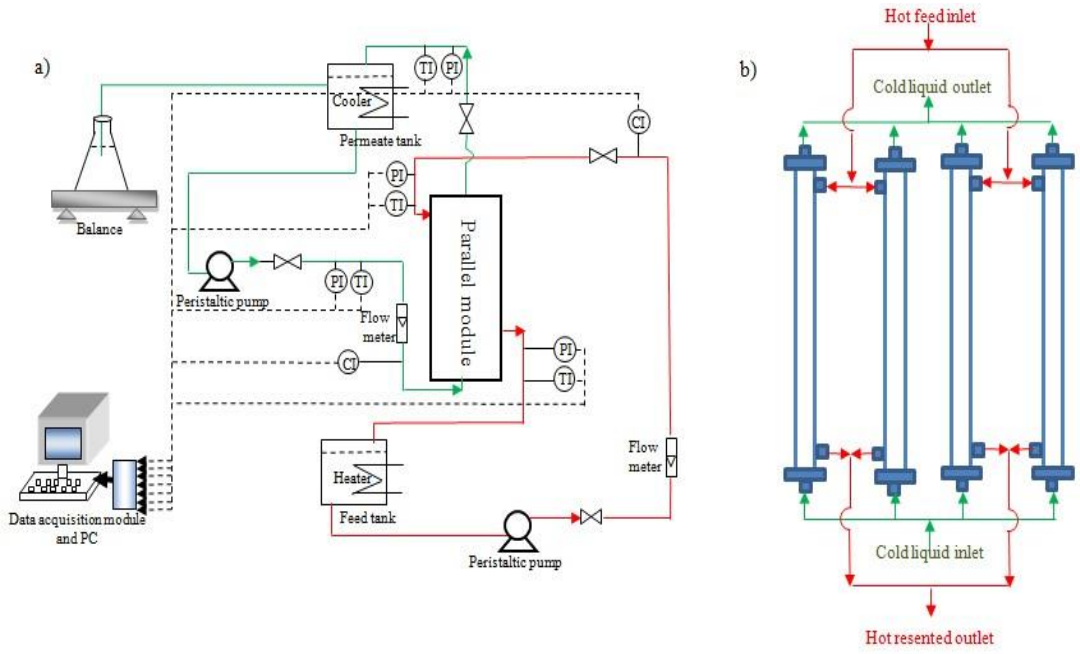

Fig. 5.3 a) Set-up diagram of MD process; b) schematic design of four parallel membrane modules

When the feed solution reached supersaturation, the parallel modules were dismantled separately at different operation time intervals to analyze the crystals depositing on the membrane surface. Cautions must be taken to avoid crystal falling off from the fouled membrane surface when pulled out from the modules. The membrane samples with crystal deposition were immersed immediately in an Isopropyl Alcohol (IPA) solution (liquid dispersion medium), which was then placed

in the ultrasonic cleaner for 20 minutes to peel off the crystals from the membranes. Afterwards, the IPA solution was analyzed using Malvern Mastersizer 2000, to obtain the crystal size distribution (CSD) curves and corresponding median crystal sizes.

In this study, two sets of experiments were carried out: one, named Set #1, for DCMD performance test and derivation of crystallization kinetic constants; Set #2, for the verification of the newly-built COMS models. The operating conditions of Set #1 experiments were: feed flow rate Q_f = 0.8 L min^{-1}; permeate flow rate Q_p = 0.2 L min^{-1}; feed temperature T_f = 340 K; permeate temperature T_p = 292 K; initial mass of salts in feed solution = 1200 g; initial salt concentration of feed solution = 18 wt %. By keeping the same membrane area and flow conditions as Set #1, Set #2 experiments were operated at a varied feed temperature of T_f = 334 K.

5.3.3 Error assessment

All experiments were repeated three times and showed good reproducibility in terms of vapor flux, crystal median size and total crystal number (*AARE* within ±8.5%). The conductivity meter had an accuracy of ±0.1 ms cm^{-1} (feed side) and ±0.1 μs cm^{-1} (permeate side), respectively. The temperature and flow rate variations were strictly controlled within ±0.4 °C and ±0.01 L min^{-1}, respectively.

5.4 Results and Discussion

5.4.1 DCMD flux profile and crystal growth on the membrane surface

The batch mode high concentration DCMD experiments (Set #1) were conducted in the parallel modules, with an initial feed concentration of 18 wt% up to supersaturation level. Fig. 5.4 shows the experimental MD flux and feed concentration as functions of the operation time. The flux profile shows a general decreasing trend along the operation time — a slow initial decrease followed by a dramatic decline. This is because that at the initial stage, an increase of salt concentration at the feed solution resulted in a slight decrease on the vapour pressure

difference across the membrane. Nevertheless, a sharp flux decline occurs when the feed concentration reached a critical level of supersaturation, denoted as critical point A (at 6.60 h), which was evaluated by applying the smoothing spline approach to fit the curve of permeation flux. The point A indicates the first dramatic point of change and a continuous increase of the absolute values of differential coefficients. This is mainly due to the rapid growth of crystal deposition on the membrane surface, which does lead to not only an increase of the resistance to water permeation but also a decrease on the vapour pressure. In the final stage, the flux drops to essentially zero when the membrane surface is completely covered with crystals. Consistently, Fig. 5.5 shows the SEM images of the cross section of the hollow fiber and membrane surface at the initial and final stages without and with depositing crystals, respectively.

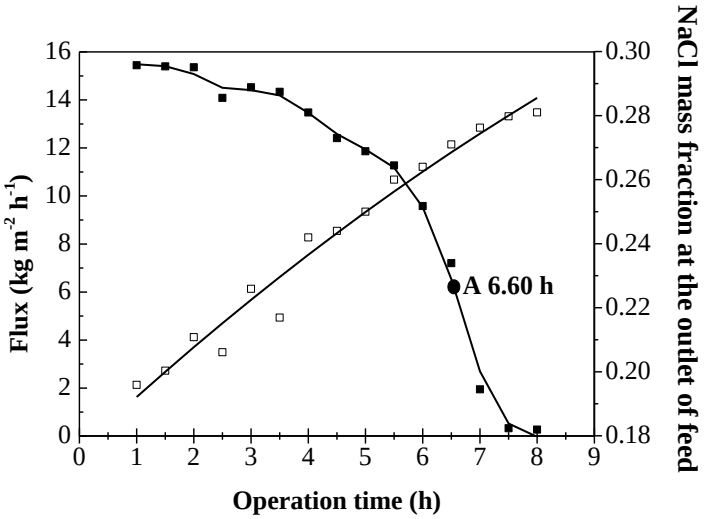

Fig. 5.4 Flux and NaCl mass fraction at outlet of feed side *vs.* time in DCMD experiments Set #1 (Q_f = 0.8 L min^{-1}; Q_p = 0.2 L min^{-1}; T_f = 340 K; T_p = 292 K; initial mass of feed solution: 1200 g; initial salt mass fraction of feed solution: 18%)

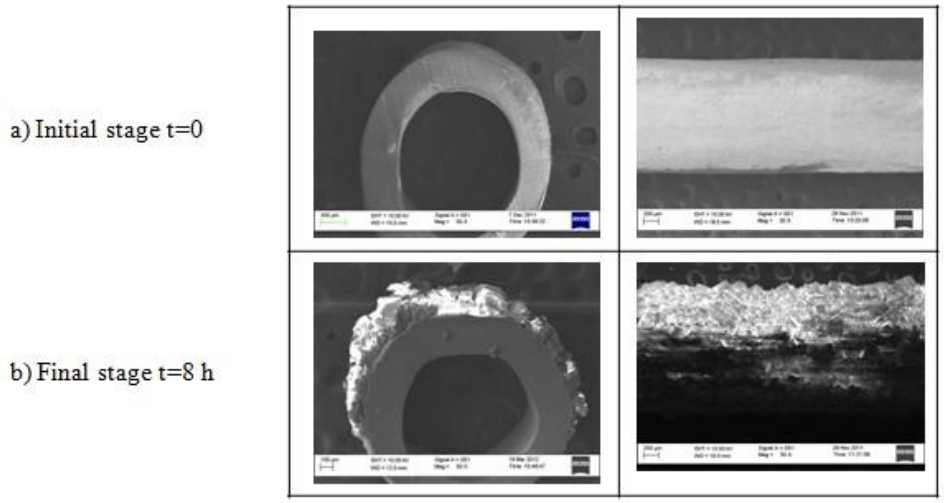

Fig. 5.5 SEM images of cross section and membrane surface at the initial stage (a) and final stage (b) of the DCMD experiments Set #1 (Q_f = 0.8 L min^{-1}; Q_p = 0.2 L min^{-1}; T_f = 340 K; T_p = 292 K; initial mass of feed solution: 1200 g; initial salt mass fraction of feed solution: 18%)

As the crystal deposits are detrimental for the MD system, a good understanding on the crystal properties and growth kinetics on the membrane surface is important. The CSD results shown in Fig. 5.6 were obtained from analyzing crystal samples taken from the membrane surface at different operation times, as indicated in Section 5.3.2. After the feed solution reached supersaturation level, the first sample was taken at t = 6.50 h, followed by the analysis for samples 2 and 3 with 10 min interval. For sample 4 and 5, the sampling interval increased to 30 min. The last sample was obtained at t = 8.00 h. Fig. 5.6 clearly shows that crystal size distribution shifts from left to right along x axis from sample 1 to 5, which indicates an increasing trend of crystal median size with increasing operation time. Surprisingly, the crystal median size of sample 6 dropped to 44.5 μm. This may be due to the detachment of over-sized crystals caused by the low adhesion force to the membrane surface, with continuous particle growth in the supersaturated solution. Therefore, the study of crystallization kinetics on membrane surface was focused on the operation period before the occurrence of crystal detachment (*e.g.*, sample 6 in experiments Set #1).

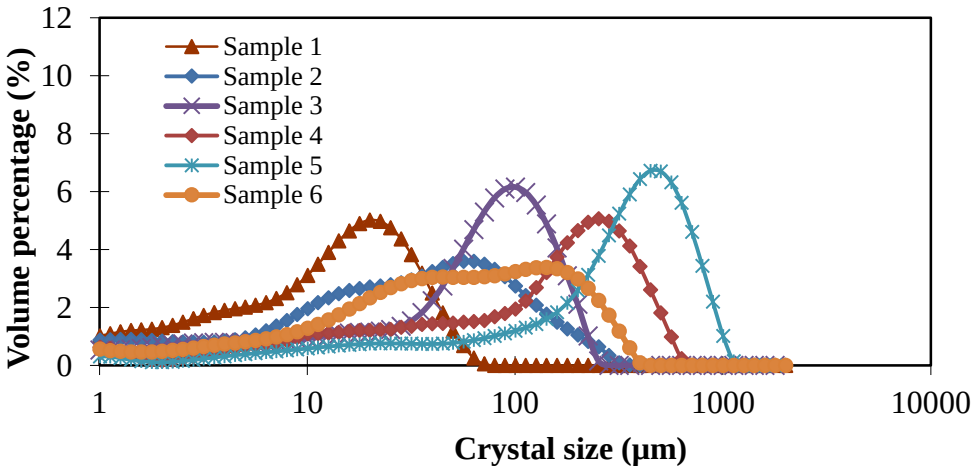

Fig. 5.6 The CSD of the crystals sample on the membrane surface at different time interval of DCMD experiments Set #1 (Q_f = 0.8 L min^{-1}; Q_p = 0.2 L min^{-1}; T_f = 340 K; T_p = 292 K; initial mass of feed solution: 1200 g; initial salt mass fraction of feed solution: 18%)

5.4.2 Investigations of crystallization process on membrane surface

5.4.2.1 Derivation of crystallization kinetic constants

Based on the CSD curves at the operating conditions of experiments Set #1 (Fig. 5.6), the respective crystal median size and total crystal number of samples 1 to 5 were determined and plotted as columns in the operation time range of 6.5 h to 7.5 h, as shown in Fig. 5.7.

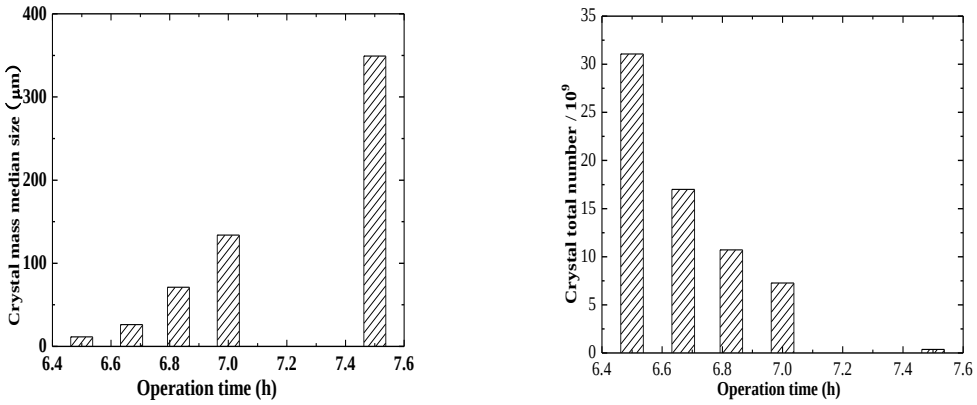

Fig. 5.7 The experimental results of crystal mass median size (a) and total number (b)

with operation time of DCMD experiments Set #1 (Q_f = 0.8 L min^{-1}; Q_p = 0.2 L min^{-1}; T_f = 340 K; T_p = 292 K; initial mass of feed solution: 1200 g; initial salt mass fraction of feed solution: 18%)

In Fig. 5.7(a) it is obvious that the crystal median size increases as the scaling process progresses along the operation time – from 11.39 μm at t=6.5 h to 349.23 μm at t=7.5 h, which correspond to the dramatic flux decline from 9.58 to 1.95 kg m^{-2} h^{-1} at the same operation times, as presented in Fig. 5.4. The increase of the crystal median size in the selected operation range is due to the elevation of supersaturation level of the feed solution with continuously generated water vapor being transported to the permeate side. At the given time interval from 6.50 h to 7.50 h, the experimental average crystal growth rate G can be obtained based on Eq. (5.4) — the crystal growth rate constant K_G and exponent were derived from data regression as 1.0002×10^2 (kg^{-g} m^{3g+1} s^{-1}) and 1.415. Hence, the expression of G in Eq. (5.2) is rewritten as:

$$G = 1.0002\times10^2 \times \Delta c^{1.415} \tag{5.24}$$

At the same sampling times as Fig. 5.7(a), the total number (columns) of crystals depositing on the membrane surface in Fig. 5.7(b) shows a decreasing trend – from 3.1×10^{10} at t=6.50 h to 3.6×10^8 at t=7.50 h. This is probably caused by the Oswald ripening effect (or agglomeration of the fine particles) immediately after the initial nuclei breeding, which is illustrated in Fig. 5.8(a). The Ostwald ripening usually occurs when the particle sizes in a system are significantly different. Gradually, the large crystals (low surface energy) receive spontaneous "nutrient" supply from the small particles (high surface energy) to grow bigger and become more stable on the membrane surface. In a word, the competing mechanisms between simultaneous nucleation growth by supersaturation and simultaneous crystal death by dissolution result in the production of large but less crystals (Aamir, Nagy et al. 2010). In addition, this spontaneous process of crystal growth can be enhanced in the feed flow direction by augmenting the collision between small (*e.g.*, particle #1) and large (*e.g.*, particle #2) particles, as depicted in Fig. 5.8(b). Therefore, the total number of

crystals deposited on the membrane surface decreases with the operation time in high concentration MD.

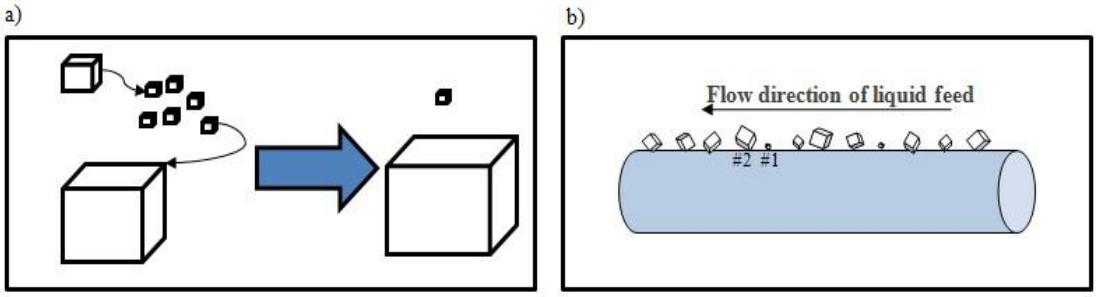

Fig. 5.8 Basic schematic of the Ostwald ripening principle (a) and phenomenon on fouled membrane surface (b)

Similar to the K_G derivation for Eq. (5.2), the rate constant of crystal nucleation K_B was regressed and obtained based on Eqs. (5.3) and (5.7) over given time interval, from the experimental data of crystal number corrected by the Ostwald ripening effect interval from. Then Eq. (5.3) can be revised as:

$$B = -9.73\times10^{11}G^{-0.83} \tag{5.25}$$

5.4.2.2 Calculation of critical crystal size

With the newly-derived crystal nucleation and growth rates expressions of Eqs. (5.24) & (5.25), the COMS modelling is expected to predict the crystal properties (size and number) as well as the critical point for the major flux deterioration associated with MD performance. The MD system can be operated normally without the scaling effect before the deposited crystals reach a critical size, which is identified as the corresponding crystal median size on the CSD curve at the critical point of flux decline and considered as a constant for membrane crystallization process under given conditions. It is mainly related to the material properties and membrane structure such as pore size, contact angle, porosity, etc. As discussed in section 5.4.1 (*i.e.*, Fig. 5.4, Set #1 experiments), the critical point of flux decline has been already identified at t= 6.60 h (point A) by applying the smoothing spline approach (Mathworks 2014). Therefore, the corresponding critical median size at the same

critical point (t=6.60 h) can be calculated based on the COMS computational diagram (Fig. 5.2). The output of the critical crystal size was obtained as 26 μm, indicating that the flux would drop sharply when the deposited crystals grow over this particular size. Thus, it can be used to predict the critical point for all batch-mode high concentration MD experiments in this study.

5.4.3 COMS model validation

As indicated in previous studies (Singh and Sirkar 2012; Adham, Hussain et al. 2013), the operating temperature of the feed solution has significant effect on the overall MD performance Therefore, to verify the critical crystal size method and the newly-established COMS mathematic model, another set of high concentration DCMD experiments (Set #2, in Section 5.3.2) were carried out at a different feed temperature of T_f=334 K and with the same membranes, initial solution concentration and flow rates. The variations of experimental membrane permeation flux and feed concentration in terms of operation time are presented in Fig. 5.9. Similarly to Fig. 5.4, the experimental critical point (point A') obtained from the differential algorithm indicates a dramatic flux decline appearing at t = 8.45 h. With the critical crystal size (26 μm) obtained in Section 5.4.2.2, the simulated critical point for experiments Set #2 appears at t = 8.46 h based on the COMS modelling. Obviously, this critical point from COMS modelling based on critical size is well agreed with the one derived from the experimental flux curve.

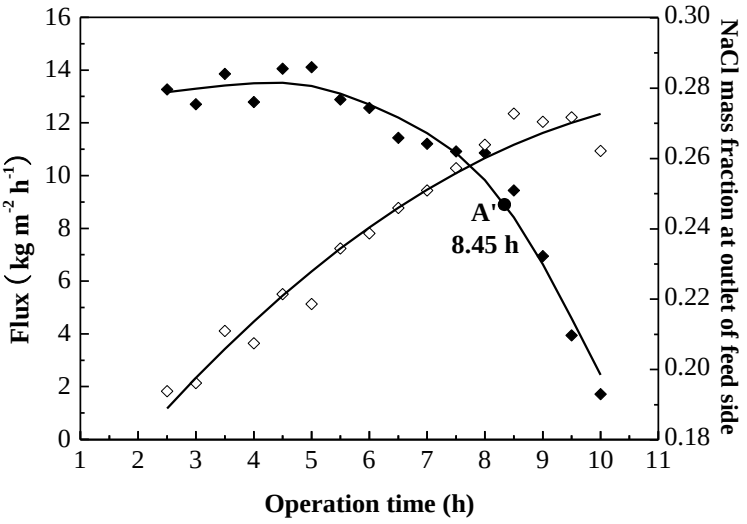

Fig. 5.9 Water flux and feed concentration profiles vs. operation time in high concentration DCMD experiments Set #2 (Q_f = 0.8 L min^{-1}; Q_p = 0.2 L min^{-1}; T_f = 334 K; T_p = 292 K; initial mass of feed solution: 1200 g; initial salt mass fraction of feed solution: 18%)

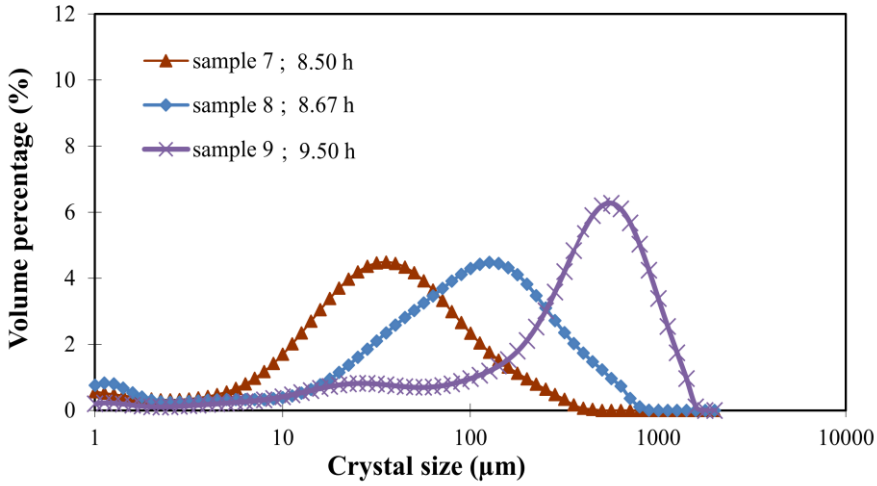

Fig. 5.10 The CSD of the crystals samples on the membrane surface at different time interval of DCMD experiments Set #2 (Q_f = 0.8 L min^{-1}; Q_p = 0.2 L min^{-1}; T_f = 334 K; T_p = 292 K; initial mass of feed solution: 1200 g; initial salt mass fraction of feed solution: 18%)

The reliability of the COMS model applied in this study is further verified by comparing the experimental crystals characteristics (median size and total number) with simulation results, as shown in Figs. 5.11 and 5.12. Three crystal samples in experiments Set #2 were withdrawn from the membrane surface at chosen operation times of 8.50 h, 8.67 h and 9.50 h, respectively. Similar to Fig. 5.6, the crystal size distribution profiles in Fig. 5.10 clearly indicates that the curves shift from left to right along the *x* axial. Consistently, Fig 5.11 shows that the crystal median size (black columns) increases with increasing operation time for samples 7 to 9. The COMS modelling results (white columns) using the revised crystallization kinetics (*i.e.*, Eqs. (5.24) & (5.25)) show a similar increasing trend and excellent agreement with the experimental data. Similarly, Fig. 5.12 shows the simulation results of the total crystal number at the same sampling times are fairly consistent with the experimental data. In a word, an acceptable average absolute relative error (*AARE*) ($\leq$ 10%) between the experimental and simulation data has confirmed the applicability of the newly-established COMS modelling approach, with which the crystallization process can be well monitored.

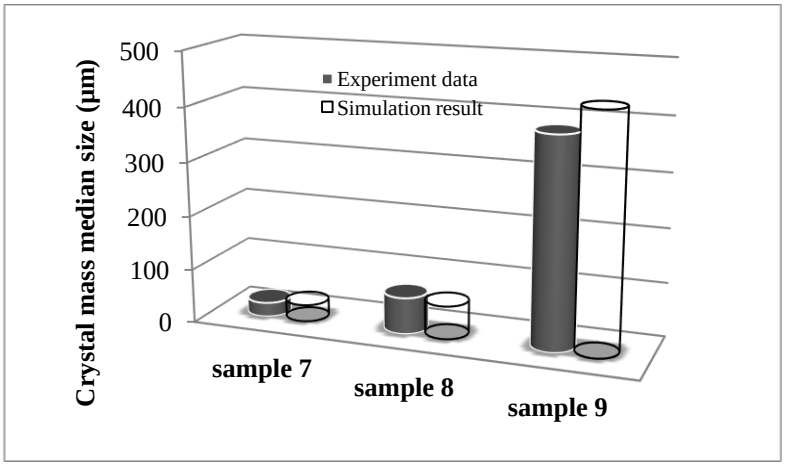

Fig. 5.11 Comparison of experimental and simulated crystal median size in terms of operation time of DCMD experiments Set #2 (Q_f = 0.8 L min^{-1}; Q_p = 0.2 L min^{-1}; T_f = 334 K; T_p = 292 K; initial mass of feed solution: 1200 g; initial salt mass fraction of feed solution: 18%)

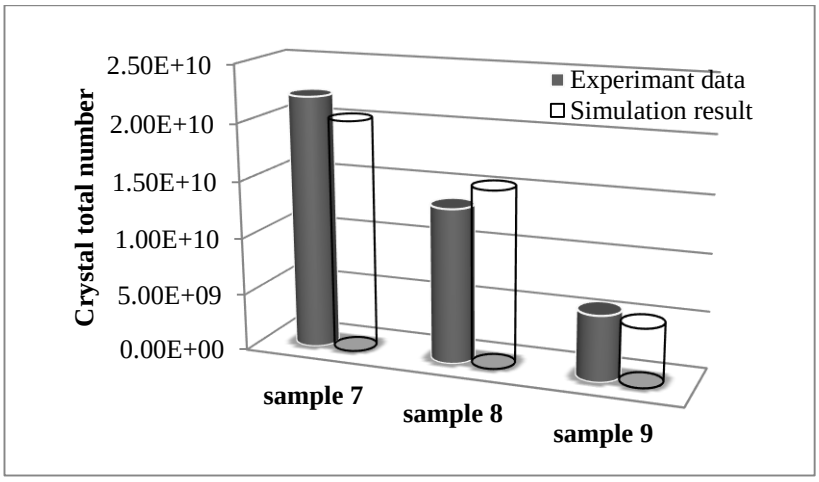

Fig. 5.12 Comparison of experimental and simulated total crystal numbers in terms of operation time of DCMD experiments Set #2 (Q_f = 0.8 L min^{-1}; Q_p = 0.2 L min^{-1}; T_f = 334 K; T_p = 292 K; initial mass of feed solution: 1200 g; initial salt mass fraction of feed solution: 18%)

5.5 Summary

This chapter has provided both the experimental study and the mathematical modelling to quantify the scaling formation in high concentration direct contact membrane distillation (DCMD) hollow fiber modules. The crystallization kinetics on the membrane surface was studied based on the evaluation of MD performance (critical point of major flux decline or scaling formation) and deposited crystal characteristics (size distribution, median size and total number). With the crystal nucleation and growth kinetic expressions derived from the regression of experimental data, a new modelling method named COMS involving both MD transport mechanisms and crystallization was established and verified. The COMS modelling has helped to quantify the crystal deposition on the membrane surface in terms of operating time and evaluate its influence on the overall MD process performance. Also, the definition of the critical size was proposed and the corresponding critical point of major MD flux decline can be estimated at different operation conditions. Overall, the modelling results in this study have shown the possibility for scaling control (*e.g.*, performance prediction and cleaning techniques) and implementation for MD applications of RO brine treatment with zero discharge.

CHAPTER 6

OPTIMIZATION OF OPERATING CONDITIONS FOR A CONTINUOUS MEMBRANE DISTILLATION CRYSTALLIZATION PROCESS WITH ZERO SALTY WATER DISCHARGE

6.1 Introduction

As mentioned in the previous chapters, membrane technology has been widely applied for water desalination and water treatment processes to address the ever-increasing potable water demand. Pressure-driven membrane processes such as reverse osmosis (RO) and nanofiltration (NF) have been successfully commercialized to produce high quality potable water (Chan 2005). However, the concentrated brine generated by these processes is normally discharged as a secondary waste stream that can increase the surface water salinity, negatively impact the environment, and thereby have economic and social consequences. This problem could become severe and even result in compromising the fresh water integral to human life (Wu, Kong et al. 1991; Gryta 2002; Guan, Wang et al. 2012).

A hybrid process that integrates MD with crystallization could offer a potential solution to this problem by enabling nearly complete water recovery and eliminating the secondary disposal problem. MD offers advantages relative to RO technology because it can handle a high concentration of salts at a low operating pressure using low grade waste heat (Chan 2005; Yun, Ma et al. 2006; Zuo, Wang et al. 2011; Chen, Yang et al. 2013). Pure water can be recovered in the MD stage and the resulting supersaturation of the soluble salt can serve as the driving force for the coupled

crystallization process from which precipitated solids can be produced for potential use. In this way MDC can realize zero discharge of concentrated brine to the environment.

As reviewed in Section 2.6, MDC showed great potential for concentrated brine treatment owing to its optimal control of the supersaturation level and uniform solid product features. Additionally, a comprehensive analysis of the MDC system was performed using an Aspen flowsheet simulation with a verified user-customized MD model to determine the energy consumption and to propose several strategies to enhance energy utilization (Guan, Wang et al. 2012). The results showed that the energy consumption of the crystallization component is less than 0.5% of the total energy consumption for the MDC hybrid system. This suggests that the crystallization unit has negligible influence on the total energy consumption of the MDC system. However, MDC hybrid system could produce high quality of pure water and solid crystals simultaneously.

Prior studies also indicate that there are several challenges to be addressed in order to develop a viable MDC process for concentrated brine treatment that include undesired crystallization in the membrane module and crystal blockage in the connecting tubing between the MD and crystallizer (Gryta 2002; Chan, Fane et al. 2005; Mariah, Buckley et al. 2006; Guan, Wang et al. 2012). Selecting proper operating conditions is crucial to determining the operation of both the MD and crystallization processes, preventing crystal deposition inside the membrane module (Curcio, Criscuoli et al. 2001; Chan, Fane et al. 2005) and obtaining the solid product from the crystallizer. However, no systematic studies focused on optimizing the continuous membrane distillation crystallization (CMDC) process have been published to date. Therefore, in this chapter CMDC was applied to a highly concentrated NaCl feed solution (26.7 wt% salt). The operating conditions including the flow rates and inlet temperatures on both the feed and permeate sides are systematically studied. In order to improve the product recovery (fresh water and solid NaCl) and better realize zero discharge, an experiment design using an orthogonal layout was applied for optimizing the operating conditions. The optimal

operating parameters determined from the analysis were validated experimentally. Since these operating conditions affect not only the CMDC performance but also the quality of the solid product obtained from the crystallizer, their effect on the crystal size distribution was also studied.

6.2 Theory

6.2.1 Continuous membrane distillation crystallization

In this chapter, a DCMD unit was integrated with a cooling crystallization unit. This hybrid process derives a potable water product from the MD unit. The retentate is cooled in the crystallizer unit in order to create a supersaturated metastable state that causes crystal nucleation and growth. The residual mother liquor is then separated from the crystalline solids and recycled to the feed tank. When this hybrid MD and crystallization process is operated in the continuous mode, it is referred to as continuous membrane distillation crystallization (CMDC). There are three circulation streams in the CMDC system: a feed stream, a permeate stream, and a recycle liquor stream. The recycle mother liquor stream connects the MD subsystem with the crystallizer. The flow rate of the recycle mother liquor stream is determined by the feed stream and permeation flux. Importantly, different temperatures must be maintained for each steam: a higher temperature for the feed steam to ensure that it is well below the salt saturation; a low temperature for the recycle steam going to the crystallizer to create supersaturation; and an even lower temperature for the permeate stream to provide a thermal driving force for the MD. In order to maintain a constant feed solution concentration, a brine solution needs to be continuously pumped into the feed tank to make up for the loss of solid salt in the crystallizer.

The performance of the CMDC is indicated by the production of pure water and solid NaCl crystals. The transmembrane flux can be determined from the overall mass-transfer coefficient and the water vapour pressure difference across the membrane:

$$J = C(P_{fm} - P_{pm}) \tag{6.1}$$

where J is the transmembrane flux (kg m^{-2} s^{-1}), C is the mass-transfer coefficient (kg m^{-2} s^{-1} Pa^{-1}) for the membrane, and P_{fm} and P_{pm} are the saturated vapour pressures (Pa) adjacent to membrane surface on the feed and permeate side, respectively. The effect of the salt concentration on the vapour pressure on the feed side of the membrane is insignificant for low concentrations. However, when the concentration of the feed increases to a high level, in particular, close to saturation, the vapour pressure driving force can be significantly influenced by the solute content; this effect is incorporated into Eq. (6.1) as follows:

$$J = C(P_{fm}(1-x_m)\gamma - P_{pm}) \tag{6.2}$$

where x_m is the mole fraction of salt at the membrane surface on the feed side, γ is the activity coefficient, which is given by the following equation for a salt solution (Schofield, Fane et al. 1990; Gryta 2002):

$$\gamma = 1 - 0.5x_m - 10x_m^{\ 2} \tag{6.3}$$

Obviously, an increase in the mole fraction of the feed solution will lead to a reduced driving force and a flux decline.

An overall mass balance provides a relationship between the mass production fluxes of the pure water, M_{pro_water}, and the solid crystals, $M_{pro\_crystal}$:

$$\frac{M_{pro-water}}{1-X} = \frac{M_{pro\_crystal}}{X} \tag{6.4}$$

where X is the NaCl mass fraction in the feed solution. The total yield is proportional to the membrane area of the MD module. Hence, the product production rates are expressed per unit area of membrane (kg m^{-2} day^{-1}).

6.2.2 Crystallization

A balance on the salt for the crystallizer is given by

$$c_{sus} \times Q_{in} = c_{out} \times Q_{out} + m_{solid} \tag{6.5}$$

Where c_{sus} is the concentration (kg m^{-3}) of the retentate solution leaving the MD unit and entering the crystallizer; c_{out} is the concentration (kg m^{-3}) of the liquid leaving the crystallizer; m_{solid} is the mass production of the NaCl crystals from the

crystallizer (kg min^{-1}); and, Q_{in} and Q_{out} are the volumetric fluxes (L min^{-1}) into and out of the crystallizer. Assuming $Q_{in} = Q_{out} = Q$ permits transforming Eq. (6.5) into the following form:

$$m_{solid} = (c_{sus} - c_{out}) \times Q = \int_{l_1}^{l_n} \rho_s \phi_v l^3 n(l) dl \approx \sum_{i=1}^{n} \rho_s \phi_v l_i^3 N_i \tag{6.6}$$

Where ρ_s is NaCl mass density (2.163 kg m^{-3}), ϕ_v is the shape factor (1 for cubic NaCl crystals), l is the characteristic size of crystals (μm) and $n(l)$ is the population density (No. μm^{-1}) of the crystals having size l. N_i it the total number of crystals having a characteristic size between l_i and l_{i+1} and is given by

$$N_i = \int_{l_i}^{l_{i+1}} n(l) dl \tag{6.7}$$

The volume percent of the crystals having size l_i then is given by

$$\text{Volume percent (\%)} = \frac{N_i l_i^3}{\sum N_i l_i^3} \tag{6.8}$$

The CSD, which is an important metric characterizing the solid product of the CMDC process, will be expressed in terms of the volume percent of crystals of a particular size as a function of crystal size.

In crystallization processes the nucleation and growth kinetics are the two dominant phenomena that determine the crystal size (Nývlt, Söhnel et al. 1985). The power-law model is usually used to express the nucleation and growth rate:

$$G = K_G (c_{sus} - c^*)^g \tag{6.9}$$

$$B = K_B G^b \tag{6.10}$$

where c^* is the equilibrium saturation concentration at the temperature in the crystallizer. The kinetic crystal growth rate constant K_G, nucleation rate constant K_B, and exponents g and b can be obtained from a regression analysis on the experimental data. From Eq. (6.9) it can be seen that the supersaturation level, $(c_{sus} - c^*)$, is the driving force for crystal nucleation and growth that determines the crystal size and distribution of the final product. Hence, in the CMDC process we must consider how the temperature and flow rate in the MD unit can affect the

solution concentration *(c_{sus})* and temperature (c^*) in the crystallizer that in turn will affect the overall CMDC performance.

6.3 Experimental

6.3.1 Apparatus and materials

The set-up of the CMDC apparatus that combines DCMD with crystallization is shown in Fig. 6.1. The bulk temperatures and pressures were measured by thermocouples connected to a data-acquisition system. The flow rates were monitored by in-line digital flow meters. The water flux was determined from the weight gain in the cooled permeate reservoir and recorded every thirty minutes. In the MD part of the apparatus the temperature of the feed solution was maintained by a heating bath (Polyscience® 9105); the temperature of the permeate reservoir was kept constant using a cooler (Julabo® F25). The feed and permeate were circulated using a peristaltic pump (Masterflex®, Cole Palmer). The crystallizer had an internal stirrer and its temperature was maintained by water that was circulated in a cooled jacket (Julabo® F25). The effluent from the crystallizer was passed through an alumina filter to separate the suspended solids from the saturated solution. In this chapter, similar PVDF membrane (characterized experimentally in Chapter 3) was used to fabricate MD modules. The parameters of the hollow fiber membrane module are listed in Table 6.1.

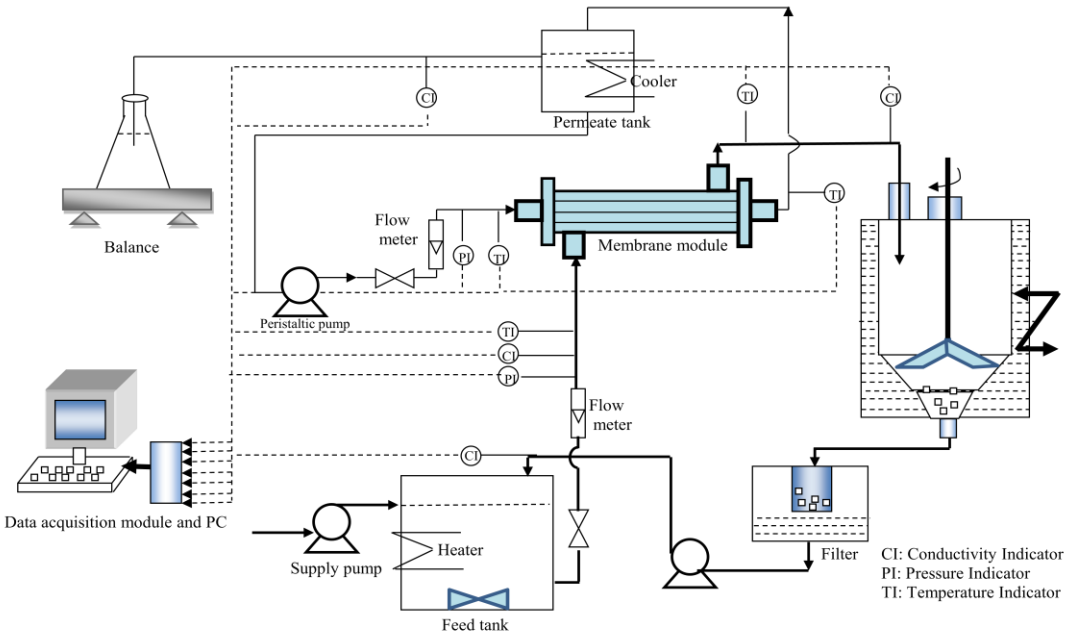

Fig. 6.1 Experimental set-up for the CMDC process

Table 6.1 Parameters of hollow fiber membrane module

Parallel module number	**Housing diameter, d_s (mm)**	**No. of fibers in each module**	**Effective fiber length, L_m (mm)**	**Membrane area, A (cm^2)**
2	12	25	410	661.7

A concentrated NaCl solution (26.7%) served as the feed stream for the CMDC experiments. Sodium chloride having 99.5% purity was purchased from Merck. Milli-Q ultrapure deionized (DI) water was used to prepare the solutions. HPLC-grade isopropanol (IPA) for the crystal analysis was purchased from Fisher.

6.3.2 Design of the experiments

6.3.2.1 Orthogonal fractional factorial (OFF) experiment design

On the lab scale or industrial scale it can be extremely costly to run a large number of experiments to test the influence and combinations of all factors in a chemical process. Hence, a judicious experiment design is necessary, especially for a multi-parameter chemical process such as CMDC. This can not only simplify and standardize experiment operations, but also permits identifying critical parameters

and optimizing a chemical process (Ravanchi, Kaghazchi et al. 2009). Hence, an experimental design method was applied to enable a systematic study of the CMDC in this study, whereby it was referred to as "orthogonal fractional factorial (OFF)" experiment design. In this OFF experiment design fractional factorial design has been standardized as orthogonal layouts for different factors with certain levels, such that only a small number of experiments are necessary rather than the large number that are required for a full factorial experiment. By range analysis (to be described in section 4.2.2) for the experiment results, it is possible to assess the dominant factors and the optimal operating conditions. A flow diagram for the implementation of the OFF experiment design is shown in Fig. 6.2.

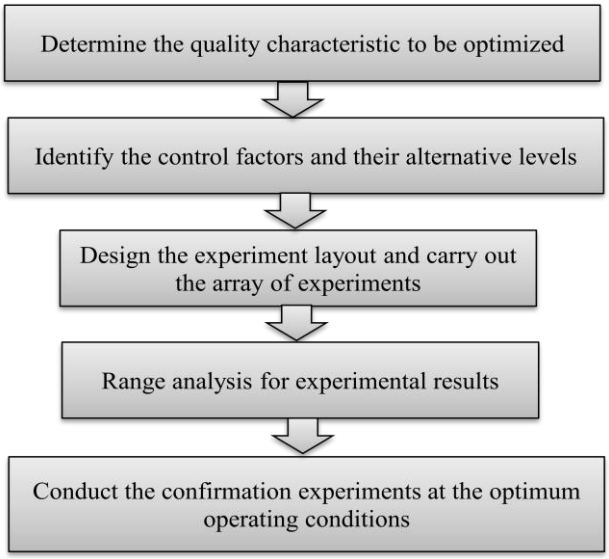

Fig. 6.2 Flow chart for orthogonal fractional factorial (OFF) experiment design method

6.3.2.2 Choice of the quality characteristic

As indicated in Fig. 6.2, the objective quality characteristic, which is the output or the response variable to be observed, must be determined first. For CMDC with zero discharge, two products are involved: pure water from the DCMD and solid NaCl from the crystallizer. Moreover, the quantity of pure water and solid NaCl are interrelated as indicated by Eq. (6.4). From Eq. (6.4) it is seen that the NaCl solid production can be determined from the pure water production. Hence, only one

experiment output needs to be chosen as the quality characteristic for the CMDC process. Since in desalination processes the pure water production usually is the criterion by which process performance is evaluated (Kubota, Ohta et al. 1988; Schofield, Fane et al. 1990; Kobayashi, Chai et al. 1999; Knyazkova and Kavitskaya 2000; Chan, Fane et al. 2005), it is chosen as the quality characteristic for the fractional factorial experiment design in this study.

6.3.2.3 Control factors and levels for CMDC

In order to determine the suitable fractional factorial design, the main factors and their corresponding levels must be chosen for the CMDC experiments. MD is a process that involves coupled mass- and heat-transfer processes (Lawson and Lloyd 1997; Alklaibi and Lior 2006; Yang, Wang et al. 2011; Yang, Wang et al. 2011; Yu, Yang et al. 2012). As such, in DCMD using a hollow fiber membrane module the flow rates and temperatures on both the shell and lumen sides are the major operating parameters or factors that influence the water permeation flux. Similarly, these four factors also have a major influence on the NaCl crystal production due to its interrelationship with the water flux in the CMDC process. Hence, in this study an OFF experiment design for these four factors at three levels was used to evaluate their impact in the multi-parameter CMDC process as summarized in Table 6.2.

Table 6.2 The OFF test factors and levels

Factor (k_{factor})		**Units**	**Level (t)**		
			1	**2**	**3**
1	Feed flowrate, Q_f	L min^{-1}	0.49	0.64	0.78
2	Feed inlet temperature, T_{fi}	K	333	338	341
3	Permeate flowrate, Q_p	L min^{-1}	0.35	0.70	0.88
4	Permeate inlet temperature, T_{pi}	K	288	293	303

The OFF experiment designs are expressed using the notation $Ln(t^k)$, where L is the symbol of the orthogonal layout; n describes the number of experiments instead of the full factorial experiments; t is the number of levels of each factor investigated and k is the number of factors investigated. Therefore, the orthogonal array applied

for this study was the *L9(3^4)*, where the experiment requires only 9 runs rather than the 81 runs that would be required for the full 3^4 factorial experiment. The details of the *L9(3^4)* orthogonal array are summarized in Table 6.3. The numbers 1, 2 and 3 denote the three levels for the four control factors. Each row of Table 6.3 represents a run for which each of the four factors is specified at one of the three levels. This OFF experiment design permits identifying the most important factor(s) and optimal operating conditions for the CMDC process. The manner in which this is done will be described in the discussion of the results.

Table 6.3 Experimental layout using an *L9(3^4)* orthogonal array

	Factors			
Experiment number	**Feed flow rate**	**Feed inlet temperature**	**Permeate flow rate**	**Permeate inlet temperature**
#1	1	1	1	1
#2	1	2	2	2
#3	1	3	3	3
#4	2	1	2	3
#5	2	2	3	1
#6	2	3	1	2
#7	3	1	3	2
#8	3	2	1	3
#9	3	3	2	1

6.3.3 Experiment procedure

A saturated NaCl solution at room temperature was prepared (8.3 L) and heated (in the range of 333~341 K) in the feed tank before running the CMDC apparatus (shown in Fig. 6.1). The 8.3 L crystallizer and the 1.5 L supply tank were filled with the same concentration NaCl solution. On the lumen side DI water was cooled in the range 288~303 K and circulated at a rate of 0.35~0.88 L min^{-1} by a peristaltic pump. The feed solution was circulated on the shell side of the membrane module. The concentrated retentate solution was pumped at a rate of 0.49~0.78 L min^{-1} into the crystallizer by another peristaltic pump. In this way the DCMD operated in a co-current contacting mode. The permeate was collected in an overflow tank sitting on a balance whose resolution was ±0.1 g. The relatively low temperature in the

crystallizer caused supersaturation and the formation of small crystals. The effluent from the crystallizer was passed through a filter that separated the suspension into solid crystals and mother liquid that was circulated back into the feed tank, thereby maintaining a continuous process.

After steady operating conditions were maintained for two hours, the pure water production was determined and crystal samples were collected every 30 minutes. The dried crystals were analyzed to determine the crystal size distribution (CSD) using a Malvern Mastersizer 2000 with HPLC-grade IPA as the liquid dispersion medium. The results for the pure water production assessment and crystal sample analyses reported in the discussion of results represented the average of three replicates.

Conductivity meters having an accuracy of ±0.1 ms cm^{-1} and ±0.1 μs cm^{-1} on the feed and permeate sides, respectively, were used to monitor the concentration of the fluids. The temperature and flow rates were controlled within ±0.5 °C and ±0.01 L min^{-1}, respectively.

6.4 Results and discussion

6.4.1 Feasibility of the CMDC experiments

First, an experiment was carried out to determine whether the CMDC could be run continuously to obtain pure water and solid NaCl products. The operating conditions were a flow rate and temperature on the feed side of 0.64 L min^{-1} and 338 K, respectively, and on the permeate side of 0.88 L min^{-1} and 303 K, respectively. Fig. 6.3 is a plot of the water permeation flux and conductivity as a function of time for this experiment that lasted slightly more than 12 hours. The membrane was rinsed in-situ with pure water approximately every 4 hours in order to remove crystalline deposits that caused a decrease in the permeability and a gradual decline in flux. In each rinsing cycle, pure water at the room temperature was circulated throughout the shell side of MD module for 10 mins with a rate of 0.2 L min^{-1}, while the flowrate and temperature of permeate fluid was maintained unchanged.

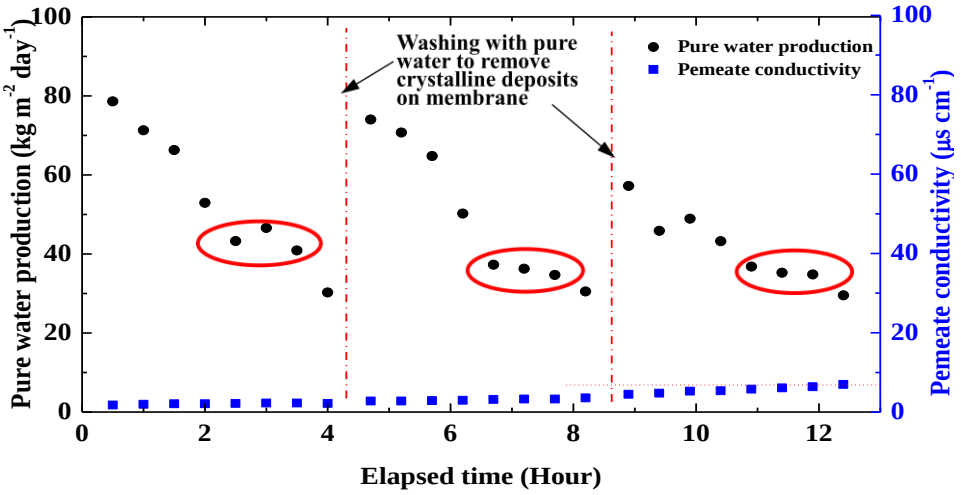

Fig. 6.3 Permeate product flux and conductivity versus elapsed time for CMDC for a feed flow rate and temperature of 0.64 L min^{-1} and 338 K and a permeate flow rate and temperature of 0.88 L min^{-1} and 303 K. Dashed vertical lines indicate when the membrane was washed with pure water for ten minutes and red circles indicate stable operation.

Between each rinsing cycle the water permeation flux displayed a similar trend that can be divided into three phases. In the first phase the water permeation flux gradually decreased owning to the increase of the recycled feed solution concentration from initial 26.4% to approximately 26.7% NaCl mass fraction. This decline in the water flux with the feed solution concentration can be explained by Eq. (6.2). After approximately 2 hours into the first phase, the CMDC process entered the second phase during which a nearly constant water permeation flux and feed solution concentration were maintained for 2.0 ~ 3.5 hours (denoted by the red circles in Fig. 6.3). During the third phase, some tiny crystalline deposits formed on the membrane owing to concentration polarization causing supersaturation of the NaCl near its surface. These crystalline deposits caused a decrease in the membrane permeability and a slight decline in the water flux. Hence, washing with the pure water was used to remove the crystalline deposits and restore the water flux to nearly its initial value after which it again declined following the same trend with three phases.

Fig. 6.3 indicates that the periodic washing process could be sustained to give a product water with a very low conductivity (< 7.5 μs). However, the permeate conductivity gradually increased after each washing. It is possible that the fouling on the membrane surface compromised membrane hydrophobicity and accelerated wetting, which resulted in the slight decline of the maximum and stable permeation flux after each washing (Gryta 2002; Gryta 2005; Goh, Zhang et al. 2013). Since the surface morphology strongly influences wetting, the membrane surface before and after an experiment was examined via scanning electron microscopy (SEM). The micrographs in Fig. 6.4 indicate that there are some streaks on the membrane surface after its use. This suggests that the rinsing did not restore the membrane to its initial condition as noted by the streaks, which may slightly change the membrane structure and cause local wetting (Gryta 2005).

6.4.2 OFF experiment design results and analysis

6.4.2.1 Results for the OFF experiment design

As outlined in section 6.3.2.3, the feed flow rate and inlet temperature, and permeate flow rate and inlet temperature were selected as the control factors for the OFF experimental design to assess the CMDC performance. The pure water production flux was chosen as the quality characteristic in the $L9(3^4)$ orthogonal array design. The nine experiments were carried out according to the experiment design arrangement summarized in Table 6.4. Fresh hollow fiber membranes were used for each experiment, all of which were run for a relatively short period of time to avoid crystalline deposition on the membrane surface. The results are summarized in Table 6.4.

Table 6.4 The OFF test results and calculation average responses

	Factors				
Experiment number	**Feed flowrate (L min^{-1})**	**Feed inlet temperature (K)**	**Permeate flowrate (L min^{-1})**	**Permeate inlet temperature (K)**	**Pure water production (kg m^{-2} day^{-1})**
#1	0.49	333	0.35	288	48.28
#2	0.49	338	0.70	293	44.74
#3	0.49	341	0.88	303	39.56

#4	0.64	333	0.70	303	60.37
#5	0.64	338	0.88	288	48.19
#6	0.64	341	0.35	293	62.32
#7	0.78	333	0.88	293	20.63
#8	0.78	338	0.35	303	66.56
#9	0.78	341	0.70	288	25.77
I_1	132.58	129.27	177.16	122.24	
I_2	170.88	159.49	130.88	127.69	
I_3	112.96	127.65	108.38	166.49	
$\bar{I}_1$	44.19	43.09	59.05	40.75	Y=46.27
$\bar{I}_2$	56.96	53.16	43.63	42.56	
$\bar{I}_3$	37.65	42.55	36.13	55.50	

The average pure water production flux (kg m^{-2} day^{-1}) for the nine experiments can be determined from the data in Table 6.4 and is given by the following:

$$Y = \frac{1}{9} \times \sum y_n = 46.27 \qquad (n=1, 2, 3 \ldots 9) \tag{6.11}$$

where y_n is the water production flux of the n^{th} experiment run in the OFF test. In the OFF experiment design, the average result for each level for a particular factor can indicate its influence at this level. Hence, by analyzing the average results for each factor, information can be obtained on how the factor affects the CMDC process. For example, the first three runs for the feed flow rate were conducted at 0.49 L min^{-1} (level 1). Hence, these three runs should belong to one subgroup for this factor. Runs #4 to #6 and #7 to #9 belong to the other two subgroups for levels 2 and 3, respectively. The total (I_1, I_2, I_3) and average ($\bar{I}_1$, $\bar{I}_2$, $\bar{I}_3$) values can be calculated for each subgroup. For level 1 of the feed flow rate, the I_1 and $\bar{I}_1$ values are 132.58 and 44.19, respectively. The resulting values for the three subgroups for each of the four control factors are summarized in Table 6.4.

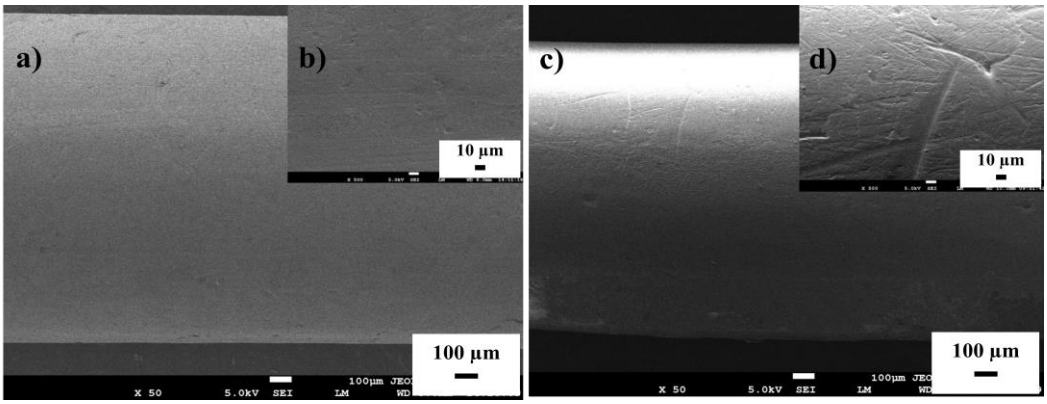

Fig. 6.4 SEM micrograph of PVDF membrane surface morphology: a) original membrane surface with magnification 50 times; b) original membrane surface with magnification 500 times; c) used membrane surface with magnification 50 times; d) used membrane surface with magnification 500 times.

The influence of each factor on the CMDC performance can be assessed by comparing the average pure water production flux for each level ($\bar{I}_1$, $\bar{I}_2$, $\bar{I}_3$) in graphical form as shown in Fig. 6.5. Fig. 6.5(a) shows the effect of the feed flow rate factor on the production fluxes of the pure water and NaCl solid. Note in Fig. 6.5(a) that both the pure water and NaCl solid production fluxes display a maximum with respect to increasing feed flow rate. A possible explanation for this maximum is that the initial increase in feed flow rate increased the Reynolds number and thereby improved the hydrodynamics adjacent to the membrane. This decreased the thickness of the thermal and solute boundary layers near the membrane and thereby increased the heat and mass transfer, which resulted in an increase in the water permeation flux (Yang, Wang et al. 2011; Yang, Yu et al. 2012). This increased permeation flux resulted in a more concentrated retentate from the DCMD and a higher degree of saturation in the feed to the crystallizer, thereby resulting in an increase in the solid NaCl product. However, at higher feed flow rates the water and solid NaCl production fluxes decreased. This is thought to be due a complex interaction between the DCMD unit and the crystallizer. The decreased residence time in the crystallizer resulted in less salt being crystallized and thereby a higher concentration in the effluent stream that is recycled to the DCMD unit. The higher concentration in the feed to the DCMD unit (from 26.5% to 26.8%) causes a reduction in the vapour

pressure described by Eq. (6.2) that decreases the driving force for the MD process (Gryta 2002). The reduced water production flux in the DCMD unit in turn results in an increased temperature of the retentate that serves as the feed to the crystallizer. This compounds the effect of the decreased residence time and results in less solid NaCl production in the crystallizer (Nývlt, Söhnel et al. 1985).

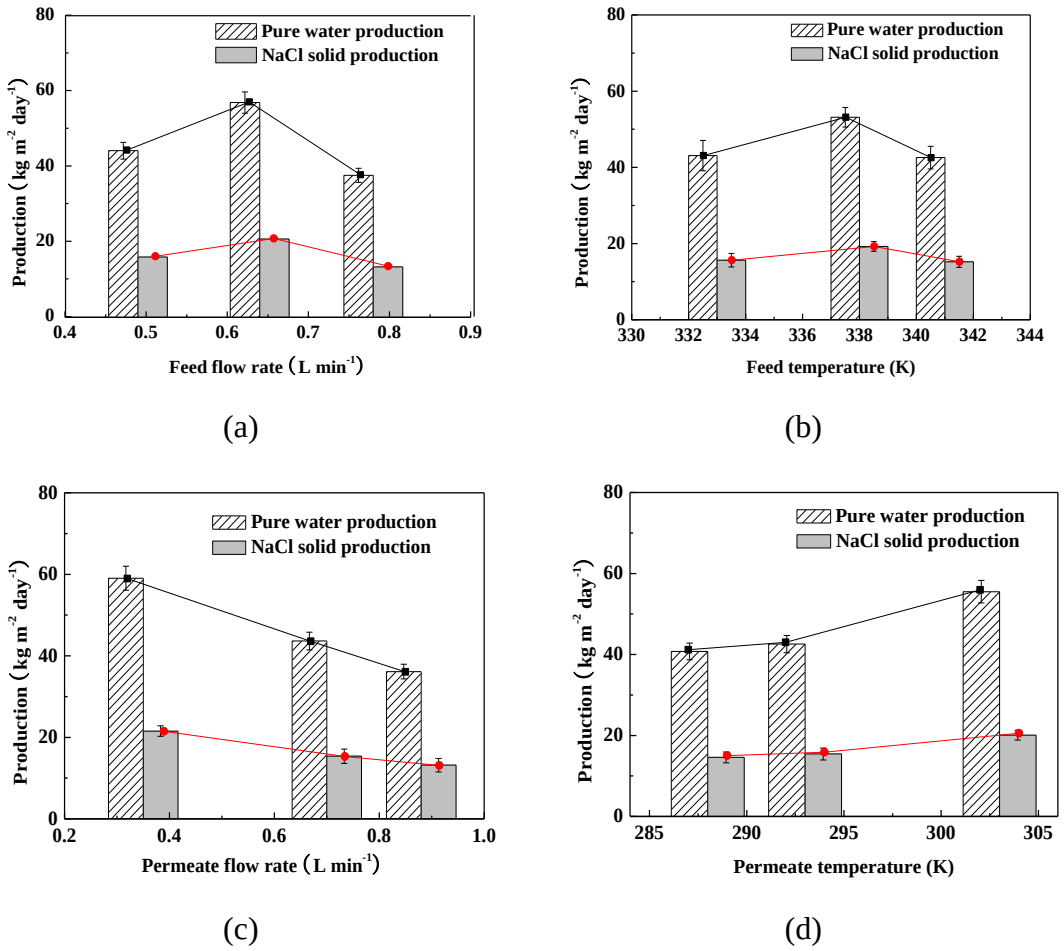

Fig. 6.5 Factor effect chart on pure water and NaCl production: a). feed flow rate; b). feed temperature; c). permeate flow rate; d). permeate temperature

Fig. 6.5(b) shows a graph of the pure water and NaCl solid production fluxes as a function of the feed inlet temperature factor in the CMDC. Both the pure water and NaCl solid production fluxes display a maximum with respect to increasing feed inlet temperature. Again this is thought to be due a complex interaction between the DCMD unit and the crystallizer. The initial increase in temperature increased the

vapor pressure and thereby increased the water production flux. This in turn increased the supersaturation of the retentate that is fed to the crystallizer and thereby increased the solid NaCl production flux. However, a further increase in the feed inlet temperature increases the cooling load in the crystallizer and thereby results in a reduction in the solid NaCl production flux. This in turn increases the concentration in the effluent stream from the crystallizer that is recycled to the DCMD unit and thereby decreases the water production flux.

Fig. 6.5(c) shows a graph of the pure water and NaCl solid production fluxes as a function of the permeate-side flow rate in the CMDC. Both the pure water and NaCl solid production fluxes show a monotonic decrease with increasing permeate-side flow rate. An increase in the permeate-side flow rate can have competing effects on the production fluxes of the products. An increase in the permeate-side flow rate causes an increase in the Reynolds number, thereby decreasing the temperature polarization on the permeate side that in turn increases the water permeation. However, this increase in the Reynolds number that reduces the convective heat transfer resistance on the permeate side can also cause an increase in the conductive heat loss through the membrane (Yu, Yang et al. 2011), thereby causing a decrease in the feed-side temperature and correspondingly the vapour pressure driving force for water permeation through the membrane. Any decrease in temperature on the feed side can also cause crystalline deposition on the membrane, which reduces the permeation. The latter effect would be more likely to occur for MD with a concentrated feed solution. Any reduction in the water permeation flux will cause the concentration of the retentate from the MD unit to decrease, thereby causing a reduction in the solid NaCl production flux in the crystallizer. Fig. 6.5(c) suggests that for the concentrated feed considered in this study the increase in conductive heat loss possibly accompanied by some crystallization on the membrane was the dominant mechanism that caused the progressive decline in water and solid NaCl production fluxes with increasing permeate-side flow rate.

Fig. 6.5(d) shows a graph of the pure water and NaCl solid production fluxes as a function of the permeate-side temperature in the CMDC. Both the pure water and

NaCl solid production fluxes show a monotonic increase with increasing permeate-side temperature. Increasing the permeate-side temperature will reduce the vapor-pressure driving force for water permeation through the membrane. However, it also will decrease the conductive heat loss through the membrane and increase the temperature on the feed-side of the membrane. The former effect causes a decrease in the water permeation flux and the latter reduces the tendency for crystallization to occur on the membrane. Any increase in the water production flux results in an increase in the concentration of the retentate from the MD unit that in turn increases the production of solid NaCl in the crystallizer. The results in Fig. 6.5(d) suggest that the reduction in conductive heat loss was the dominant mechanism that caused the increase in the water and solid NaCl production fluxes with an increase in the permeate-side temperature (Yu, Yang et al. 2011). However, ultimately an increase in the permeate-side temperature has to cause a decrease in both the water and solid NaCl production fluxes owing to its effect on the overall vapor pressure driving force in the MD unit. The results shown in Fig. 6.5(d) are a consequence of having a large temperature difference between the feed and permeate sides of the MD unit. Note that the feed-side temperature increased from 333 to 341 K and the permeate-side temperature increased from 288 to 303 K, thereby causing a decrease in the overall temperature driving force from 45 to 38 K in going from level 1 to level 3. The results in Fig. 6.5(d) indicate that the negative effects of the decrease in overall temperature driving force were dominated by the positive effects of the reduction in conductive heat loss and reduced crystallization on the membrane.

In summary, since the CMDC process necessarily has a much higher salt concentration in the feed in order to facilitate precipitation of solid NaCl in the crystallizer, its response to the operating parameters can be markedly different than conventional MD that has a much lower salt concentration (Wang, Gu et al. 2009; Zuo, Wang et al. 2011; Yu, Yang et al. 2012). The OFF design experiments indicate there are optimal values for the feed flow rate and temperature. Moreover, the CMDC process should be run at a relatively low flow rate and relatively high temperature on the permeate side, provided that a large temperature driving force is maintained between the feed and permeate sides of the membrane. Range analysis

will be employed in the following section to determine optimal operating conditions for the CMDC process.

6.4.3 Range analysis and optimal conditions confirmation

Range analysis is a design strategy whereby the results of OFF design experiments are used to identify the principal operating parameter(s) and to determine optimal operating conditions. Applying range analysis involves first determining D_t, the difference between the average pure water production flux for the three levels of the k^{th} factor (*i.e.*, k = 1~4) and the average pure water production flux for the 9 runs:

$$D_t = \bar{I}_t - Y \qquad (t=1, 2, 3) \tag{6.12}$$

There are three values of D_t, for each of the four factors. The metric D_t is a measure of the production flux of the particular factor at the level t relative to the average production flux. For each factor there will be maximum and minimum values of D_t denoted by R_{max} and R_{min}, respectively. The metric T defined by Eq. (6.13) is a measure of the importance of the particular factor in terms of its influence on the pure water production flux:

$$T = R_{\max} - R_{\min} \tag{6.13}$$

A large value of T implies that varying the particular factor causes a large change in the quality characteristic, which for CMDC is the pure water production flux.

Table 6.5 Range analysis

No.	D_1	D_2	D_3	R(max)	R(min)	T
1	-5.43	7.34	-1.91	7.34	-5.43	12.77
2	-0.38	3.54	-3.16	3.54	-3.16	6.70
3	9.43	-2.08	-7.34	9.43	-7.34	16.77
4	-4.97	-0.91	5.87	5.87	-4.97	10.84

Table 6.5 summarizes the resulting values of D_1, D_2, D_3, R_{max}, R_{min} and T for the four factors considered in this analysis, namely the feed flow rate, feed inlet temperature, permeate-side flow rate and permeate inlet temperature. The largest values of T are seen to be 22.92 for the permeate-side flow rate and 19.31 for the feed flow rate.

Hence, the permeate-side and feed flow rates are the principal factors that influence the performance of the CMDC process. The optimal values of the factors can be estimated from the largest values of D_t for each factor. Defining D_{tk} to be the value of D_t for the k^{th} factor at the t^{th} level, the inspection of the D_{tk} values in Table 6.5 indicates the following: $D_{21} > D_{31} > D_{11}$; $D_{22} > D_{12} > D_{32}$; $D_{13} > D_{23} > D_{33}$; and $D_{34} > D_{24} > D_{14.}$ This implies that the optimal values of the four factors based on the nine runs for OFF experiment design are the following: feed flow rate = 0.64 $L \cdot min^{-1}$; feed inlet temperature = 338 K; permeate-side flow rate = 0.35 L min^{-1}; and permeate inlet temperature = 303 K. However, it should be pointed out that these values do not represent a global optimum but rather optimum values based on the nine runs whose conditions are summarized in Table 6.4.

Confirmation of the results of OFF design strategy was obtained by conducting an experiment at the optimal values determined based on the nine runs. The resulting pure water production flux was 72.66 kg m^{-2} day^{-1} and the NaCl solid production flux was 26.06 kg m^{-2} day^{-1}, both of which are greater than any of the production fluxes obtained in the nine runs summarized in Table 6.4.

6.4.4 Effect of the four factors on crystal size distribution

One of the objectives of the CMDC process is to obtain a high production flux of good quality solid products. The OFF design permitted maximizing the production flux of both the water and the solid NaCl products. The mean diameter and CSD are important in terms of the quality of the crystalline product and insofar as their influence on subsequent washing, filtering, transportation, and storage processes. Large crystals having a uniform size are usually desired (Ji, Curcio et al. 2010; Edwie and Chung 2012). Fig. 6.6 shows an SEM image of the NaCl crystalline product obtained using the optimal values of the four factors that shows a more-or-less cubic structure and a range of particle size.

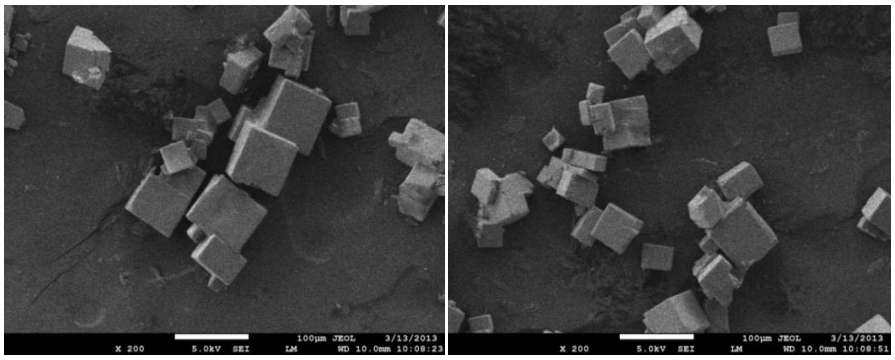

Fig. 6.6 SEM micrograph (magnification 500 times) of sodium chloride crystals with cubic structure

Whereas the OFF experiment design permits optimizing the values for the operating parameters of the CMDC process to obtain the maximum product fluxes, it does not address the properties of the resulting solid product. Hence, a series of experiments was done to explore the effects of the four factors (feed flow rate and inlet temperature and permeate-side flow rate and inlet temperature) on the CSD of the final solid products. Each of the four factors was varied over a range of values while the other three factors were held constant. The CSD for each experiment was represented in terms of the volume percent of the crystals having size l_i defined by Eq. (6.8) as a function of l. The resulting CSDs for each of the four factors are summarized in Fig. 6.7. All the CSDs are seen to be unimodal with a relatively narrow size distribution. This is probably because the retentate from the MD unit in the CMDC process has a nearly constant degree of supersaturation for fixed values of the four factors. Fig. 6.7(a) indicates that the feed flow rate has the strongest influence on both the mean crystal size and the CSD; the mean crystal size l increased from 138.9 to 216.5 μm when the feed flow rate decreased from 0.78 to 0.49 L min^{-1}. Undoubtedly this is a result of the increased residence time in the crystallizer that permitted more crystal growth. Fig. 6.7(b) indicates that the feed temperature also had a reasonably large influence on the mean crystal size; the crystal mean size decreased from 209.9 to 188.1 μm when the feed temperature increased from 333 to 341 K. A higher temperature of the feed into the crystallizer results in an increased cooling load and a decrease in the driving force for crystal

growth. The permeate-side flow rate and inlet temperature have some influence on the CSD but have less influence on the mean crystal size.

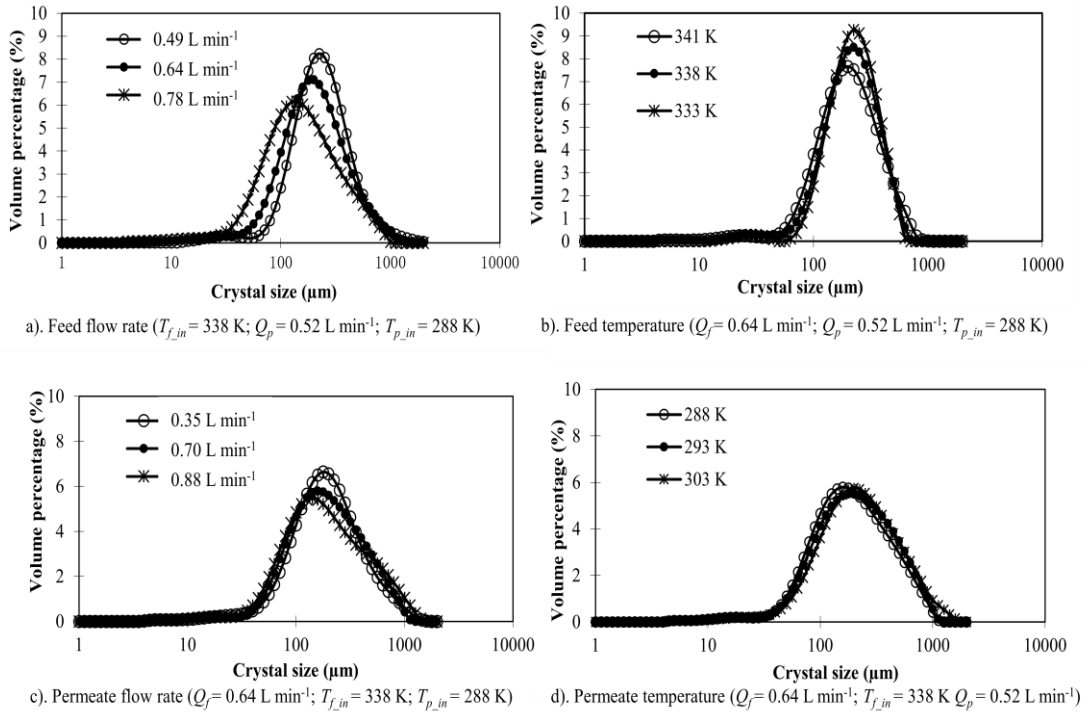

a). Feed flow rate (T_{f_in} = 338 K; Q_p = 0.52 L min^{-1}; T_{p_in} = 288 K)

b). Feed temperature (Q_f = 0.64 L min^{-1}; Q_p = 0.52 L min^{-1}; T_{p_in} = 288 K)

c). Permeate flow rate (Q_f = 0.64 L min^{-1}; T_{f_in} = 338 K; T_{p_in} = 288 K)

d). Permeate temperature (Q_f = 0.64 L min^{-1}; T_{f_in} = 338 K Q_p = 0.52 L min^{-1})

Fig. 6.7 Factor effect on crystal size distribution

6.5 Summary

In this chapter, the CMDC process has been shown to permit obtaining pure water and solid NaCl products from a concentrated feed. An orthogonal fractional factorial (OFF) experiment design was used to identify the operating parameters that affect the production of water and NaCl products. The water production flux was identified as quality characteristic since the water and NaCl production fluxes are interrelated. The feed flow rate and inlet temperature and permeate-side flow rate and inlet temperature were identified as the four factors whose influence on the water production flux was to be assessed. The OFF experiment design permitted studying the effect of three levels for each of the four factors via only nine experiments. The range analysis of the results of these nine experiments identified the feed and permeate-side flow rates as the most influential factors affecting the water production

flux. The OFF experiment design also permitted determining the optimal values of the four factors based on the nine experiments. A subsequent experiment run using these optimal values of the four factors resulted in fluxes of both the water and solid NaCl that exceeded any obtained in the nine experiments. This confirmed the merits of the OFF experiment design and analysis in determining optimal operating conditions for the CMDC process.

An ancillary study of the effect of the four factors on the mean crystal size and CSD indicated that the feed flow rate and inlet temperature were the dominant factors. An increase in the feed flow rate resulted in a smaller mean crystal size owing to a reduction in the residence time in the crystallizer. An increase in the feed inlet temperature also resulted in a smaller mean crystal size owing to an increase in the thermal load in the crystallizer and a corresponding decrease in the driving force for crystal growth. The permeate-side flow rate and inlet temperature have some influence on the CSD but a lesser influence on the mean crystal size.

This study indicates that the design of a CMDC that employs a concentrated feed stream is markedly different from that for MD that employs a relatively dilute feed stream. The latter is run using a large temperature difference between the feed and permeate sides of the membrane. As such, in a CMDC increasing the permeate-side inlet temperature can increase the water and solid NaCl product fluxes, whereas in conventional MD it would decrease the temperature driving force and thereby decrease the water permeation flux.

The conclusions drawn from this study need to be viewed in perspective of the range of values explored in the nine experiments. The values of the four factors that gave the largest water and NaCl solid production fluxes do not represent the global optimum. Rather they represent optimum values based on the range of values explored for the four factors in the OFF experiment design.

CHAPTER 7

CONCLUSIONS AND RECOMMENDATIONS

7.1 Overall conclusions

This thesis aims to develop novel methods for enhancing the hollow fibre membrane module performance and controlling scaling formation on the membrane surface in both high concentration MD and MDC processes. Therefore, attempts have been made to introduce dynamic shear-induced technique, explore measurement method of scaling information and optimize operating conditions for MD/MDC.

Firstly, a gas-liquid two-phase flow has been introduced and systematically investigated in DCMD process experimentally. With the encouraging results, an in-depth theoretical analysis on the working mechanisms of heat-transfer intensification was studied, associated with the investigation of temperature polarization coefficient and the ratio of conductive heat loss to the overall heat flux. More importantly, the specific expression of scaling resistance was derived as a theoretical basis for quantifying the efficiency of the bubbling system for membrane scaling control in high concentration DCMD. In order to fundamentally prevent crystal deposition on the membrane surface, the crystallization kinetics on the surface of PVDF hollow fiber membranes was studied using sodium chloride as a model scalant in batch-mode DCMD. Combined with experimental investigations, a mathematical model was developed and verified in terms of MD performance (critical point of major flux decline or scaling formation) and deposited crystal characteristics (median size and total number). Finally, a hybrid process that integrates MD with crystallization was systematically studied to obtain pure water and solid NaCl products simultaneously from a highly concentrated NaCl feed solution. An orthogonal fractional factorial

(OFF) experiment design was used to optimize the operating conditions and better realize zero discharge, including the flow rates and inlet temperatures on both the feed and permeate sides.

The major findings and conclusions are summarized as follows:

Chapter 3:

- In a bubbling-assisted DCMD module, the permeate flux enhancement ratio could reach up to 1.72 at an optimized gas flow rate. A higher flux enhancement ratio could be achieved at either a high feed operating temperature, low feed and permeate Reynolds numbers and a module with 45° inclined orientation, short fiber length or low packing density.
- Compared to a modified module with spacers, the introduction of gas bubbles is able to alleviate scaling formation on the membrane surface and delay the critical point of super saturation that leads to a major flux decline. These results were consistent with the membrane surface inspection by SEM, which showed that the least severe crystal deposition occurred in the original module incorporating bubbling.

Chapter 4:

- With the aid of direct observation and statistical analysis on the bubble characteristics in a specially-designed DCMD module, it was found that bubbles with small mean size and narrow size distribution were preferred for creating even flow distribution, intensifying mixing and enhancing surface shear rate. Compared to non-bubbling DCMD, the heat-transfer coefficient and temperature polarization coefficient (*TPC*) reached up to 2.30- and 2.13-fold, respectively, at an optimal gas flowrate.
- Based on the resistance-in-series model, the scaling resistance in a DCMD concentration experiment was quantified. Consistent with the experimental observation of crystal growth on the membrane surface, the increasing trend of the ratio of scaling resistance to the overall resistance (r_{fl} / r_{ov}) has confirmed the

dominant role of scaling formation on the membrane surface for the dramatic flux drop.

- The introduction of gas bubbles has shown benefits for supersaturation brine concentrating MD process - remarkably decreased the local-scaling resistance due to bubble-intensified shear stress and enhanced hydrodynamics. Also, total water removal for the brine concentration process was significantly improved by 131% and the discharged brine volume was reduced accordingly at appropriately selected gas flow rate.

Chapter 5:

- Based on the crystal size distribution (CSD) curves obtained from depositing crystals in a batch-mode DCMD for brine concentration, the crystallization kinetic constants were derived for salt deposition. Combined with the derived kinetic expressions and MD transport equations, a newly-established mathematical method, namely crystallization on membrane surface (COMS) modelling, was developed to quantify the crystal depositing situation with the operating time especially at the critical point.
- The proposed critical crystal size (26 μm) and the COMS model were verified by another set of experiments using the same kind membrane surface but with the different operating conditions. Hence, the critical point and the corresponding high efficient MD work area can be predicted before the experiments, which is meaningful to guide the high concentration MD operation.

Chapter 6:

- The continuous membrane distillation crystallization (CMDC) process has been shown to permit obtaining pure water and solid NaCl products simultaneously from a concentrated feed. The range analysis of the results from the orthogonal fractional factorial (OFF) experiment design identified the feed and permeate-side flow rates as the most influential factors affecting the final production.
- A confirmation experiment was conducted using the optimal values determined from the range analysis of OFF experiment design. Its result confirmed the merits

of the OFF experiment design and analysis in determining optimal operating conditions for the CMDC process.

- An ancillary study of the effect of the four factors on the mean crystal size and CSD indicated that the feed flow rate and inlet temperature were the dominant factors. The permeate-side flow rate and inlet temperature have some influence on the CSD but a lesser influence on the mean crystal size.
- The design of a CMDC that employs a concentrated feed stream is markedly different from that for MD that employs a relatively dilute feed stream. For instance, in a CMDC increasing the permeate-side inlet temperature can increase the water and solid NaCl product fluxes, whereas in conventional MD it would decrease the temperature driving force and thereby decrease the water permeation flux.

7.2 Recommendations for future research

For the study of gas-liquid two-phase in MD, modelling could be developed to explore the hydraulic situation and heat/mass transfer process. Yu and Yang et al. in our group have provided a good foundation for applying computational fluid dynamics (CFD) in the MD module (Yang, Yu et al. 2012; Yang, Yu et al. 2012; Yu, Yang et al. 2012). The encouraging computational and experimental results from our previous work (Chen, Yang et al. 2013; Chen, Lu et al. 2014) offer a distinct possibility to develop a 3-D CFD transfer modelling for a bubbling-assisted MD. It can be anticipated that the detailed simulated results would offer more guidance and inspirations on this two-phase flow design.

Potential crystallization in the membrane module and relative low performance are unavoidable challenges for the development of the MDC process. Therefore, combining membrane distillation with crystallization operations and adopting a cleaning technique to remove the depositing crystals from the membrane surface is one part of our future work. This method could extract more production water from the MD stage and make it easier to bring the crystallizer to super-saturation. These removed crystals from the membrane surface could be also used as seeds to speed up

the crystallization process. It would be expected that this novel design could avoid the unnecessary installation, energy loss and extract more production water and solid from the saturated brine.

For the cleaning technique in integrated MDC, ultrasound may be a good option for its uniform energy distribution and high fouling removal efficiency. It has been reported that an ultrasonic irradiation technique enhanced the performance of an AGMD system and the improvement is up to 200% (Zhu, Liu et al. 1999; Zhu and Liu 2000). Attempts could be done to test the enhancement of DCMD permeation flux under the varied ultrasonic conditions owing to reduction of the temperature and concentration polarization and improvement of hydraulic conditions by ultrasonic cavitations, acoustic streaming, and ultrasonic-induced vibration of membrane. Also, experiments could be conducted to test the possibility and efficiency of fouling/scaling removal.

Lastly, in Chapter 6, the lab-scale demonstration of continuous MDC has proven the feasibility of this process and the operating conditions have been optimized accordingly. However, a study of continuous MDC process based on pilot plant scale has yet to be conducted for a reliable estimation. Also, the combination of the MDC process with other membrane process such as RO, NF and UF could be studied for various applications since MDC is still a relatively new technology waiting to be fully exploited. And the optimal arrangements will be established for various scenarios.

REFRENCES

Altaee, A., Al-Rawajfeh, A.E. et al. (2010). "Application of vibratory system to improve the critical flux in submerged hollow fiber MF process." Separation Science and Technology , Vol. 45, pp. 28-34.

Armando, A.D., Culkin, B. et al. (1992). "New separation system extends the use of membranes." Proceedings of the Euromembrane 6, Lavoisier, paris(459-462).

Aamir, E., Nagy, Z.K. et al. (2010). "Evaluation of the Effect of Seed Preparation Method on the Product Crystal Size Distribution for Batch Cooling Crystallization Processes." Crystal Growth and Design, Vol. 10, No.11, pp. 4728-4740.

Abbas, A. and Romagnoli, J.A. (2007). "Multiscale modeling, simulation and validation of batch cooling crystallization." Separation and Purification Technology, No. 2, pp. 153-163.

Adham, S., Hussain, A. et al. (2013). "Application of Membrane Distillation for desalting brines from thermal desalination plants." Desalination, Vol. 314, pp. 101-108.

Alklaibi, A.M. and Lior, N. (2005). "Membrane-distillation desalination: Status and potential." Desalination, Vol. 171, , No. 2, pp. 111-131.

Alklaibi, A.M. and Lior, N. (2006). "Heat and mass transfer resistance analysis of membrane distillation." Journal of Membrane Science, Vol. 282, pp. 362-369.

Altmann, J. and Ripperger, S. (1997). "Particle deposition and layer formation at the crossflow microfiltration." Journal of Membrane Science, Vol. 124, No.1, pp. 119-128.

Banat, F., Jumah, R. et al. (2002). "Exploitation of solar energy collected by solar stills for desalination by membrane distillation." Renewable Energy, Vol. 25, No. 2, pp. 293-305.

Beier, S.P., Guerra, M. et al. (2006). "Dynamic microfiltration with a vibrating hollow fiber membrane module: Filtration of yeast suspensions." Journal of Membrane Science, Vol. 281, No. 1-2, pp. 281-287.

Beier, S.P. and Jonsson, G. (2007). "Separation of enzymes and yeast cells with a vibrating hollow fiber membrane module." Separation and Purification Technology, Vol. 53, No. 1, pp. 111-118.

Beier, S.P. and Jonsson, G. (2009). "A vibrating membrane bioreactor (VMBR): Macromolecular transmission—influence of extracellular polymeric substances." Chemical Engineering Science, Vol. 64, No. 7, pp. 1436-1444.

Bellara, S.R., Cui, Z.F. et al. (1996). "Gas sparging to enhance permeate flux in ultrafiltration using hollow fibre membranes." Journal of Membrane Science, Vol. 121, pp. 175-184.

Bilad, M.R., Mezohegyi, G. et al. (2012). "Novel magnetically induced membrane vibration (MMV) for fouling control in membrane bioreactors." Water Research, Vol. 46, No. 1, pp. 63-72.

Bouguecha, S., and Dhahbi, M. (2003). "Fluidized bed crystallizer and air gap membrane distillation as a solution to geothermal water desalination." Desalination, Vol. 152, No. 1-3, pp. 237-244.

Butcher, J.C. (2008). Numerical Methods for Ordinary Differential Equations, Wiley.

Cabassud, C., Laborie, S. et al. (1997). "How slug flow can improve ultrafiltration flux in organic hollow fibres." Journal of Membrane Science, Vol. 128, No. 1, pp. 93-101.

Calabro, V. and Drioli, E. (1996). "Polarization phenomenon in integrated reverse osmosis and membrane distillation for seawater desalination and waste water treatment." Desalination, Vol. 108, pp. 81-82.

Cath, T.Y., Adams, V.D. et al. (2004). "Experimental study of desalination using direct contact membrane distillation: a new approach to flux enhancement." Journal of Membrane Science, Vol. 228, No.1, pp. 5-16.

Catherine, C. (2009). "A review of membrane processes and renewable energies for desalination." Desalination, Vol. 245, No. 1-3, pp. 214-231.

Chan, M.T. (2005). "Membrane distillation crystallization." The University of New South Wales, Sydney, Australia.

Chan, M.T., Fane, A.G. et al. (2005). "Membrane distillation crystallization of concentrated salts—flux and crystal formation." Journal of Membrane Science, Vol. 257, No. 1-2, pp. 144-155.

Charcosset, C., Kieffer, R. et al. (2010). "Coupling between Membrane Processes and Crystallization Operations." Industrial & Engineering Chemistry Research, Vol. 49, pp. 5489-5495.

Charcosset, C., Samuel, B. et al. (2007). "Membrane techniques for the preparation of nanomaterials: nanotubes, nanowires and nanoparticles-a review." Dynamic Biochemistry, Process Biotechnology and Molecular Biology, Vol. 1, No. 1, pp. 15-23.

Charcosset, C. and Fessi, H. (2005). "Preparation of nanoparticles with a membrane contactor." Journal of Membrane Science, Vol. 266, No. 1-2, pp. 115-120.

Charpentier, J.C. (2002). "The triplet "molecular processes-product process" engineering: the future of chemical engineering." Chemical Engineering Science, Vol. 57, No. 22-23, pp. 4667-4690.

Chen, D., Weavers, L.K. et al. (2006). "Ultrasonic control of ceramic membrane fouling by particles: Effect of ultrasonic factors." Ultrasonics Sonochemistry, Vol. 13, pp. 379-387.

Chen, G., Lu, Y. et al. (2014). "Optimization of operating conditions for a continuous membrane distillation crystallization process with zero salty water discharge." Journal of Membrane Science, Vol. 450, pp. 1-11.

Chen, G., Yang, X. et al. (2014). "Heat transfer intensification and scaling mitigation in bubbling-enhanced membrane distillation for brine concentration." Journal of Membrane Science, Vol. 470, pp. 60-69.

Chen, G., Lu, Y. et al. (2014). "Quantitative Study on Crystallization Induced Scaling in High Concentration Direct Contact Membrane Distillation (DCMD)." Industrial & Engineering Chemistry Redearch, Vol. 53, No. 40, pp, 15656–15666.

Chen, G., Yang, X. et al. (2013). "Performance enhancement and scaling control with gas bubbling in direct contact membrane distillation." Desalination, Vol. 308, pp. 47-55.

Chen, J.C., Li, Q. et al. (2004). "In situ monitoring techniques for concentration polarization and fouling phenomena in membrane filtration." Advances in Colloid and Interface Science, Vol. 107, No. 2-3, pp. 83-108.

Cheng, L.H., Wu, P.C. et al. (2008). "Modeling and optimization of hollow fiber DCMD module for desalination." Journal of Membrane Science, Vol. 318, pp. 154-166.

Chilcott, T., Chan, M. et al. (2002). "Electrical impedance spectroscopy characterisation of conducting membranes I. Theory " Journal of Membrane Science, Vol. 195, No. 2, pp. 153-167.

Cobry, K.D., Yuan, Z. et al. (2011). "Comprehensive experimental studies of early-stage membrane scaling during nanofiltration." Desalination, Vol. 283, pp. 40-51.

Costa, C.B.B., da Costa, A.C. et al. (2005). "Mathematical modeling and optimal control strategy development for an adipic acid crystallization process." Chemical Engineeing Process: Process Intensification, Vol. 44, No. 7, pp. 737-753.

Cui, Z.F., Chang, S. et al. (2003). "The use of gas bubbling to enhance membrane processes." Journal of Membrane Science, Vol. 221, No. 1-2, pp. 1-35.

Cui, Z.F. and Wright, K.I.T. (1994). "Gas-liquid 2-phase cross-flow ultrafiltration of bsa and dextran solutions." Journal of Membrane Science, Vol. 90, No. 1-2, pp. 183-189.

Curcio, E., Criscuoli, A. et al. (2001). "Membrane crystallizers." Industrial & Engineering Chemistry Research, Vol. 40, pp. 2679-2684.

Curcio, E., Ji, X. et al. (2010). "Membrane distillation operated at high seawater concentration factors: Role of the membrane on $CaCO_3$ scaling in presence of humic acid." Journal of Membrane Science, Vol. 346, No. 2, pp. 263-269.

Dash, S.R. and Rohani, S. (1993). "Iterative Parameter-Estimation for Extraction of Crystallization Kinetics of Potassium-Chloride from Batch Experiments." Canadian Journal of Chemical Engineering, Vol. 71, No. 4, pp. 539-548.

Davey, R. and Garside, J. (2000). "From molecules to crystallizers: An introduction to crystallization." Oxford University Press.

Delgado, S., Villarroel, R. et al. (2008). "Effect of the shear intensity on fouling in submerged membrane bioreactor for wastewater treatment." Journal of Membrane Science, Vol. 311, No. 1-2, pp. 173-181.

Ding, Z., Liu, L. et al. (2011). "The use of intermittent gas bubbling to control membrane fouling in concentrating TCM extract by membrane distillation." Journal of Membrane Science, Vol. 372, No. 1-2, pp. 172-181.

Dumée, L., Campbell, J.L. et al. (2011). "The impact of hydrophobic coating on the performance of carbon nanotube bucky-paper membranes in membrane distillation." Desalination, Vol. 283, pp. 64-67.

Curcio, E., Di Profio, G. et al. (2003). "A new membrane-based crystallization technique: test on lysozyme." Journal of Crystal Growth, Vol. 247, No. 1-2, pp. 166-176.

Curcio, E., Di Profio, G. et al. (2002). "Membrane crystallization of macromolecular solutions." Desalination, Vol. 145, No. 1-3, pp. 173-177.

Edwie, F. and Chung, T.-S. (2012). "Development of hollow fiber membranes for water and salt recovery from highly concentrated brine via direct contact membrane distillationm and crystallization." Journal of Membrane Science, Vol. 421-422, pp. 111-123.

Edwie, F. and Chung, T.-S. (2013). "Development of simultaneous membrane distillation–crystallization (SMDC) technology for treatment of saturated brine." Chemical Engineering Science, Vol. 98, pp. 160-172.

Fritzmann, C., Löwenberg, J. et al. (2007). "State-of-the-art of reverse osmosis desalination." Desalination, Vol. 216, No. 1-3, pp. 1-76.

Gaedt, L., Chilcott, T. et al. (2002). "Electrical impedance spectroscopy characterisation of conducting membranes II. Experimental " Journal of Membrane Science, Vol. 195, No. 2, pp. 169-180.

Genkin, G., Waite, T.D. et al. (2006). "The effect of vibration and coagulant addition on the filtration performance of submerged hollow fibre membranes." Journal of Membrane Science, Vol. 281, No. 1-2, pp. 726-734.

Godino, M.P., Peña, L. et al. (1997). "Water production from brines by membrane distillation." Desalination, Vol. 108(1-3), pp. 91-97.

Goh, S., Zhang, J. et al. (2013). "Fouling and wetting in membrane distillation (MD) and MD-bioreactor (MDBR) for wastewater reclamation." Desalination, Vol. 323, pp. 39-47.

Greenlee, L.F., Lawler, D.F. et al. (2009). "Reverse osmosis desalination: Water sources, technology, and today's challenges." Water Research, Vol. 43, No. 9, pp. 2317-2348.

Gryta, M. (2002). "Concentration of NaCl solution by membrane distillation integrated with crystallization." Separation and Purification Technology, Vol. 37, pp. 3535-3558.

Gryta, M. (2005). "Long-term performance of membrane distillation process." Journal of Membrane Sciencev, Vol. 265, pp. 153-159.

Gryta, M. (2008). "Fouling in direct contact membrane distillation process." Journal of Membrane Science, Vol. 325, No. 1, pp. 383-394.

Guan, G., Wang, R. et al. (2012). "Analysis of membrane distillation crystallization system for high salinity brine treatment with zero discharge using aspen flowsheet simulation." Industrial & Engineering Chemistry Research, Vol. 51, pp. 13405-13413.

Hamachi, M. and Mietton-Peuchot, M. (1999). "Experimental investigations of cake characteristics in crossflow microfiltration " Chemical Engineering Science, Vol. 54, No. 18, pp. 4023-4030.

Hamachi, M. and Mietton-Peuchot, M. (2001). "Cake thickness measurement with an optical laser sensor." Chemical Engineering Research & Design, Vol. 79, No. A2, pp. 151-155

He, F., Gilron, J. et al. (2008). "Potential for scaling by sparingly soluble salts in crossflow DCMD." Journal of Membrane Science, Vol. 311, No. 1-2, pp. 68-80.

Harscoat, C., Jaffrin, M.Y. et al. (1999). "Influence of fermentation conditions and microfiltration process on membrane fouling during recovery of glucuronane polysaccharides from fermentation broths." Biotechnology and Bioengineering, Vol. 65, pp. 500-511.

He, F., Sirkar, K.K. et al. (2009). "Studies on scaling of membranes in desalination by direct contact membrane distillation: $CaCO_3$ and mixed $CaCO_3$/$CaSO_4$ systems." Chemical Engineering Sciense, Vol. 64, No. 8, pp. 1844-1859.

Hernyshov, M.N., Meindersma, G.W., et al. (2003). "Modelling temperature and salt concentration distribution in membrane distillation feed channel." Desalination, Vol. 157, No. 1-3, pp. 315-324.

Hogan, P.A., Sudjito, et al. (1991). "Desalination by solar heated membrane distillation." Desalination, Vol. 81 , No. 1-3, pp. 81-90.

Hsu, S.T., Cheng, K.T. et al. (2002). "Seawater desalination by direct contact membrane distillation." Desalination, Vol. 143, pp. 279-287.

Huczko, A. (2000). "Template-based synthesis of nanomaterials." Applied Physics A: Materials Science & Processing, Vol. 70, No. 4, pp. 365-376.

Hughes, D., Tirlapur, U.K. et al. (2006). "In situ 3D characterization of membrane fouling by yeast suspensions using two-photon femtosecond near infrared non-linear optical imaging." Journal of Membrane Science, Vol. 280, No. 1-2, pp. 124-133.

Hulburt, H.M. and Katz, S. (1964). "Some problems in particle technology: A statistical mechanical formulation." Chemical Engineering Science, Vol. 19, No. 8, pp. 555-574.

Hulteen, J.C. and Martin, C.R. (1997). "A general template-based method for the preparation of nanomaterials." Journal of Materials Chemistry, Vol. 7, No. 7, pp. 1075-1087.

Intelligence, G.W. (2013). "http://www.desalination.com".

Ji, X., Curcio, E. et al. (2010). "Membrane distillation-crystallization of seawater reverse osmosis brines." Separation and Purification Technology, Vol. 71, No. 1, pp. 76-82.

Karelin, F.N., Askerniya, A.A. et al. (1996). "Salt concentration and recovery from aqueous solutions using pressure-driven membrane processes." Desalination, Vol. 104, No. 1-2, pp. 69-74.

Kenning, D.B.R. and Kao, Y.S. (1972). "Convective heat transfer to water containing bubbles: enhancement not dependent on thermocapillary." International Journal of Heat Mass Transfer, Vol. 15, No. 9, pp.1709-&.

Khayet, M. (2011). "Membranes and theoretical modeling of membrane distillation: A review." Advances in Colloid and Interface Science, Vol. 164, No. 1-2, pp. 56-88.

Kieffer, R., Mangin, D. et al. (2009). "Precipitation of barium sulphate in a hollow fiber membrane contactor, Part I: Investigation of particulate fouling." Chemical Engineering Science, Vol. 64, No. 8, pp. 1759-1767.

Kim, J.C., Garzotto, F., et al. (2011). " Enhancement of solute removal in a hollow-fiber hemodialyzer by mechanical vibration." Blood Purification, Vol. 31, No. 4, pp. 227-234.

Knyazkova, T.V. and Kavitskaya, A.A. (2000). "Improved performance of reverse osmosis with dynamic layers onto membranes in separation of concentrated salt solutions." Desalination, Vol. 131, No. 1-3, pp. 129-136.

Kobayashi, T., Chai, X. et al. (1999). "Ultrasound enhanced cross-flow membrane filtration." Separation and Purification Technology, Vol. 17, pp. 31-40.

Kobayashi, T., Kobayashi, T. et al. (2003). "Ultrasound-enhanced membrane-cleaning processes applied water treatments: influence of sonic frequency on filtration treatments." Ultrasonics Sonochemistry, Vol. 41, No. 3, pp. 185-190.

Kola, A., Ye, Y. et al. (2012). "Application of low frequency transverse vibration on fouling limitation in submerged hollow fibre membranes." Journal of Membrane Science, Vol. 409-410, pp. 54-65.

Kola, A., Ye, Y. et al. (2014). "Transverse vibration as novel membrane fouling mitigation strategy in anaerobic membrane bioreactor applications." Journal of Membrane Science, Vol. 455, pp. 320-329.

Kubota, N., Otosaka, H. et al. (2000). "Effect of lead(II) impurity on the growth of sodium chloride crystals." Journal of Crystal Growth, Vol. 220, No. 1-2, pp. 135-139.

Kubota, S., Ohta, K. et al. (1988). "Experiments on seawater desalination by membrane distillation." Desalination, Vol. 69, No. 1, pp. 19-26.

Kubie, J. (1975). "Bubble induced heat transfer in two phase gas-liquid flow." International Journal of Heat and Mass Transfer, Vol. 18, No. 4, pp. 537-551.

Kuhn, J., Lakerveld, R. et al. (2009). "Characterization and dynamic optimization of membrane-assisted crystallization of adipic acid." Industrial & engineering chemistry research, Vol. 48, No. 1, pp. 5360-5369.

Kumar, S., Kusakable, K. et al. (1992). "Mechanism of heat transfer in bubbly liquid and liquid–solid systems: single bubble injection." AIChE Journal, Vol. 38, pp. 733-741.

Kyllönen, H., Pirkonen, P. et al. (2006). "Experimental aspects of ultrasonically enhanced cross-flow membrane filtration of industrial wastewater." Ultrasonics Sonochemistry, Vol. 13, No. 4, pp. 295-302.

Kyllönen, H.M., Pirkonen, P. et al. (2005). "Membrane filtration enhanced by ultrasound: a review." Desalination, Vol. 181, No. 1-3, pp. 319-335.

Lamminen, M.O., Walker, H.W. et al. (2004). "Mechanisms and factors influencing the ultrasonic cleaning of particle-fouled ceramic membranes." Journal of Membrane Science, Vol. 237, No. 1-2, pp. 213-223.

Lamminen, M.O., Walker, H.W. et al. (2006). "Cleaning of particle-fouled membranes during cross-flow filtration using an embedded ultrasonic transducer system." Journal of Membrane Science, Vol. 283, pp. 225-232.

Lawson, K.W. and Lloya, D.R. (1997). "Membrane distillation." Journal of Membrane Science, Vol. 124, No. 1, pp. 1-25.

Lawson, K.W. and Lloya, D.R. (1996). "Membrane distillation. I. Module design and performance evaluation using vacuum membrane distillation." Journal of Membrane Science, Vol. 120, No. 1, pp. 111-121.

Lee, C.Y.M., Todd, P.S.R. et al. (1998). "Control of nucleation in oligonucleotide crystallization by the osmotic dewatering method with kinetic water removal rate control." Jounal Crystal Growth, Vol. 187, No. 3-4, pp. 490-498.

Lee, C.Y., Sportiello, M.G. et al. (1997). "Characterization and applicationsof osmotic dewatering to the crystallization of oligonucleotides." Biotechnology Progress, Vol. 13, No. 1, pp. 77-81.

Leighton, T.G. (1994). "The Acoustic Bubble, Academic Press." Inc, San Diego.

Leland, M., Vane, F.R.A., et al. (1999). "Reduction of concentration polarization in pervaporation using vibrating membrane module." Journal of Membrane Science, Vol. 153, pp. 233-241.

Li, H., Fane, A.G. et al. (2003). "Observation of deposition and removal behaviour of submicron bacteria on the membrane surface during crossflow microfiltration." Journal of Membrane Science, Vol. 217, No. 1-2, pp. 29-41.

Li, J.M., Xu, Z.K. et al. (2003). "Microporous polypropylene and polyethylene hollow fiber membranes. Part 3. Experimental studies on membrane distillation for desalination." Desalination, Vol. 155, No. 2, pp. 153-156.

Li, T., Law, A.W.K. et al. (2014). "Submerged hollow fibre membrane filtration with transverse and longitudinal vibrations." Journal of Membrane Science, Vol. 455, pp. 83-91.

Li, X., Yu, J. et al. (2011). "Fouling mitigation for hollow-fiber UF membrane by sonication." Desalination, Vol. 281, pp. 23-29.

Liao, Y., Wang, R. et al. (2013). "Fabrication of polyvinylidene fluoride (PVDF) nanofiber membranes by electro-spinning for direct contact membrane distillation." Journal of Membrane Science, Vol. 425-426, pp. 30-39.

Liao, Y., Wang, R. et al. (2013). "Engineering superhydrophobic surface on poly(vinylidene fluoride) nanofiber membranes for direct contact membrane distillation." Journal of Membrane Science, Vol. 440, pp. 77-87.

Lu, X., Kujundzic, E. et al. (2012). "Ultrasonic sensor control of flow reversal in RO desalination—Part 1: Mitigation of calcium sulfate scaling." Journal of Membrane Science, Vol. 419-420, pp. 20-32.

Lu, Y., Ding, Z. et al. (2008). "The influence of bubble characteristics on the performance of submerged hollow fiber membrane module used in microfiltration." Separation and Purification Technology, Vol. 61, No. 1, pp. 89-95.

Macedonio, F., Curcio, E. et al. (2007). "Integrated membrane systems for seawater desalination: energetic and exergetic analysis, economic evaluation, experimental study." Desalination, Vol. 203, No. 1-3, pp. 260-276.

Martínez-Díez, L. and Vazquez-Gonzalez, M.I. (1999). "Temperature and concentration polarization in membrane distillation of aqueous salt solutions." Journal of Membrane Science, Vol. 156, No. 2, pp. 265-273.

Mairal, A.P., Greenberg, A.R. et al. (2000). "Investigation of membrane fouling and cleaning using ultrasonic time-domain reflectometry." Desalination, Vol. 130, No. 1, pp. 45-60.

Mairal, A.P., Greenberg, A.R. et al. (1999). "Real-time measurement of inorganic fouling of RO desalination membranes using ultrasonic time-domain reflectometry." Journal of Membrane Science, Vol. 159, No. 1-2, pp. 185-196.

Mariah, L., Buckley, C.A. et al. (2006). "Membrane distillation of concentrated brines—Role of water activities in the evaluation of driving force." Journal of Membrane Science, Vol. 280, No. 1-2, pp. 937-947.

Martínez-Díez, L. and Florido-Díaz, F.J. (2001). "Desalination of brines by membrane distillation." Desalination, Vol. 137, No. 1-3, pp. 267-273.

Martínez-Díez, L., Florido-Díaz, F.J. et al. (2000). "Study of polarization phenomena in membrane distillation of aqueous salt solutions." Separation Science and Technology, Vol. 35, No. 10, pp. 1485-1501 .

Martínez-Díez, L. and Vaízquez-Gonzaílez, M.I. (1999). "Temperature and concentration polarization in membrane distillation of aqueous salt solutions." Journal of Membrane Science, Vol. 156, pp. 265-273.

Martínez, L. and Rodríguez-Maroto, J.M. (2007). "On transport resistances in direct contact membrane distillation." Journal of Membrane Science, Vol. 295, pp. 28–39.

Martin, C.R. (1996). "Membrane based synthesis of nanomaterials." Chemistry of Materials, Vol. 8, No. 8, pp. 1739-1746.

Mathworks, D.C. (2014). from "http://www.mathworks.com/help/curvefit/smoothing-splines.html." Retrieved Jan 13.

Mercier-Bonin, M., Lagane, C. et al. (2000). "Influence of a gas/liquid two-phase flow on the ultrafiltration and microfiltration performances: case of a ceramic flat sheet membrane." Journal of Membrane Science, Vol. 180, No. 1, pp. 93-102.

Mercier, M., Fonade, C. et al. (1997). "How slug flow can enhance the ultrafiltration flux in mineral tubular membranes." Journal of Membrane Science, Vol. 128, No. 1, pp. 103-113.

Mersmann, A. (2001). "Crystallization Technology Handbook, 2nd ed.": Dekker: New York.

Mengual, J.I. and Peňa, L. (1997). "Membrane distillation." Colloid and Surface Science, pp. 17-29.

Mizrahi, G., Wong, K. et al. (2012). "Ultrasonic sensor control of flow reversal in RO desalination. Part 2: Mitigation of calcium carbonate scaling." Journal of Membrane Science, Vol. 419-420, pp. 9-19.

Mores, W. and Davis, R. (2001). "Direct visual observation of yeast deposition and removal during microfiltration " Journal of Membrane Science, Vol. 189, No. 2, pp. 217-230

Mulin, J.W. (1972). "Crystallization, 2nd ed.": Butterworth & Co.

Muthukumaran, S., Kentish, S. et al. (2005). "The optimisation of ultrasonic cleaning procedures for dairy fouled ultrafiltration membranes." Ultrasonics Sonochemistry, Vol. 12, No. 1-2, pp. 29-35.

Myerson, A.S. (2002). "Handbook of Industrial Crystallization, 2nd ed.": Butterworth-Heinemann: Boston, MA.

Nývlt, J. (1968). "Kinetics of nucleation in solutions." Journal of Crystal Growth, Vol. 3-4, pp. 377-383.

Nývlt, J., Söhnel, O. et al. (1985). "The kinetics of industrial crystallization." Elsevier, Amsterdam Academia, Prague.

OriginLab from: http://www.originlab.de/www/helponline/origin/en/UserGuide/GaussAmp.html.

Pazuki, G.R. and Rohani, A.A. (2006). "A new model for the activity coefficients of individual ions in aqueous electrolyte solutions." Fluid Phase Equilibria, Vol. 242, No. 1, pp. 65-71.

Perry, R.H., Green, D.W., et al. (1997). "Perry's chemical engineers' handbook." New York: McGraw-Hill Companies, Inc.

Phattaranawik, J., Fane, A.G. et al. (2008). "A novel membrane bioreactor based on membrane distillation." Desalination, Vol. 223, No. 1-3, pp. 386-395.

Psoch, C. and Schiewer, S. (2006). "Dimensionless numbers for the analysis of air sparging aimed to reduce fouling in tubular membranes of a membrane bioreactor." Desalination, Vol. 197, No. 1-3, pp. 9-22.

Qiu, Y. and Rasmuson, A.C. (1991). "Nucleationand growth of of succinic acid in a batch cooling crystallizer." AIChE Journal, Vol. 37, pp. 1293.

Randolph, A.D. and Larson, M.A. (1971). "Theory of Particulate Processes." Academic Press, New York.

Randolph, A.D. and Maurice, A.L. (1988). "Theory of particulate processes: analysis and techniques of continuous crystallization " San Diego, Academic Press.

Ratkovich, N., Chan, C.C.V. et al. (2009). "Experimental study and CFD modelling of a two-phase slug flow for an airlift tubular membrane." Chemical Engineering Science, Vol. 64, No. 16, pp. 3576-3584.

Ravanchi, M.T., Kaghazchi, T. et al. (2009). "A novel separation process for olefin gas purification: effect of operating parameters on separation performance and process optimization." Journal of the Taiwan Institute of Chemical Engineering, Vol. 40, pp. 511-517.

Söhnel, O., Bravi, M. et al. (1996). "Growth kinetics of sodium perborate from batch crystallization." Journal of Crystal Growth, Vol. 160, No. 3–4, pp. 355-360.

Safavi, M. and Mohammadi, T. (2009). "High-salinity water desalination using VMD." Chemical Engineering Journal, Vol. 149, No. 1-3, pp. 191-195.

Sarti, G.C., Gostoli, C. et al. (1985). "Low energy cost desalination processes using hydrophobic membranes." Desalination, Vol. 56, pp. 277-286.

Schmid, G. (2002). "Materials in nanoporous alumina." Journal Materials Chemistry, Vol. 12, No. 5, pp. 1231-1238.

Schofield, R.W., Fane, A.G. et al. (1987). "Heat and mass transfer in membrane distillation." Journal of Membrane Science, Vol. 33, pp. 299-313.

Schofield, R.W., Fane, A.G. et al. (1990). "Factors affecting flux in membrane distillation." Desalination, Vol. 77, pp. 279-294.

Sherwood, T.K., Pigford, R.L. et al. (1975). "Mass Transfer." McGraw-Hill,New York.

Sherwood, T.K., Brain, P.L.T. et al. (1965). "Salt concentration at phase boundaries in desalination by reverse osmosis." Industrial and Engineering Chemistry Fundamentals, No. 4, pp. 113-118

Short, B.E. (1965). "Flow geometry and heat exchanger performance." Chemical Engineering Progress, Vol. 61, No. 7, pp. 63-&.

Sim, S.T.V., Chong, T.H., et al. (2012). "Monitoring of colloidal fouling and its associated metastability using Ultrasonic Time Domain Reflectometry." Journal of Membrane Science, Vol. 401-402, pp. 241-253.

Singh, D. and Sirkar K.K. (2012). "Desalination of brine and produced water by direct contact membrane distillation at high temperatures and pressures." Journal of Membrane Science, Vol. 389, pp. 380-388.

Sofia, A., Ng, W.J. et al. (2004). "Engineering design approaches for minimum fouling in submerged MBR." Desalination, Vol. 160, No. 1, pp. 67-74.

Stankiewicz, A. (2003). "Reactive separations for process intensification: an industrial perspective." Chemical Engineering Process, Vol. 42, No. 3, pp. 137-144.

Susanto, H. (2011). "Towards practical implementations of membrane distillation." Chemical Engineering Process, Vol.50, pp. 139-150.

Subramani, A., Hoek, E.M.V. (2008). " Direct observation of initial microbial deposition onto reverse osmosisand nanofiltrati on membranes." Journal of Membrane Science, Vol. 319, No. 1-2, pp. 111-125.

Subramani, A., Huang, X.F., Hoek, E.M.V. (2011). " Direct observation of bacterial deposition onto clean and organic-fouled polyamide membranes." Journal of Colloid and Interface Science, Vol. 336, No. 1, pp. 13-20.

Tajima, F., Yamamoto, T. (1988). "Apparatus for filtering water containing radioactive substances in nuclear power plants." Toshiba, U.S. Patent 4.

Tavare, N.S. (1991). "Batch Crystallizers." Reviews in Chemical Engineering, Vol. 7, No. 3-4, pp. 211-355.

Tavare, N.S. (1993). "Characterization of crystallization kinetics from batch experiments." Separation and Purification Methods, Vol. 22, No. 2, pp. 93-210.

Tavare, N.S. and Garside, J. (1986). "Simultaneous Estimation of Crystal Nucleation and Growth-Kinetics from Batch Experiments." Chemical Engineering Research and Design, Vol. 64, No. 2, pp. 109-118.

Teoh, M.M., Bonyadi, S. et al. (2008). "Investigation of different hollow fiber module designs for flux enhancement in the membrane distillation process." Journal of Membrane Science, Vol. 311, No. 1-2, pp. 371-379.

Tomaszewska, M., Gryta, M. et al. (1995). "Study on the concentration of acids by membrane distillation." Journal of Membrane Science, Vol. 102, pp. 112-122.

The International Desalination & Water Reuse Quarterly industry website (D&WR) (2013). from " http://www.desalination.biz/news ". Retrieved Oct 14.

U. Frenander, A.S.J. (1996). "Cell harvesting by cross-flow microfiltration using a shear-enhanced module." Biotechnology and Bioengineering, Vol. 52, pp. 397–403.

Uchymiak, M., Lyster, E. et al. (2008). "Kinetics of gypsum crystal growth on a reverse osmosis membrane." Journal of Membrane Science, Vol. 314, No. 1–2, pp. 163-172.

Uchymiak, M., Rahardianto, A. et al. (2007). "A novel RO ex situ scale observation detector (EXSOD) for mineral scale characterization and early detection." Journal of Membrane Science, Vol. 291, No. 1–2, pp. 86-95.

Vera, L., Delgado, S. et al. (2000). "Dimensionless numbers for the steady-state flux of cross-flow microfiltration and ultrafiltration with gas sparging." Chemical Engineering Science, Vol. 55, No. 17, pp. 3419-3428.

Wang, Z., Gu, Z. et al. (2009). "Application of vacuum membrane distillation to lithium bromide absorption refrigeration system." International Journal of Refrigeration, Vol. 32, No. 7, pp. 1587-1596.

Warner, S.B. and Science F. (1995). "Prantice Hall." New Jersey: 201-248, ISBN: 200-202-424541-424540.

Wicaksana, F., Fane, A.G. et al. (2006). "Fibre movement induced by bubbling using submerged hollow fibre membranes." Journal of Membrane Science, Vol. 271, No. 1–2, pp. 186-195.

Wirth, D. and Cabassud C. (2002). "Water desalination using membrane distillation: comparison between inside/out and outside/in permeation." Desalination, Vol. 147, No. 1–3, pp. 139-145.

Wu, Y. and Drioli, E. (1989). "The behaviour of membrane distillation of concentrated aqueous solution." Water Treatment, pp. 399-415.

Wu, Y., Kong, Y. et al. (1991). "An experimental study on membrane distillation-crystallization for treating waste water in taurine production." Desalination, Vol. 80, pp. 235-242.

Yang, X., Wang, R. et al. (2013). "Membrane module design and dynamic shear-induced techniques to enhance liquid separation by hollow fiber modules: a review." Desalination and Water Treatment, Vol. 51, No. 16-18, pp. 3604-3627.

Yang, X., Fridjonsson, E.O. et al. (2014). "A non-invasive study of flow dynamics in membrane distillation hollow fiber modules using low-field nuclear magnetic resonance imaging (MRI)." Journal of Membrane Science, Vol. 451, pp. 46-54.

Yang, X., Wang, R. et al. (2011). "Novel designs for improving the performance of hollow fiber membrane distillation modules." Journal of Membrane Science, Vol. 384, No. 1–2, pp. 52-62.

Yang, X., Wang, R. et al. (2011). "Performance improvement of PVDF hollow fiber-based membrane distillation process." Journal of Membrane Science, Vol. 369, pp. 437-447.

Yang, X., Yu, H. et al. (2012). "Analysis of the effect of turbulence promoters in hollow fiber membrane distillation modules by computational fluid dynamic (CFD) simulations." Journal of Membrane Science, Vol. 415–416, pp. 758-769.

Yang, X., Yu, H. et al. (2012). "Optimization of microstructured hollow fiber design for membrane distillation applications using CFD modeling." Journal of Membrane Science, Vol. 421-422, pp. 258-270.

Yeo, A.P.S., Law, A.W.K. et al. (2006). "Factors affecting the performance of a submerged hollow fiber bundle." Journal of Membrane Science, Vol. 280, No. 1–2, pp. 969-982.

Yeo, A.P.S., Law, A.W.K. et al. (2007). "The relationship between performance of submerged hollow fibers and bubble-induced phenomena examined by particle image velocimetry." Journal of Membrane Science, Vol. 304, No. 1–2, pp. 125-137.

Yu, H., Yang, X. et al. (2011). "Numerical simulation of heat and mass transfer in direct membrane distillation in a hollow fiber module with laminar flow." Journal of Membrane Science, Vol. 384, No. 1–2, pp. 107-116.

Yu, H., Yang, X. et al. (2012). "Analysis of heat and mass transfer by CFD for performance enhancement in direct contact membrane distillation." Journal of Membrane Science, Vol. 405–406, pp. 38-47.

Yun, Y., Ma, R. et al. (2006). "Direct contact membrane distillation mechanism for high concentration NaCl solutions." Desalination, Vol. 188, No. 1-3, pp. 251-262.

Zarkadas, D.M. and Sirkar K.K. (2006). "Antisolvent crystallization in porous hollow fiber devices." Chemical Engineering Science, Vol. 61, No. 15, pp. 5030-5048.

Zhang, J., Li, J.D. et al. (2010). "Performance of asymmetric hollow fibre membranes in membrane distillation under various configurations and vacuum enhancement." Journal of Membrane Science, Vol. 362, No. 1–2, pp. 517-528.

Zhang, K., Cui, Z. et al. (2009). "Effect of bubble size and frequency on mass transfer in flat sheet MBR." Journal of Membrane Science, Vol. 332, No. 1-2, pp. 30-37.

Zhu, C. and Liu G. (2000). "Modeling of ultrasonic enhancement on membrane distillation." Journal of Membrane Science, Vol. 176, pp. 31-41.

Zhu, C., Liu, G. L.et al. (1999). "Ultrasonic stimulation on enhancement of air gap membrane distillation." Journal of Membrane Science, Vol. 161, pp. 85-93.

Zuo, G., Wang, R. et al. (2011). "Energy efficiency evaluation and economic analyses of direct contact membrane distillation system using Aspen Plus." Desalination, Vol. 283, pp. 237-244.